How the Physics of Acceleration in Solar Flare Loops Determines Gamma-Ray and Neutron Production

R. J. Murphy

E.O. Hulburt Center for Space Research, Code 7650, Naval Research Lab., Washington, DC 20375, U.S.A.

murphy@ssd5.nrl.navy.mil

Benzion Kozlovsky

School of Physics and Astronomy, Tel Aviv University, Ramat Aviv, Israel

G. H. Share

Department of Astronomy, University of Maryland, College Park, MD 20742

X.-M. Hua

L3 Communications, Analytics Corporation, Largo, MD 20774

and

R. E. Lingenfelter

Center for Astrophysics and Space Sciences, 0424, University of California, San Diego, La Jolla, CA 92093

ABSTRACT

The measurable quantities associated with γ-ray and neutron observations of solar flares are: nuclear-deexcitation line shapes, shifts, fluences, and time histories; neutron capture and annihilation line fluences and time histories; and energy-dependent escaping neutron fluence and time history. Theoretical calculations of these measurable quantities require a model for ion acceleration, transport and interaction. Using recently updated cross sections for nuclear interactions, we have calculated a number of measurable quantities associated with narrow nuclear deexcitation γ-ray lines, the neutron capture line, and escaping neutron spectra. The yields and yield ratios presented can be used by researchers analyzing high energy solar flare data. All of the calculations were performed within the context of a magnetic loop transport and interaction model

that provides a physical basis for the interacting accelerated ion time delays and anisotropic angular distributions that previously have only been assumed. The model includes energy losses due to Coulomb collisions, removal by nuclear reactions, magnetic mirroring in the convergent flux tube, and MHD pitch-angle scattering in the corona. Each of the measurable quantities depends to varying degree on the parameters of the model. In this paper we explore these dependences in detail and construct a self-consistent approach to the analysis of high-energy flare data that provides an optimum set of parameters with meaningful uncertainties. The calculations are applied in a comprehensive analysis of the γ-ray and neutron observations of the 1991 June 4 solar flare obtained with *CGRO*/OSSE, providing an algorithm that can be applied to other flares with measurements covering a similarly wide range of measurable quantities. We find that the loop model can account for the observations with realistic values for the parameters. In addition, our analysis of the neutron data showed that the accelerated ion spectrum for this flare was not an unbroken power law, but had to steepen sharply above $\sim$125 MeV nucleon^{-1}.

Subject headings: Sun: flares — Sun: X-rays, gamma rays — acceleration of particles — nuclear reactions

1. INTRODUCTION

Information about ions accelerated in solar flares that escape from the Sun can be obtained from direct measurement of impulsive solar energetic particle events in interplanetary space (Reames 2002). Information about flare-accelerated ions that remain at the Sun can be obtained by observing the emissions that result from their nuclear interactions with the solar atmosphere. These interactions produce excited and radioactive nuclei, neutrons and π-mesons. All of these products subsequently produce observable γ-rays via secondary processes and the neutrons that escape may be observed both directly in space and via their decay protons.

The measurable quantities associated with these emissions (e.g., γ-ray line intensities, shapes, and time histories and escaping neutron spectra and time histories) convey information about the accelerated ions responsible for their production. *Acceleration parameters*, such as the number and spectral shape of the accelerated protons and α particles (and thus their energy content) and the relative abundances of the accelerated ions, can be obtained from measured deexcitation line intensities and ratios. This aspect of high-energy flare emission has been well-explored in past research (e.g., Ramaty et al. (1995)).

However, the measurable quantities can also depend strongly on the physical conditions of the magnetic flare loop in which the particles transport from the acceleration site to the interaction region. These physical conditions are described by *physical parameters*, such as loop length, the level of pitch-angle scattering (PAS) within the loop, the degree of convergence of the loop magnetic field at the footpoints, the location of the flare on the Sun, and the density and temperature height-profile and elemental composition of the flaring atmosphere. Analyses of high-energy solar-flare emissions therefore offer the potential to learn much more about the flare process than just particle acceleration, such as the structure and evolution of the flare environment.

But because each of the measurable quantities can depend on some or all of the same acceleration or physical parameters, deriving well-constrained values for those parameters is challenging. Previous analyses often have not taken these complicated inter-dependences into account in a systematic way, relying on *ad hoc* assumptions that resulted in unrealistically small uncertainties for their limited number of parameters. The goal of this paper is to systematically address these inter-dependences by identifying all relevant acceleration and physical parameters, showing how the nature of the nuclear interactions depend on them and how the various measurable quantities are subsequently affected. This understanding will enable us to construct a comprehensive and self-consistent approach to the analysis of flare data that will provide optimum parameter values and meaningful uncertainties which can simultaneously provide predicted observable quantities that are consistent with the measured quantities. Success of this approach will require that the available flare measurements cover a sufficiently-broad range of the measurable quantities.

In §2 we describe in detail how the acceleration and physical parameters affect the nuclear interactions responsible for the high-energy flare emissions and how the measurable quantities associated with these emissions are subsequently affected. We also explore the ranges of accelerated ion energies that are responsible for the various emissions. With this understanding, in §3 we use the measurements of the 1991 June 4 flare to constrain all of the relevant parameters, developing a data analysis algorithm that provides the approach and analysis steps necessary for such a comprehensive analysis. The 1991 June 4 flare observed by Oriented Scintillation Spectrometer Experiment (OSSE) on the *Compton Gamma Ray Observatory* (*CGRO*) and by a number of other instruments is one of the best-measured high-energy flares to date, providing time-dependent measurements with good statistical significance of hard X-rays, γ-ray lines and continuum, and neutrons.

2. GAMMA-RAY AND NEUTRON PRODUCTION BY ACCELERATED IONS IN SOLAR FLARES

Accelerated-ion interactions with the ambient solar medium produce excited nuclei which promptly deexcite, yielding observable γ-ray lines. The lines resulting from accelerated protons and α particles interacting with ambient nuclei heavier than He are "narrow" (fractional FWHM $\sim 2\%$), due to the relatively low recoil velocity of the heavy nucleus. Accelerated α particles and heavier ions interacting with ambient H and He produce "broad" lines (fractional FWHM $\sim 20\%$) due to the relatively high recoil velocity of the nucleus. Recently Kuzhevskij et al. (2005a) considered deexcitation line yields from heavy-heavy nucleus interactions, but we have found that for the narrow 1.634 MeV ^{20}Ne and 1.369 MeV ^{24}Mg lines produced by interactions of ^{12}C and ^{16}O, the yields are negligible due to both the lower abundances of both species and the higher energy loss of heavy particles. Accelerated ion interactions also create radioactive nuclei which produce delayed γ-ray lines that can be observed when the prompt emission is negligible (Tatischeff et al. 2006).

Ion interactions also produce neutrons which can be observed both directly and indirectly. Neutrons that escape from the Sun and survive the transit to Earth can be directly detected with instruments in orbit and, for events with sufficient high-energy neutrons (>300 MeV), by neutron monitors on the ground. Those escaping neutrons that decay can be indirectly detected via their decay protons in space (e.g., Evenson et al. (1983)). Neutrons that remain at the Sun may be indirectly detected because some of them can be captured on ambient hydrogen in the photosphere, producing deuterium and a strong γ-ray line at 2.223 MeV.

Our understanding of γ-ray and neutron production has evolved for more than 35 years. After the seminal work by Lingenfelter & Ramaty (1967), a comprehensive treatment of deexcitation-line production was given by Ramaty et al. (1979). The resulting γ-ray line production code has recently been updated (Kozlovsky et al. 2002) to incorporate new cross-section data. This code calculates a complete γ-ray line spectrum along any observing direction from the flare site for any assumed accelerated-ion spectral shape, accelerated and ambient composition, and interacting-particle angular distribution. We will use this deexcitation-line production code in this paper. A simplified version of the code is available at http://lheawww.gsfc.nasa.gov/users/ramaty/ViewPubs/ramaty.html.

Hua et al. (1989) developed a magnetic loop transport and interaction model (described more fully below) in which a Monte Carlo simulation follows an individual accelerated ion through a flare loop until it either undergoes a nuclear reaction or its energy falls below nuclear reaction thresholds. The process is repeated until adequate statistical significance is achieved. The most important aspects of ion transport are included in the model: energy

losses due to Coulomb collisions, removal by nuclear reactions, magnetic mirroring in the convergent flux tube, and MHD pitch angle scattering. They applied this model to deexcitation line reactions and calculated the depth distribution and time history (for instantaneous release of the energetic ions) for production of several nuclear deexcitation lines. We will use this deexcitation-line transport code in this paper.

The theory of neutron production, escape, and transport to Earth was first treated by Lingenfelter et al. (1965a,b) and was further developed by Hua & Lingenfelter (1987a) using Monte Carlo transport simulations to follow the neutrons until until they decay, are captured on H in the solar atmosphere to produce the 2.223 MeV neutron-capture line, or escape from the Sun. Using the magnetic loop model referred to above, Hua et al. (2002) calculated angle-dependent neutron spectra using updated neutron production cross sections and new kinematics. The code calculates escaping neutron spectra and neutron-capture line intensities and time histories along any observing direction from the flare site. We will use this neutron/neutron-capture line transport/production code in this paper. The code is available on-line (see Hua et al. (2002)).

Ion interactions also produce radioactive nuclei and, if there are sufficient very high energy accelerated ions, positively-charged pions, both of which decay to produce positrons which then annihilate to produce the strong 0.511 MeV annihilation line. Production of positron-emitting nuclei was discussed by Kozlovsky et al. (1987, 2004) and Tatischeff et al. (2006). Pion production was discussed by Murphy et al. (1987). Positron annihilation in the solar atmosphere was recently addressed by Murphy et al. (2005). Unfortunately, the intense flux of X rays from the June 4 flare restricted the usable data to those from the detector pointed away from the Sun (see §3.1). Because of the resulting strong attenuation of <1 MeV photons by the detector shields, measurements of the annihilation line during the peak of the flare are not available and positron production will not be discussed in this paper.

Neutral pions can also be produced which decay into two γ rays with energies of 67.6 MeV in the pion rest frame. The energies of these photons are then Doppler shifted by the pion motion. The spectrum is a broad peak centered near 70 MeV with a full width at half maximum of $\sim$100 MeV (Lingenfelter & Ramaty 1967; Crannell et al. 1979; Murphy et al. 1987). The positrons and electrons from charged pion decay produce continuum bremsstrahlung, most easily observed at >10 MeV. We will see that the accelerated particle spectrum responsible for γ-ray emission in the June 4 flare was relatively steep and did not produce significant numbers of pions. Pion production will also not be discussed in this paper.

In §2.1 we describe the loop transport and interaction model and its parameters relat-

ing to the physical conditions of the magnetic loop. In §2.2 we summarize the acceleration and physical parameters addressed by our calculations of deexcitation γ-ray, neutron, and neutron-capture line production. In §2.3 we discuss how these parameters affect the nuclear interactions. (Some of the material concerning the interaction time history and depth distribution was first discussed by Hua et al. (1989) but for a Bessel function accelerated-particle spectrum rather than the power law spectrum presented here. Some of the material concerning neutron production was discussed by Hua et al. (2002) but they did not include a discussion of the neutron capture line.) In §2.4 we describe how the measurable quantities associated with the products of these interactions (deexcitation lines, neutrons, and the neutron-capture line) are subsequently affected and the ranges of ion energies that are most effective in producing each. The understanding gained from the single-loop study can be easily extended to account for multiple-loop structures.

2.1. Magnetic Loop Transport and Interaction Model

The magnetic loop will form the basic geometrical structure for the calculations performed here. Imaging observations by Yohkoh and *RHESSI* indicate that X- and γ-ray flare emission occurs at footpoints, suggesting the presence of a loop. Observations at radio, optical and soft X-rays clearly reveal the loop structure. We will perform our calculations for a single loop since the fundamental processes probably occur within one loop. Complex flare processes may be considered as resulting from combinations of loops; e.g., recent imaging results from *RHESSI* show that the electron bremsstrahlung and neutron capture line emissions are physically separated suggesting at least two loops (Hurford et al. 2003).

We will use the loop formalism developed by Hua et al. (1989). Their transport and interaction model consists of a semicircular coronal portion of length L and two straight portions extending vertically from the transition region through the chromosphere into the photosphere. Recent γ-ray line shift measurements by *RHESSI* (Smith et al. 2003) suggest that in some flares the loop may be inclined to the solar surface. Here we will only perform calculations for vertical loops. Qualitative implications for inclined loops can be estimated from the results for a vertical loop.

Below the transition region, the magnetic field strength is assumed proportional to a power δ of the pressure (Zweibel & Haber 1983). For coronal and photospheric pressures of 0.2 and 10^5 dyne cm^{-2} and relevant magnetic field strengths of 100 and 1600 gauss, respectively, $\delta \simeq 0.2$. Such a converging magnetic field can result in mirroring of accelerated particles. Pitch angle scattering is characterized by Λ, the mean free path required for an arbitrary initial angular distribution to relax to an isotropic distribution. The dependence

of Λ on particle energy is expected to be weak (see discussion by Hua et al. (1989)) and is assumed here to be independent. The level of PAS is characterized by λ, the ratio of Λ to the loop half-length L_c ($= L/2$). Magnetic convergence and PAS directly affect the angular distribution of the accelerated particles when they interact with the ambient medium. As we will see, this angular distribution will have a strong affect on the subsequent observable emissions. In the past, researchers have often assumed specific angular distributions (such as isotropic, downward beam, fan beam, etc.). With the present calculations, the distributions will develop naturally from the physical parameters of the loop model and cover a wider range of distributions.

Because recent results based on measurements made with *RHESSI* (Share et al. 2004; Murphy et al. 2005; Aschwanden et al. 2003) and the Solar Maximum Mission, Yohkoh and GRANAT/PHEBUS (Kuzhevskij et al. 2005b) have suggested that the flaring atmosphere within the loop may be considerably different from that of the quiet Sun, several height-density profiles ($n(h)$) for the solar atmosphere will be considered.

In the Monte Carlo simulation, accelerated ions are released instantaneously and isotropically at the top of the loop. Each ion is followed until it interacts or thermalizes, typically near the loop footpoints in the chromosphere or upper photosphere where the density is sufficient for efficient nuclear interactions. When an interaction occurs, the time after the initial release of the energetic ion, the location along the loop, and the direction of motion of the ion are recorded. This is repeated until sufficient statistical significance is achieved. Because the ions do not escape (i.e., they either interact or thermalize), the calculations are "thick target". For deexcitation line reactions, the resulting interacting-particle angular distribution can then be used with the γ-ray line production code to calculate line shapes and shifts. The attenuation of the γ ray along the line of sight is calculated from the location of the interaction along the loop. For neutron-producing reactions, the Monte Carlo simulation follows the neutron until it escapes into space, is captured on H to contribute the 2.223 MeV capture line, reacts with ^{3}He without production of radiation (see §2.4.3), or decays. If a neutron-capture γ ray is produced, its attenuation along the line of site is calculated.

2.2. Summary of the Acceleration and Physical Parameters

Table 1 lists the acceleration and physical parameters of the loop transport and interaction model that affect the measurable quantities addressed by our calculations. We discuss and review the range of parameter values obtained by past analyses.

2.2.1. Acceleration Parameters

A fundamental property of accelerated ions is their energy spectrum. For the calculations performed here, we assume that the spectral form of the accelerated ions is an unbroken power law, with all ion species having the same index (here denoted by s), normalized to one proton with energy greater than 30 MeV. Gamma-ray and neutron observations provide various measures of the power law index. Ramaty et al. (1996) derived power law indexes for several flares observed with the Gamma Ray Spectrometer on the *Solar Maximum Mission* (*SMM*) using two such measures, the fluence ratio of the 6.129 MeV ^{16}O to the 1.634 MeV ^{20}Ne lines and the fluence ratio of the 2.223 MeV neutron capture line to the 4.438 MeV ^{12}C lines. For each flare, he found that the indexes derived with the two tests were the same, within their uncertainties (see the Ne/O discussion in §2.2.2). We will see in §2.4.4 that the first measure is relevant to accelerated ions with energies from a few to about 10 MeV nucleon^{-1} while the second is relevant to ions with energies from a few to as much as 100 MeV nucleon^{-1}, implying that the spectrum is an unbroken power law through this entire energy range.

In addition to using these measures in their analysis of OSSE data from the 1991 June 11 solar flare, Murphy & Share (2000) used an additional measure: the fluence ratio of the 0.511 MeV positron annihilation to the 4.438 MeV ^{12}C lines. We will show in §2.4.4 that this measure is relevant to accelerated ions energies from a few to a few tens of MeV nucleon^{-1}; i.e., between the energy ranges of the other two tests. They showed that there were time periods during the June 11 flare when the spectrum appeared to be an unbroken power law throughout the entire relevant energy range, but there were also periods when it was not, exhibiting a soft low-energy component and a hard high-energy component. Using similar spectral index measures as those above, we will show in this paper that the accelerated ion spectrum for the June 4 flare is again consistent with an unbroken power law up to ∼100 MeV nucleon^{-1} but, with the addition of neutron measurements also available for this flare (which are relevant to ion energies up to a GeV nucleon^{-1}; see §2.4.4), the spectrum must steepen above 100 MeV nucleon^{-1}.

In our calculations, we will vary the power law spectral index from 2 to 6. In their derivation of spectral indexes from 19 flares observed by *SMM*, Ramaty et al. (1996) found most indexes fell within this range, with an average of ∼4.2. Spectral indexes derived using recent data from 3 solar flares obtained with the *RHESSI* instrument have been harder, with indexes nearer to 3 or less.

The accelerated-ion composition used in the calculations is summarized in Table 2. We have assumed the "impulsive flare" accelerated-ion abundances defined by Ramaty et al. (1996) which reflects average heavy-element abundance enhancements found in impulsive

SEP events in space (Reames et al. 1994). Accelerated ion compositions derived from γ-ray line measurements (Murphy et al. 1991; Share & Murphy 1998, 1999; Mandzhavidze et al. 1999) have suggested that they are similar to those of such impulsive SEP events. The impulsive composition is coronal (Reames 1995) for C, N, Ne, Mg, Al, Si, S, Ca & Fe relative to O but with Ne/O, Mg/O, Si/O and S/O increased by a factor of 3 and Fe/O increased by a factor of 10. We will assume two values for α/proton: 0.1 and 0.5. For each, we will maintain α/O = 50 and ^{3}He/^{4}He = 1.

2.2.2. Physical Parameters

The ambient composition used in the calculations is also summarized in Table 2. We have assumed coronal abundances (Reames 1995) for C, N, O, Mg, Al, Si, S, Ca & Fe relative to H. Abundance determinations from analyses of γ-ray lines for several flares (Share & Murphy 1995; Ramaty et al. 1996) have shown that the composition of the γ-ray line production region is similar to coronal. These are the same ambient abundances used by Ramaty et al. (1996) except we assume ^{4}He/H = 0.10 rather than the coronal value of 0.037. Mandzhavidze et al. (1999) have shown that in some flares the ambient ^{4}He/H abundance ratio could be >0.1. Grevesse et al. (1996) list the photospheric ^{4}He/H as 0.097.

We have also taken Ne/O = 0.25. In their analysis of 19 SMM flares, Ramaty et al. (1996) showed that to maintain an unbroken power-law spectrum from ∼2 to ∼50 MeV nucleon^{-1}, the ambient Ne/O abundance ratio had to be ∼0.25, higher than the accepted photospheric value of 0.15. Similar Ne/O enhancements have been seen in other measurements of flare data; for example, Schmelz (1993) found Ne/O of 0.32 using observations of a solar flare obtained with the Flat Crystal Spectrometer on SMM. Drake & Testa (2005) found Ne/O = 0.41 for a sample of 21 stars located within 100 pc of the Sun that had been observed with the High Energy Transmission Grating on the Chandra X-Ray Observatory. But the Ne/O abundance ratio derived in a recent analysis of FCS data which excluded data taken during flares and long-duration events (Schmelz et al. 2005) was consistent with the accepted 0.15 value. Schmelz et al. (2005) also reconsidered older data obtained from full-Sun observations and again found Ne/O consistent with the accepted value. Considering that the Ne/O enhancements could be flare-related, Shemi (1991) suggested that pre-flare soft X-ray radiation preferentially ionizes Ne which could then be transported to higher levels of the atmosphere. Since the Chandra spectra analyzed by Drake & Testa (2005) are most likely dominated by photons from very intense flares, their enhanced neon abundances might result from a similar mechanism. However, Schmelz et al. (2005) point out that this is not likely since low-FIP elements in active stellar coronae are generally depleted rather

than enhanced, as they are in the solar corona. Here we will use the 0.25 value derived from the solar-flare γ-ray measurements.

We will investigate the effect on the measurable quantities for two models of the solar atmosphere: the sunspot region atmosphere of Avrett (1981), and a hybrid model that could be more similar to the atmosphere during an active period. In the sunspot model of Avrett, the density at heights greater than several hundred kilometers is more tenuous than that of the quiet Sun model of Vernazza et al. (1981), but below this height it is greater. During a flare, the atmosphere could be considerably different still (Share et al. 2004). Aschwanden et al. (2003) have used *RHESSI* measurements of electron bremsstrahlung to estimate the density-height profile in a solar flare and found that the density is enhanced relative to quiet Sun models at heights greater than ∼1000 km and the density scale height is considerably larger. We construct a hybrid solar-flare model (the "*RHESSI*/Avrett model") consisting of the Avrett density profile below 1000 km and the Aschwanden profile above. We use the Avrett sunspot model at photospheric heights since flare loop structures are generally found above sunspots (e.g., Hurford et al. (2003); Schrijver et al. (2006)). The enhanced chromospheric density during flares suggested by the *RHESSI* measurements could be due to filling of the loop by active processes prior to the main impulsive event. The two models, along with the Vernazza model, are shown in Figure 1 where the larger chromospheric density and scale height of the *RHESSI*/Avrett model is clearly seen. This is the first time that the dependence of solar-flare γ-ray and neutron production on the atmospheric model has been systematically explored, thus allowing the possibility to learn about the structure of the solar atmosphere during flares from high-energy measurements.

The parameters associated with the loop model are the level of PAS, the degree of loop magnetic convergence, and loop length. We will vary the level of PAS from none ($\lambda \rightarrow \infty$) to *saturated*. At saturation ($\lambda \approx 20$), further decrease of λ has no effect on the temporal or angular dependence of the interactions (see discussion below). We will vary the magnetic convergence from none ($\delta = 0$) to very strong ($\delta = 0.45$). For the Avrett (1981) atmosphere, $\delta = 0.1$ and 0.2 correspond to an increase of the magnetic field from the corona to the photosphere by factors of ∼5 and ∼20, respectively. The loop length will be varied by an order of magnitude from 11,500 to 115,000 km. Estimates of loop lengths based on hard X-ray timing and footpoint imaging (e.g., Aschwanden et al. (1996); White et al. (2002)) range from ∼10,000 to 80,000 km.

Nuclear reactions and the yields of the various products in solar flares are not influenced by the temperature of the interaction region. At the temperatures expected in solar flares, any deexcitation-line Doppler broadening is dominated by the recoil velocities of the excited nuclei resulting from the impact of the non-thermal accelerated particles. For the 4.438

MeV ^{12}C deexcitation line, the FWHM due to recoil is ∼80 keV, while even at 10^6 K the thermal FWHM is < 1 keV. The width of the 2.223 keV neutron-capture line does reflect the temperature of the region where the neutrons are captured since the neutrons are typically thermalized before capture, but since the captures occur deep in the photosphere where the temperature is $< 10^4$ K, the FWHM is ∼10 eV, much less than typical detector energy resolution at these energies. The yield of secondary positrons from production of radioactive nuclei and pions is similarly not influenced by the temperature, but the yield of the subsequent annihilation photons and the shape of the annihilation line is. Positron annihilation was thoroughly studied by Murphy et al. (2005).

2.2.3. Nuclear Interaction Cross Sections

The development of the theory of γ-ray line production motivated a systematic effort of laboratory measurements of production cross-sections for the most important lines in solar flares with resulting estimated uncertainties of less than 20% (e.g., Dyer et al. (1981, 1985)). The γ-ray production code developed by Ramaty et al. (1979) now includes over 100 individual lines. The cross sections for all of these lines have recently been re-evaluated and updated with new laboratory measurements (Kozlovsky et al. 2002). The cross sections are generally strongly peaked in the energy range 10–30 MeV nucleon^{-1}.

The γ-ray line production code includes accurate kinematics to calculate the direction of the recoil excited nucleus in the center-of-mass frame and the angular distribution of the γ-ray emission in the frame of the excited nucleus (see Ramaty et al. (1979) and the more recent work of Kiener et al. (2001)). Anisotropic emission in the excited nucleus rest frame generally will not affect line fluence determinations unless the accelerated particles are truly beamed. In addition, the velocities of the excited nuclei are generally too small to result in significant anisotropy of the emission in the frame of the Sun due to relativistic beaming. However, the velocities are large enough to produce measurable line Doppler shifts when the recoil angular distribution is sufficiently anisotropic.

In addition to the explicit γ-ray lines included in our deexcitation line code, nuclear reactions involving heavier nuclei also produce a large number of weaker, closely-spaced lines and a true nuclear continuum. This additional emission is currently included in the line production code according to the prescription given by Ramaty et al. (1979). We are currently improving this modeling using both measurements and calculations of this emission. Accurate modeling of this emission is not critical for the purposes of this paper since we will focus only on measurements of the strongest narrow lines.

Hua et al. (2002) thoroughly reevaluated and revised the neutron production cross sections and kinematics. With these new approximations for the angular- and energy-dependent cross sections, the calculated neutron yields are in much better agreement with laboratory measurements. The estimated uncertainties in the calculated neutron yield over the neutron energy range relevant to solar flare measurements is ∼30%.

2.3. Effect of the Acceleration and Physical Parameters on the Nuclear Interactions

Except for neutrons that escape from the Sun, the products of nuclear reactions (e.g., excited and radioactive nuclei, pions and neutrons) are not directly observable but reveal themselves through secondary processes producing emissions that *are* observable (e.g., deexcitation γ rays, annihilation γ rays after positron emission, pion-decay radiation, and neutron capture γ rays). The properties of an interacting accelerated ion that most significantly affect the measurable quantities associated with the observable emissions are (1) the time of the interaction after release from the acceleration region, (2) the ion direction of motion at interaction, (3) where in the loop the interaction occurs, and (4) the ion kinetic energy at interaction. The parameters listed in Table 1 combine to affect all of these properties to varying degree. In the following subsections we discuss how these interacting ion properties depend on the parameters, using calculations of the production of the 4.438 MeV excited state of ^{12}C for illustration. The results are qualitatively valid for other deexcitation lines and for neutron production. The total number of possible parameter combinations is too large to fully explore so the parameter ranges and values discussed are chosen to effectively convey the most important dependences. We discuss the interaction time history in §2.3.1, the interacting ion angular distribution in §2.3.2, and the distribution of the interactions in the loop in §2.3.3. We defer the discussion of the energies of the interacting ions to §2.4.4 after discussing the effect of the parameters on the various observable emissions resulting from the nuclear interactions in §2.4.1, 2.4.2 and 2.4.3.

In the following sections, figures are presented showing the dependence of the interacting ion properties on a particular acceleration or physical parameter. Except for the parameter being varied, and unless otherwise indicated, the other parameters will be held fixed at a set of standard values: α/proton = 0.5, $s = 4$, $\lambda = 300$, $\delta = 0.2$, L = 11,500 km, and the atmosphere of Avrett (1981).

2.3.1. Nuclear Interaction Rate Time History

The time history of the nuclear interaction rate is governed by both the time history of the ion acceleration release rate ($a_{\rm ion}(t)$) and transport in the loop. Here we will only consider the effects of transport, assuming instantaneous release of all particles at $t = 0$. (When the June 4 flare data are analyzed in §3, we will discuss estimates for $a_{\rm ion}(t)$.) In the absence of magnetic convergence ($\delta = 0$), ions do not mirror and the nuclear interaction time history depends only on the energy loss rate in the lower chromosphere and upper photosphere where the density is greatest and most of the interactions occur. In the presence of magnetic convergence ($\delta \neq 0$), ions with initial pitch angles lying close to the loop axis also do not mirror (they are within the "loss cone") and behave similarly. Ions outside the loss cone mirror and lose energy much more slowly as they traverse the low-density corona. These interactions thus occur on longer time scales, with the time scale increasing with increasing convergence. Figure 2a shows ^{12}C line production time histories for $\delta = 0.0$, 0.20, and 0.45. For the time histories with $\delta \neq 0$, the excesses at times less than 1 second are due to ions within the loss cone interacting on their first pass down the loop leg. For all of these calculations, we have assumed no PAS; i.e., $\lambda \rightarrow \infty$.

Pitch angle scattering causes the loss cone to be continuously repopulated. As a result, the nuclear interaction rate increases at early times and correspondingly decreases at later times. Figure 2b shows ^{12}C line production time histories for PAS levels of none ($\lambda \rightarrow \infty$), intermediate ($\lambda = 300$), and high ($\lambda = 20$). The time history is no longer affected by decreasing λ when the rate of loss-cone replenishment exceeds the rate of nuclear reactions in the loss cone. This saturation effect occurs for λ less than $\sim$20.

Increasing the loop length increases the time scale of the interaction rate since mirroring particles spend more time at lower coronal densities where nuclear reactions are less likely. Figure 2c shows the effect on the interaction time history due to loop length. The delays of the excesses at $\sim$1 second and less (for ions within the loss cone interacting on their first pass down the loop leg) are directly due to the longer transit times resulting from the longer loop lengths .

The accelerated ion spectral index has no significant affect on the interaction rate time history at times later than about 1 second after particle release. However, in harder spectra there is a larger fraction of ions with higher energies producing the reactions (see §2.4.4). Before about 1 second, this results in ions arriving earlier at the footpoints on their first transport down the loop leg. This can be seen in Figure 2d where time histories for $s = 3$, 4 and 5 are shown. Similarly, different energy dependences of the interaction cross sections affect the time history only before about 1 second.

The differences of the Avrett and Vernazza atmospheric models have negligible effect on the interaction time history. Only when the model is significantly different, such as the *RHESSI*/Avrett model, is the time history affected, with a shortened time scale due to the dramatic chromospheric and lower-corona density enhancement as shown in Figure 2e. Another aspect of the time history dependence on the atmospheric model is shown in Figure 2f. At times less than a few seconds, the extent of the variation of the time history as PAS is varied from none to saturated is significantly less for the *RHESSI*/Avrett model than it is for the Avrett model. A similar reduced extent of the variation is found as δ is varied. This will impact the ability to distinguish among possible values of δ and λ when data from the June 4 flare are analyzed in §3.1 under the assumption of the *RHESSI*/Avrett model.

2.3.2. Interacting Ion Angular Distribution

As mentioned in §2.1, calculations based on the loop model produce angular distributions for the interacting ions that can be related to physical parameters, in contrast to the *ad hoc* distributions assumed previously. In the absence of magnetic convergence ($\delta = 0$), there is no mirroring and the angular distribution of the interacting ions (initially isotropic when released at the top of the loop) will be downward isotropic regardless of level of PAS or loop size. In the presence of magnetic convergence ($\delta \neq 0$) but no PAS ($\lambda \rightarrow \infty$), ions with pitch angles too small to mirror enter the "loss cone" and either undergo a nuclear reaction as they are moving downward or are thermalized. But most ions have larger initial pitch angles which results in mirroring and the interactions occur mostly at the ion mirror points where the density is greatest. Thus, most ions are moving parallel to the solar surface when they interact (i.e., a "fan beam" angular distribution; see, e.g., Hua & Lingenfelter (1987b)) with a relatively small contribution from downward-moving ions. The downward contribution becomes even less important as δ increases. Figure 3a shows the affect of magnetic convergence on the interacting ion angular distribution for $\delta = 0.0$, 0.20 and 0.45. For all of these calculations, there is no PAS ($\lambda \rightarrow \infty$).

By continuously repopulating the loss cone, the effect of PAS is to produce more interactions involving downward-directed ions. This is seen in Figure 3b where angular distributions are shown for the same convergences as Figure 2a ($\delta = 0.0$, 0.20 and 0.45) but for $\lambda = 300$. As PAS is increased (λ decreased), more ions interact in the loss cone and the distribution becomes more downward-directed until saturation is reached ($\lambda \sim 20$). This is shown in Figure 3c for $\lambda \rightarrow \infty$, $\lambda = 300$, and $\lambda = 20$.

The angular distribution of the accelerated ions when they interact is not significantly affected by the spectral index or the energy dependence of the interaction cross section. The

distributions produce by the three atmospheric models considered here (Vernazza, Avrett, and *RHESSI*/Avrett) were also very similar, except for low levels of PAS (large λ) where the *RHESSI*/Avrett distribution had a slightly enhanced downward-directed component resulting from enhanced interactions of particles within the loss cone.

2.3.3. Interaction Depth Distribution

In the absence of magnetic convergence ($\delta = 0$), there is no mirroring and the depth distribution directly reflects the grammage required for the accelerated particles to interact as they move downward through the solar atmosphere. In the presence of magnetic convergence ($\delta \neq 0$), mirroring results in interactions occurring at higher elevations (and therefore lower densities) as more and more particles are prevented from penetrating the lower atmosphere. This is seen in Figure 4a where the fraction of interactions occurring deeper than a given density is plotted versus density in the solar atmosphere for $\delta = 0.0$, 0.20 and 0.45.

Even with minimal convergence, the lack of PAS ($\lambda \rightarrow \infty$) results in a significant fraction of the interactions occurring at low densities. This can be seen in Figure 4b where depth distributions for no PAS ($\lambda \rightarrow \infty$), $\lambda = 300$ and saturated PAS ($\lambda = 20$) are shown. The curve for no PAS shows that almost 20% of the interactions occur at densities less than 10^{10} H cm^{-3}. As PAS is increased (λ decreased), the bulk of the interactions move to higher densities as more interactions occur within the loss cone.

Because the nuclear interactions occur predominantly at chromospheric depths or greater, transport through the low density corona has little effect on where the interactions will ultimately occur. As a result, the effect of loop length on the interaction depth distribution is minimal, as long as the other parameters are not changed. Specifically, to maintain the relative level of PAS in the calculations when the loop length is increased, the physical scattering mean free path (Λ) must be increased accordingly. For a fixed Λ, however, increasing the loop length results in decreasing λ, the effect of which was discussed above.

Because higher-energy ions tend to interact farther along their paths, harder particle spectra result in interactions occurring at higher densities since more ions of higher energies are producing the interactions (see §2.4.4). This is seen in Figure 4c for $s = 3$, 4 and 5.

When the depth distribution is considered as a function of atmospheric density, the effect of different atmospheric density profiles is minimal as seen in Figure 4d where the depth distribution is shown for the three models considered here (Vernazza, Avrett, and *RHESSI*/Avrett). This is due partly to the fact that for convenience we have parameterized the magnetic convergence in terms of the pressure so that, for a given δ, the mirror point

tends to remain near the same density as the atmospheric model is changed. In terms of physical depth, however, the distribution does change significantly as the model is changed, as seen in Figure 5 where the distribution as a function of depth in the atmosphere is shown for the three model atmospheres.

Interactions whose cross sections have high thresholds tend to interact at higher densities, again the consequence of the longer ranges of higher-energy ions. This is seen in Figure 4e where the depth distributions for interactions with two different cross section energies are shown: a low threshold energy ($\sim$1 MeV nucleon^{-1}, similar to that of the 1.634 MeV ^{20}Ne deexcitation line) and a high threshold energy ($\sim$25 MeV nucleon^{-1}, similar to those of neutron-producing p-α reactions).

This dependence of the depth distribution on the interaction cross section also explains why the distribution is affected by the accelerated α/proton ratio, as shown in Figure 4f. This dependence results from the different threshold energies of the α and proton cross sections for producing the 4.438 MeV excited state of ^{12}C. The α-particle interactions have a lower threshold and, as just discussed, such interactions occur at lower densities (see Figure 4e). When the α/proton ratio is high, a larger fraction of the line yield is due to such reactions and the depth distribution shifts to lower densities.

2.4. Effect of the Acceleration and Physical Parameters on the Observable Quantities

In §2.3 we discussed how the various acceleration and physical parameters affect those aspects of the nuclear interactions that most significantly affect the subsequent observable emissions. In the next three sub-sections we discuss how the parameters affect the measureable quantities associated with deexcitation lines, escaping neutrons and the neutron capture line, respectively. In a final sub-section we discuss what accelerated ion energies are responsible for each of these emissions.

2.4.1. Deexcitation Line Production

In this section we discuss the measurable quantities associated with "narrow" nuclear deexcitation lines produced by accelerated proton and α-particle interactions with ambient C and heavier nuclei. For such deexcitation lines, the measurable quantities are the line fluence, shape, central energy and emission time history. How the acceleration and physical parameters affect each of these quantities is discussed.

Deexcitation Line Yields and Yield Ratios

The only physical parameter significantly affecting time-integrated narrow deexcitation line yields (and also, therefore, line ratios) is the relative abundances of the ambient elements heavier than He. Yields are not affected by the physical parameters associated with the loop itself, such as length, PAS or magnetic convergence. This is because in the loop model accelerated ions do not escape from the loop so the interactions are "thick target" overall. In addition, the lines are not produced sufficiently deep in the solar atmosphere for significant attenuation to occur. Only when the flare is located at or beyond the limb of the Sun is there any significant attenuation of any line. Also, the interacting angular distribution does not significantly affect line ratios because the recoil velocities of the excited nuclei are non-relativistic so there is no significant beaming of the emission. The anisotropic emission of photons in the rest frame of the recoil nucleus is significant only for very beamed distributions. Therefore, calculated total production yields and yield ratios can be used for flares occurring anywhere on the solar disk.

The acceleration parameters that affect narrow deexcitation line yields (and ratios) are the accelerated α/proton ratio and the spectral index. Both accelerated protons and α particles contribute to essentially all reactions producing excited nuclei via direct excitation or spallation and the relative contributions from the two particles vary according to the α/proton ratio and the spectral index (through the reaction cross sections). The acceleration parameters that affect the relative intensities of broad deexcitation lines are the accelerated ion composition and the spectral index. The only physical parameter affecting broad deexcitation line yields and line ratios is the ambient He/H ratio.

Using the updated cross sections of Kozlovsky et al. (2002), we show in Figure 6 the yields of the 1.634 MeV ^{20}Ne, 4.438 MeV ^{12}C and 6.129 MeV ^{16}O lines as functions of the accelerated-ion power-law spectral index for $\alpha/\mathrm{p} = 0.1$ (thin curves) and 0.5 (thick curves). These yields include the direct excitation reactions and all spallation reactions producing the excited nucleus. While each of these yields is dominated by the line of the nucleus noted, we also include weaker lines at close-lying central energies. Specifically, the 1.634 MeV ^{20}Ne yield also includes the lines at 1.600 from ^{23}Mg, 1.635 MeV from ^{14}N and 1.636 MeV from ^{23}Na in addition to the ^{20}Ne line. The 4.438 MeV ^{12}C yield also includes the 4.444 MeV line from ^{11}B in addition to the ^{12}C line. The 6.129 MeV ^{16}O yield also includes the 6.175 MeV line from ^{15}O, the 6.322 MeV line from ^{15}N and the 6.337 and 6.476 MeV lines from ^{11}C in addition to the ^{16}O line. Including these additional lines is appropriate when comparing these calculated yields with yields measured with medium-resolution NaI detectors such as OSSE and *SMM*. Higher-resolution detectors such as *RHESSI* may be able to separate the individual lines. The shapes of the curves in Figure 6 result from (1) the relationship between

the accelerated ion spectrum and the energy dependence of the cross section (of the main line and also of the additional lines included in the yield) and (2) the normalization of 1 proton above 30 MeV. The minimum exhibited by the curves is an artifact due to this normalization and the index at which the minimum occurs changes as the normalization energy is changed. The choice of this normalization energy is arbitrary and is set at 30 MeV because that is near the energy where many of the deexcitation line production cross sections peak.

As first suggested by Lingenfelter & Ramaty (1967), the fluence ratio of two lines whose production cross sections have markedly different energy dependences is sensitive to the steepness of the accelerated-ion spectrum. The 6.129 MeV ^{16}O and the 1.634 MeV ^{20}Ne lines are uniquely useful in this way because (1) the threshold for the ^{20}Ne line is unusually low ($\sim$2 MeV for proton reactions and $\sim$1 MeV nucleon^{-1} for α reactions) and is very different from that of the ^{16}O line ($\sim$7 MeV for proton reactions and $\sim$2.5 MeV nucleon^{-1} for α reactions), (2) they are both strong lines, and (3) they both arise from elements with high FIP and are therefore expected to be free of the abundance variations associated with low FIP elements (Murphy et al. 1991; Share & Murphy 1995; Ramaty et al. 1995). In addition to the time-integrated measure of the spectral index, the time dependence of the ratio also provides an instantaneous measure because both of these lines are prompt (the halflives of the excited nuclei being $< 10^{-10}$ s). (Note: there is no significant difference of the interaction time histories due to the different energy dependences of the cross sections; see §2.3.1.) Using this technique, power-law spectral indexes have been determined for a number of flares observed by several detectors over the past two solar cycles (e.g., Ramaty et al. 1996, Murphy et al. 1997, Ramaty & Mandzhavidze 2000). This ratio was used by Ramaty & Mandzhavidze (2000) to establish the near energy equivalency of accelerated ions and electrons.

Figure 7 shows the yield ratio of the 6.129 MeV ^{16}O and 1.634 MeV ^{20}Ne lines as a function of power-law spectral index for α/p = 0.1 (thin curves) and 0.5 (thick curves). Over the spectral index range relevant for solar flares, this line ratio varies by almost an order of magnitude. Because of the lower threshold energies of α-particle reactions, line production for hard accelerated particle spectra are dominated by proton interactions and there is little difference between the ratios for α/proton = 0.1 and 0.5. As the spectrum softens, the contribution from α-particle interactions increases and the ratios differ.

Accelerated α particles can interact with ambient He to produce excited states of ^{7}Be and ^{7}Li. These states then deexcite to produce lines at 0.478 MeV and 0.429 MeV which, through Doppler broadening, generally merge into what is known as the "$\alpha - \alpha$ complex". Since the complex is produced purely by accelerated α particles, the ratio of its yield to the yield of other deexcitation lines (which are generally produced by both protons and α

particles) is very sensitive to the accelerated α/proton ratio in addition to its dependence on the accelerated ion spectrum. We show in Figure 6 the yields for this complex as a function of spectral index for $\alpha/\mathrm{p} = 0.1$ (thin curves) and 0.5 (thick curves). We show in Figure 8 the corresponding yield ratios of the $\alpha - \alpha$ complex and the sum of the strongest high-FIP lines (1.63, 4.44, 6.13 and ∼7 MeV lines from ^{20}Ne, ^{12}C, ^{16}O, and ^{16}O, respectively, as a function of spectral index. The shape of this curve is due to the different energy dependences of the cross sections. The cross sections for producing the ^{7}Li and ^{7}Be lines are both sharply peaked with threshold energies of about 10 MeV nucleon^{-1} and falling to insignificance by 100 MeV nucleon^{-1}. In contrast, the cross sections for producing the 4.44 MeV ^{12}C line from both accelerated protons and α particles have lower thresholds (∼5 MeV for proton reaction and 1–2 MeV nucleon^{-1} for α reactions) and also extend to higher energies and this is generally true for the other lines as well. As a result, the yield of the 4.44 MeV line is relatively large for steep spectra due to the lower threshold energy and also large for hard spectra due to the extension to high energy, with a minimum for intermediate spectra.

Deexcitation Line Shapes and Central Energies

The acceleration parameters that most significantly affect the shapes and line shifts of the narrow deexcitation lines are the α/proton ratio and the steepness of the accelerated-particle spectrum (the index s for power-law spectra). The effect on the shape of the line is illustrated in Figure 9a with line profiles of the 4.438 MeV ^{12}C line for an isotropic interacting-particle angular distribution. Because the angular distribution is assumed isotropic, the shape is symmetrical about the rest energy of the line (indicated by the vertical line). The solid and dotted curves are for interactions due to protons and α-particles, respectively. The thick and thin curves are for power-law spectral indexes of 2.75 and 4.75, respectively. (Note: the profiles have been renormalized to facilitate comparison.) For both proton and α-particle interactions, a harder spectrum results in a broader line because there are more interactions involving higher-energy accelerated particles and such particles produce larger Doppler shifts due to the faster recoiling nuclei. Similarly, α-particle interactions produce a broader line because the larger α-particle mass also results in faster recoil velocities.

The final shape of the line depends on the relative contribution of the accelerated proton and α-particle reactions which depends on the accelerated α/proton ratio and how the relative yields depend on spectral index through their respective production cross sections. Because the cross sections of α-particle reactions tend to have lower threshold energies, steeper accelerated-particle spectra tend to increase the relative α-reaction yield. For the 4.438 MeV ^{12}C line, Figure 10 shows the ratio of the yield from α particles to the yield from protons as a function of spectral index for equal numbers of accelerated α particles and

protons. Figure 11 shows the final resulting line shapes for $s = 3.75$ and α/proton ratios of 0.1 and 0.5. Although a harder spectrum produces broader lines, the contribution of the inherently broader α reaction decreases so that the overall line width may in fact be narrower depending on the α/proton ratio.

The physical parameters that affect the shapes and shifts of the narrow deexcitation lines are those that affect the angular distribution of the interacting particles: most significantly the level of convergence (δ) and PAS (λ) and to a lesser degree the atmospheric model. Figure 9b illustrates the effect on the ^{12}C line profile for $\delta = 0.20$ and saturated PAS ($\lambda = 20$) for a flare centered on the solar disk ($\theta_{\rm obs} = 0°$). Again, the solid and dashed curves are for interactions due to protons and α-particles, respectively and the thick and thin curves are for power-law spectral indexes of 2.75 and 4.75, respectively. This downward-directed angular distribution (see Figure 3) results in red-shifted lines, with both harder spectra and α particles producing the most Doppler shift. Details of the line shape and shift will vary with different combinations of δ, λ, s, and accelerated α/proton ratio. The extreme case of a 100% downward-beamed angular distribution for a disk-centered flare is shown in Figure 9c. As discussed in §2.3.2, the *RHESSI*/Avrett atmosphere produces a slightly enhanced downward component for combinations of δ and λ resulting in mirroring (i.e., fan-beam) distributions. This results in a slightly increased line red shift for such distributions. For example, at the 74.5° June 4 flare location with $\lambda = 0$ and $\delta = 0.45$, the 4.438 MeV ^{12}C line is red-shifted 3 keV more for the *RHESSI*/Avrett atmosphere than for the Avrett atmosphere.

For any angular distribution with some downward-directed component, as the flare location moves away from Sun center, the amount of Doppler shift will decrease. This is illustrated in Figure 12 where ^{12}C line profiles are shown for a flare occurring at a heliocentric angle of $\theta_{\rm obs} = 74.5°$ (as for the 1991 June 4 flare). Profiles resulting from three angular distributions are shown: isotropic, saturated PAS, and downward beam. For these calculations, the α/proton ratio is 0.5 and $s = 4$. At 74.5°, only the extreme case of a 100% downward beam produces any significant Doppler shift of the line.

Deexcitation Line Time History

Because the lifetimes of the excited states are very short ($< 10^{-6}$ s), photon emission is prompt, with virtually no delay between the nuclear interaction and the appearance of the γ ray. As a result, a measured deexcitation line emission time history will be essentially identical to the nuclear interaction time history. The parameters that affect the interaction time history (and thus the delay of γ-ray emission relative to accelerated particle release) were discussed in §2.3.1. The only acceleration parameter that affects the interaction time history is the ion acceleration release time history, $a_{\rm ion}(t)$. The most significant physical

parameters affecting the time history are the magnetic convergence, the level of PAS and the loop length.

2.4.2. Neutron Production and Escape

In this section we discuss the measurable quantities associated with flare-produced neutrons escaping from the Sun and observed by detectors in space or on Earth. The measurable quantities are the energies of the neutrons and their arrival times; i.e., the time-dependent energy spectra of the arriving neutrons. These spectra are modified from the spectrum of neutrons that escaped from the Sun by both velocity dispersion of the neutrons with various energies and decay of the neutrons during transport. How the acceleration and physical parameters affect the time-dependent escaping neutron spectrum was discussed by Hua et al. (2002). We summarize some of their results here and further discuss some other aspects of neutron production. A fraction of those neutrons initially produced traveling in a downward direction can be captured on H to produce deuterium and the 2.223 MeV neutron-capture line which is discussed in §2.4.3.

Total Neutron Production

The acceleration parameters that affect the total neutron yield are the accelerated particle spectral index and composition, particularly the accelerated α/proton ratio. The only physical parameter affecting the total yield is the ambient composition. Total neutron production as a function of accelerated-ion spectral index is shown in Figure 13 for α/proton = 0.1 (thin curves) and 0.5 (thick curves). These total yields are similar to those given by Ramaty et al. (1996) (who also used the updated total cross sections of Hua et al. 2002) except for steep spectra where the yields calculated here are $\sim$30% larger due to our larger assumed ambient He/H abundance. Using the loop formalism of Hua et al. (1989) and Hua et al. (2002), we confirmed that this *total* neutron yield is independent of parameters of the loop model as expected. For softer spectra, neutron production is dominated by α-particle reactions and the dependence of the yield on the α/proton ratio is almost linear. The explanation for the shapes of the yield curves is the same as for the deexcitation lines which is discussed in §2.4.1.

Neutron Spectra

In the analysis of neutrons from solar flares, there are three relevant energy spectra of neutrons that must be considered: the spectrum at the production site, the spectrum escaping

from the Sun, and the spectrum arriving at Earth. As for total neutron production, the angle-integrated spectrum of neutrons at the production site is independent of parameters of the loop model, depending only on the accelerated-particle spectrum and the ambient and accelerated-ion compositions. Neutrons are produced in proton–proton, $\alpha - \alpha$, proton$-\alpha$ and $\alpha-$proton reactions and reactions of protons and α particles with heavier ambient nuclei and their inverse reactions. The threshold energies for these various reactions (see Hua et al. (2002) for the full cross sections) are given in Table 3 and span a broad range of energies from about an MeV nucleon^{-1} for reactions involving heavy nuclei to several hundred MeV for proton–proton reactions. Which reactions dominate neutron production at a given neutron energy depends on the accelerated-ion spectrum and the composition of the accelerated ions and the ambient medium.

Angle-integrated spectra at the production site are shown in Figure 14, calculated for an accelerated-ion power-law spectral index of 4, saturated PAS, $\delta = 0.2$, the compositions of Table 1, and both accelerated α/proton = 0.5 (Panel a) and 0.1 (Panel b). Also shown are the contributions from the various reactions. The shapes of the total spectra for the two values of α/proton are similar, but the overall yield is less for α/proton = 0.1, as shown in Figure 13. For this spectral index, the main contribution to the production of high-energy (>1 GeV) neutrons is from accelerated α-particle reactions with ambient H for α/proton = 0.5, but it is from accelerated proton reactions with ambient H and He for α/proton = 0.1. For both values of α/proton, the main contribution to production of neutrons with energies of tens of MeV is from α-particle reactions with ambient H. Referring to the thresholds of Table 2, these α particles must have energies greater than 10 MeV nucleon^{-1}. For accelerated α/proton = 0.5, the main contribution to low-energy (<10 MeV) neutrons is from α reactions with ambient He and heavier nuclei. Because of the very low threshold for the latter reactions, some of these low-energy neutrons can be produced by α particles of only a few MeV nucleon^{-1}. For α/proton = 0.1, most of the low-energy neutrons are produced by accelerated proton interactions with ambient He. From Table 2, the energies of these protons must be >30 MeV. As the assumed accelerated-ion spectrum steepens, the contribution of the low-threshold α–heavy reactions begins to dominate. We note that the combined yield of neutrons from reactions of accelerated protons with ambient C and heavier nuclei and their inverse reactions (the dashed-dot-dot curves in Figure 14) increases as accelerated α/proton is increased even though the reactions do not involve accelerated α particles. This is because we maintain accelerated α/O at 50, as stated in §2.2.1 which affects the yields of the inverse reactions. The relative contribution of the various reactions to *total* neutron production is independent of the loop parameters such as PAS, magnetic convergence, and length.

Because most of the neutrons are produced at densities where scattering is small (see

Figure 9 of Hua et al. (2002)), neutrons initially produced moving upwards typically escape from the solar atmosphere without scattering. Neutrons moving downwards typically lose their energy with little chance of escape. As discussed by Hua et al. (2002), while low-energy neutrons tend to be produced isotropically, higher-energy neutrons tend to be emitted more in the same direction as the interacting ion, with this tendency increasing with increasing ion energy. As a result, the spectrum of neutrons escaping from the Sun along a particular line of sight depends on the energy and angular distributions of the interacting accelerated ions. As discussed in §2.3.2, the physical parameters that affect the angular distribution of the interacting ions are the level of convergence (δ) and PAS (λ). In panel a of Figure 15 we show the angular-dependent kinetic-energy spectra of escaping neutrons calculated for an accelerated-ion spectral-index of 4, convergence $\delta = 0.2$, and both saturated ($\lambda = 20$, dashed) and no ($\lambda \rightarrow \infty$, solid) PAS. For loops perpendicular to the solar surface, θ is the angle between the normal to the solar surface and the line of sight and corresponds to the heliocentric angle of the flare, $\theta_{\rm obs}$. At each angle, the number of escaping neutrons from saturated PAS is less than that from no PAS since fewer neutrons are produced moving upwards with saturated PAS.

In panel b of Figure 15 we show the angular-dependent kinetic-energy spectra of escaping neutrons calculated for an accelerated ion spectral index of 4, $\lambda = 300$, and two values of magnetic convergence, $\delta = 0.20$ (solid) and 0.45 (dashed). The effect is similar to that for PAS, with the more downward-directed angular distribution of $\delta = 0.2$ resulting in fewer neutrons directed upwards. The broader interacting-ion angular distribution of $\delta = 0.45$ (see Figure 3) results in a weaker dependence of the escaping neutron spectrum on angle.

Neutron Production Time History

The effects of the acceleration and physical parameters on the delay of the production of neutrons relative to the accelerated ion release are qualitatively the same as those described for the 4.44 MeV ^{12}C deexcitation line (§2.2.1). The affects of PAS on the time dependence of neutron production were specifically discussed by Hua et al. (2002).

2.4.3. Neutron-Capture Line Production

In this section we discuss the measurable quantities associated with the 2.223 MeV neutron capture line: the line yield and time history. Neutrons initially produced moving downward either decay, react with ^{3}He, or are captured on H. Capture on other nuclei is less important due to their smaller relative abundances. The reaction with ^{3}He is charge

exchange, ^{3}He$(n,p)^3$H, without the emission of radiation. The capture on H results in the formation of deuterium with the binding energy appearing as a 2.223 MeV photon. Since the probability for elastic scattering is much larger than the probability for either of these reactions, most of the neutrons thermalize first, causing a delay in the formation of the capture photon relative to neutron formation. This delay is in addition to the delay of neutron production relative to the accelerated ion release discussed in §2.4.2.

The cross sections for the H and ^{3}He reactions are 2.2×10^{-30} β^{-1} cm^2 and 3.7×10^{-26} β^{-1} cm^2, respectively, where β is neutron velocity in units of the speed of light. Therefore, if the ^{3}He/H ratio at the capture site is $\sim 5 \times 10^{-5}$ (comparable to that observed in the solar wind), nearly equal numbers of neutrons will be captured on H as react with ^{3}He. The ambient ^{3}He/H abundance ratio affects not only the total yield of the capture line but also the delay of its formation.

In the next section we calculate 2.223 MeV neutron-capture line yields and in the following section neutron-capture line time histories. We explore their dependences on the acceleration and physical parameters.

Neutron-Capture Line Yield

The total neutron capture line yield depends directly on the total neutron yield and so, in addition to ambient ^{3}He/H, it also depends on the same acceleration and physical parameters affecting total neutron production: accelerated particle spectral index and ambient and accelerated particle compositions. Because the probability for capture depends on the initial direction of the neutron through the atmosphere, the capture line yield also depends on the physical parameters affecting the interacting ion angular distribution, δ and λ, because it determines the subsequent neutron angular distribution. Because effective capture requires high density, the capture line is produced deep in the photosphere resulting in strong attenuation of the line, especially if the flare is located near the solar limb. Therefore, while deexcitation line yields do not depend on the location of the flare on the solar surface (see §2.4.1), the neutron-capture line yield does.

Capture-line yields for a flare occurring near the center of the solar disk are shown in Figure 13 as functions of the power-law spectral index for α/proton = 0.1 (thin curves) and 0.5 (thick curves). For each value of α/proton, the yields are shown for two extreme values of PAS: no PAS ($\lambda \rightarrow \infty$, dashed curves) and saturated PAS ($\lambda = 20$, dotted curves). For each of these PAS values, yields for two extreme values of magnetic convergence are shown: $\delta = 0.0$ (i.e., none) and $\delta = 0.45$. For these calculations, the loop length is 11,500 km, the atmosphere is Avrett (1981), and ^{3}He/H $= 3.7 \times 10^{-5}$. As for the deexcitation line and

neutron yields, the shape of a curve results from (1) the relationship between the spectrum and the energy dependence of the cross section and (2) the normalization of 1 proton above 30 MeV. We see that the yield is larger for saturated PAS than for no PAS since the more downward-directed neutrons from PAS are more likely to be captured than decay. Similarly, the yields are larger for smaller values of convergence, again due to the more downward-directed angular distribution. We note that this is in contrast to the escaping neutron yield discussed in §2.5 which is less for more downward-directed angular distributions.

The ambient ^{3}He/H ratio has a strong affect on the neutron-capture line yield as the non-radiative reactions with ^{3}He compete with the line-producing captures on H. As ^{3}He/H is increased from 3.7×10^{-5} to 10×10^{-5}, the yield decreases by ∼50% and when ^{3}He/H is decreased to 0, the yield increases by ∼50%. Up to heliocentric angles of 85°, the dependence of the yield on ^{3}He/H is fairly independent of interacting particle angular distribution (i.e., λ and δ), spectral index, accelerated α/proton ratio, and atmospheric model.

We found that the effect of the atmospheric model on the total yield was relatively weak, with the most significant differences occurring for combinations of δ and λ producing mirroring (i.e., fan-beam) distributions of the interacting ions (and resulting neutrons). The fate of downward-moving neutrons is fairly insensitive to the atmospheric structure, but the relative probabilities for capture and decay for neutrons moving parallel to the surface depend on the amount of material the neutrons encounter. The higher density of the *RHESSI*/Avrett model at the higher elevations resulted in higher capture line yields for the fan-beam angular distributions. For parameter combinations resulting in strongly downward distributions, the yields from the Avrett and *RHESSI*/Avrett models were the same, regardless of flare location. The yields from the Vernazza model were as much as 10% less, with the largest difference occurring for limb flares. For parameter combinations resulting in more fan-beam distributions, the yields from the Avrett model were ∼10% less than from the *RHESSI*/Avrett model, independent of flare location. The yields from the Vernazza model were from 15 to 20% less than the *RHESSI*/Avrett model, independent of heliocentric angle. These effects were not significantly dependent on ^{3}He/H.

Because of the very different energy dependences of deexcitation line and neutron production cross sections, the fluence ratio of the neutron-capture line and a deexcitation line is very sensitive to the accelerated-ion spectral index. Corresponding to the yields shown in Figure 13, neutron-capture/4.438 MeV ^{12}C line fluence ratios as a function of power law spectral index for a flare occurring near the center of the solar disk are shown in Figure 7 for α/proton = 0.1 (thin curves) and 0.5 (thick curves). For each value of α/proton, the yields are shown for two extreme values of PAS: no PAS ($\lambda \rightarrow \infty$, dashed curves) and saturated PAS ($\lambda = 20$, dotted curves). For each of these PAS values, yields for two extreme values of

magnetic convergence are shown: $\delta = 0.0$ (i.e., none) and $\delta = 0.45$. The ratios vary by more than two orders of magnitude as the index is varied and are significantly more sensitive and cover a wider accelerated-ion energy range than the 6.129 MeV ^{16}O/1.634 MeV ^{20}Ne ratio (see §2.4.4). Since the neutron-capture line is delayed by ∼100 s due to the time required by the neutrons to slow down and be captured (see below), this ratio generally is only used to provide flare-averaged spectral indexes For these calculations, ^{3}He/H $= 3.7 \times 10^{-5}$.

The neutron-capture line originates in the photosphere (in contrast to nuclear deexcitation lines which probably originate at chromospheric densities) and is significantly attenuated for flares that occur near the solar limb. We show in Figure 16 neutron-capture/4.438 MeV ^{12}C line ratios as functions of flare heliocentric angle, parameterized by spectral index, and calculated for accelerated α/proton = 0.5, ^{3}He/H $= 3 \times 10^{-5}$, and no PAS ($\lambda \rightarrow \infty$; panel a), nearly-saturated PAS ($\lambda = 300$; panel b), and saturated PAS ($\lambda = 20$; panel c). The neutron-capture line is strongly attenuated for flares occurring at heliocentric angles greater than ∼75°: relative to a disc-centered flare, the neutron-capture/4.438 MeV ^{12}C line ratio decreases by an order of magnitude by 88° and two orders of magnitude by 90°.

We estimate the uncertainty of the neutron-capture yield due to uncertainty in the neutron production cross sections to be ∼20%.

Neutron-Capture Line Time History

Because both the probability for capture and the time to thermalize before capture depend on the initial direction of the neutron through the atmosphere, the capture line time history depends on the physical parameters affecting the interacting particle angular distribution: λ and δ. In panel a of Figure 17 we show neutron-capture line time histories calculated for instantaneous release of accelerated ions at the top of the loop at $t = 0$ for various values of PAS, from $\lambda \rightarrow \infty$ (none) to $\lambda = 20$ (saturated). (We note that these time histories, and the other time histories shown in this section, include the delay of neutron production relative to the initial ion release.) For these calculations, accelerated α/proton = 0.5, ^{3}He/H $= 3.7 \times 10^{-5}$, and $\theta_{\rm obs} = 75°$ (where $\theta_{\rm obs}$ is the heliocentric angle of the flare). As PAS decreases (λ increases), the interacting-particle angular distribution (and corresponding neutron distribution) become less downward-directed and the time history becomes more prolonged. Similarly, the angular distribution becomes less downward directed as δ decreases and the time history again becomes more prolonged, as shown in panel b of Figure 17 (for $\lambda = 300$).

Because harder accelerated particle spectra produce more high energy neutrons which penetrate to higher densities with increased probability for capture, the capture line time

history also depends on the accelerated particle spectral index. This is shown in panel c of Figure 17 for several values of spectral index s. Harder spectra result in a faster falling time history. For these calculations, accelerated α/proton = 0.5, ^{3}He/H = 3.7×10^{-5}, and $\theta_{\rm obs}$ = 75°. Also apparent is the strong dependence of the total line yield on spectral index.

The non-radiative reaction with ^{3}He competes with neutron capture on H and affects the neutron-capture line time history. This is seen in panel d of Figure 17 where time histories for several values of ^{3}He/H are shown. Increased ^{3}He results in a faster falling time history as neutrons are more rapidly removed. For these calculations, accelerated α/proton = 0.5 and $\theta_{\rm obs}$ = 75°.

Neutrons that penetrate deeper in the photosphere are captured sooner due to the higher density, but the subsequent capture line photons are more strongly attenuated. For flares located nearer to the solar limb, this attenuation becomes even stronger, resulting in slower time histories as photons from the more-rapid captures are attenuated. This can be seen in panel e of Figure 17 where we show capture-line time histories for flares located at disk center (0° heliocentric angle), 75° and 85°. Also apparent is the strong decrease of the total line yield with increasing angle. For these calculations, accelerated α/proton = 0.5 and ^{3}He/H = 3.7×10^{-5}.

We found that the effect of the atmospheric model on the neutron-capture line time history was relatively weak, with the most significant differences occurring for combinations of δ and λ resulting in interacting particle (and resulting neutron) angular distributions that were the least downward directed. Similar to the total capture line yield as noted above, the fate of downward-moving neutrons is fairly insensitive to the atmospheric structure, but the relative probabilities for capture and decay for neutrons moving parallel to the surface depend on the amount of material the neutrons encounter. The higher density of the *RHESSI*/Avrett model at the higher elevations results in a faster decay of the time history for fan-beam distributions. This can be seen in panel f of Figure 17 where we show time histories calculated for the Avrett and the *RHESSI*/Avrett atmospheres. Here we assume δ = 0.2 and λ = 1000 which results in a fan beam angular distribution (see panel c of Figure 3). For the other parameters, accelerated α/proton = 0.5, ^{3}He/H = 3.7×10^{-5}, and $\theta_{\rm obs}$ = 75°.

2.4.4. Effective Energies of the Accelerated Ions Producing Gamma Rays and Neutrons

In the previous sections we have explored the dependences of the various measurable quantities of flare emissions on the acceleration and physical parameters. When deriving

these parameters from measured observables, it is important to be aware that each observable is sensitive only to a unique range of accelerated ion energies. For example, when deriving spectral indexes from measured line fluence ratios, the effective ion energies relevant to the $^{16}O/^{20}Ne$ ratio are much lower than those relevant to the neutron capture/^{12}C line ratio. In this section we determine the effective ion energy ranges responsible for the various products of nuclear reactions.

The main factor determining the effective energy range for a nuclear reaction is the cross section, but the shape of the accelerated ion spectrum can be important. Steep spectra can shift the emphasis to lower energies and vice versa. For thin target interactions, only the cross section and spectrum are relevant. As a general rule, only ions with energies where the cross section is significant contribute to thin target interactions. For thick target interactions, however, even ions with high energies where cross sections are often small also contribute, since they can lose energy and then interact where the cross section is significant.

Using our nuclear production computer codes we have calculated the yields of deexcitation lines, escaping neutron spectra and the neutron capture line for monoenergetic accelerated ions. For the deexcitation lines we include all spallation reactions leading to the excited nuclei. We show in Figure 18 monoenergetic ion yields for the 1.634 MeV ^{20}Ne line and the 2.223 MeV neutron capture line. The composition of the accelerated particles is that given in Table 2 and the yields are normalized to one proton at the given energy. Accelerated ions heavier than He contribute to the neutron capture line, but for the deexcitation lines we are only considering accelerated proton and α particle direct reactions producing the narrow lines. For the neutron capture line calculation, we assumed $\lambda = 300$, $\delta = 0.2$, $^3He/H = 3 \times 10^{-5}$, and $\theta_{obs} = 75°$. The effect of the depth distribution of the production and subsequent attenuation of the 2.223 MeV photons has been taken into account. Because of the thick target assumption, we see that ions of several hundred MeV nucleon^{-1} are very effective in producing the Ne line even though the cross section at those energies is small (see Kozlovsky et al. (2002)).

While we do not discuss in detail the production of positrons in this paper, the positron annihilation line is an important additional diagnostic for flare parameters. We also show in Figure 18 positron yields for monoenergetic ions and emphasize that these yields are for *positrons*, not the subsequent annihilation photons. The assumed accelerated $^3He/^4He$ ratio is 1.0. The structure apparent in this curve deserves discussion. The enhancement at high ion energies (> 300 MeV nucleon^{-1}) is due to positrons from the decay of positively charged pions whose production cross sections have very high threshold energies (Murphy et al. 1987). The enhancement at low energies (less than $\sim$5 MeV nucleon^{-1}) is due to positrons from the decay of radioactive nuclei produced by accelerated ^3He reactions which can have

large cross sections at very low energies (Kozlovsky et al. 2004). The yield at intermediate energies is due to positrons from the decay of radioactive nuclei produced by accelerated protons and α particles with heavier elements and their inverse reactions (Kozlovsky et al. 1987).

The differential accelerated ion kinetic energy spectrum gives the number of ions per unit energy at each energy. To determine the effective ion energies for a particular ion spectrum, we weight the monoenergetic yields calculated above with the given spectrum. As an example, we show in Figure 19 the differential yield of the Ne line as a function of accelerated ion energy for power law spectra with indexes of 3 and 5 and accelerated α/proton = 0.5. We show the separate contributions to the line from accelerated protons (dashed curves) and α particles (dotted curves). We see that for a soft spectrum, the α particle contributions dominate due their lower threshold energies, and the most effective ion energies are around a few MeV nucleon^{-1}. For hard spectra, the proton interactions become important and the effective ion energies shift to higher energies due to the higher proton interaction threshold energies. For intermediate spectral indexes, both accelerated particles can be important and the effective ion energy range can be very broad. To quantify the effective ion energy range for producing the line, we use the following definition: we identify the ion energy where the yield is maximum, and then define the effective range to be that within which the yield has fallen to 50% on each side of the maximum. We note that if the effective energy distribution is very broad, the arbitrary value of 50% could be somewhat misleading.

The fluence ratio of the 6.129 MeV ^{16}O and 1.634 MeV ^{20}Ne lines has been frequently used as a measure of the accelerated ion spectral index. Using the 50% definition for the effective accelerated ion energy range as given above, we can now see what ion energies are most relevant to this ratio. We show in Figure 20 the effective accelerated ion energy ranges for producing the 1.634 MeV ^{20}Ne line (white boxes) and the 6.129 MeV ^{16}O line (grey boxes) for several power law spectral indexes and for accelerated α/proton = 0.1 (panel a) and 0.5 (panel b). The horizontal line within each box corresponds to the peak of the distribution. The ratio of these two lines has been used to determine accelerated ion spectral indexes (see §2.4.1). The Figure shows that the effective energy range for producing the ^{16}O line is always shifted to higher energies than for the ^{20}Ne line. This is reflected in Figure 7 where the ^{16}O/^{20}Ne yield ratio curve monotonically decreases with increasing spectral index. The degree of separation of the effective energy ranges for the two lines determines the sensitivity of the ratio to the spectral index (i.e., the slope of the curve in Figure 7). Because the separation for these two lines is not large, the slope of the yield ratio curve in Figure 7 is not very steep.

The range of accelerated ion energies relevant to this line ratio can also be seen in Figure 20. For very hard spectra, the upper range of the effective ion energies can be ∼100 MeV nucleon^{-1}. But for most (softer) spectra it is less than 10 MeV nucleon^{-1}. The lower range is typically a few MeV nucleon^{-1} but for very soft spectra (particularly when α/proton = 0.5) it can be less than 2 MeV nucleon^{-1}. For softer spectra, the line production is dominated by the lower energy reactions of accelerated α particles. As the spectrum hardens, the higher energy accelerated proton reactions begin to contribute and the effective ion energy range shifts to higher energies and becomes broader as interactions of both α particles and protons contribute.

The fluence ratio of the 4.438 MeV ^{12}C and 2.223 MeV neutorn capture lines has also been frequently used as a measure of the accelerated ion spectral index. We show in Figure 21 the effective accelerated ion energy ranges for the 4.44 MeV ^{12}C line (white boxes) and the 2.223 MeV neutron capture line (grey boxes) for several power law spectral indexes and for accelerated α/proton = 0.1 (panel a) and 0.5 (panel b). For the neutron capture line, λ = 300, δ = 0.2, ^{3}He/H = 3×10^{-5}, and $\theta_{\rm obs} = 75°$. The ranges of effective ion energy ranges for the 4.44 MeV line are similar to those for the 6.129 MeV ^{16}O line shown in Figure 20 since the production cross sections for the two lines are similar. For hard spectra ($s < 4$), the effective ion energies for the neutron capture line extend to very high energies, up to ∼ 100 MeV nucleon^{-1}, and are generally much higher than those producing the ^{12}C line. However, for soft spectra ($s > 4$), the effective ion energies for the neutron capture line can be very low (< 7 MeV nucleon^{-1}) due to neutron production by the exothermic (α, n) reactions on heavy elements. For such soft spectra the effective ion energies for the neutron capture line are even less than those for the ^{12}C line. This behavior of the separation of the effective ion energies for the two lines is reflected in Figure 7 where the slope of the yield ratio curve is very steep for hard spectra but then flattens and even begins to rise for very soft spectra. The very broad effective ion energy distribution for the neutron capture line at intermediate spectral indexes reflects the nearly-equal contribution to the line from both low-energy and high-energy neutron production reactions. We find that there is essentially no dependence of the neutron capture line effective ion energy ranges on λ and δ. As the flare location moves from disk center to limb, the effective energies shift to slightly lower energies since the neutrons from higher energy reactions are generally produced deeper and are subsequently more attenuated by Compton scattering.

When a spectral index is derived using the ratio of these two lines, the relevant ion energies cover a broad range of energies. For hard spectra, the relevant ion energy range extends from a few MeV nucleon^{-1} up to and greater than 100 MeV nucleon^{-1}. For soft spectra ($s > 4$), the relevant ion energy range is much narrower, from less than 1 to a few MeV nucleon^{-1}. For very soft spectra, the lack of separation of the effective ion energies

producing the two lines reduces the sensitivity of the ratio to the spectral index, as seen in Figure 7.

Determining the effective accelerated ion energies for production of the neutrons escaping from the Sun and arriving at Earth is more complicated than for a γ-ray line since there is no simple *yield*. Rather, there is an escaping neutron *spectrum* which results in a time history of neutrons of varying energies arriving at Earth. We show in Figure 22 the effective accelerated ion energies for neutrons arriving at Earth before (grey boxes) and after (white boxes) a time $t_{\rm arr} = 850$ s after the release of the accelerated ions into the magnetic loop at the Sun. The effective energies are shown for several power law spectral indexes and $\lambda = 300$, $\delta = 0.2$, ^{3}He/H $= 3 \times 10^{-5}$, and $\theta_{\rm obs} = 75^\circ$ and for accelerated α/proton = 0.1 (panel a) and 0.5 (panel b). The choice of $t_{\rm arr} = 850$ s is motivated by the analysis of the June 4 flare presented in §3.1. The figure shows that the effective ion energies producing neutrons that arrive at the Earth before 850 s are very high, always greater than 100 MeV nucleon^{-1}. Neutrons arriving after 850 s are produced by accelerated ions of lower energies.

In Figure 23 we show the effective accelerated ion energies for the production of positrons for accelerated ^{3}He/^{4}He = 0 (white boxes) and 1 (grey boxes) and for accelerated α/proton = 0.1 (panel a) and 0.5 (panel b). The figure shows that for very hard spectra, the effective ion energies can be extend to more than a GeV nucleon^{-1} because the positrons result mainly from very high-energy reactions producing charged pions. With α/proton = 0.1, the production is primarily from accelerated proton reactions and the lower energy of the effective energy range is several hundred MeV nucleon^{-1}. When α/proton is 0.5, lower energy accelerated α particle and heavy element interactions producing radioactive nuclei also contribute, extending the effective energy range to lower energies. The very low energy reactions of accelerated ^{3}He do not contribute significantly. For softer spectra, the contribution from ^{3}He reactions can lower the lower range of the effective energies to less than 1 MeV nucleon^{-1}, the lowest ion energies for any of the observables considered here. The upper range is from a few MeV nucleon^{-1} to $\sim$ 15 MeV nucleon^{-1} depending on the ^{3}He abundance.

Because the measured ratio of the 0.511 MeV positron annihilation line fluence to the fluence of a deexcitation line, such as the 4.44 MeV ^{12}C line, has also been used to derive spectral indexes, for comparison we also show in Figure 23 the effective accelerated ion energy ranges for the 4.44 MeV line from Figure 21. We see that when spectral indexes are determined from this ratio, the effective ion energies are from less than an MeV nucleon^{-1} to a few MeV nucleon^{-1} for very soft spectra and from many MeV nucleon^{-1} to over a GeV nucleon^{-1} for very hard spectra. We again caution, however, that the effective energies shown in this figure are for the production of *positrons*. The escaping 0.511 MeV annihilation

photons can be significantly attenuated if the positrons are produced deep in the solar atmosphere. Pion production can be very deep since the high energy ions responsible have very long ranges. As a result, even for very hard spectra, the annihilation photons that do escape can be mainly from decay of radioactive nuclei rather than pions. Such nuclei are produced by ions with energies that are much lower than those indicated in the figure. High-energy (>10 MeV) continuum emission from neutral and charged pion decay is only produced by accelerated ions (protons and α particles) with energies greater than $\sim$200 MeV nucleon^{-1}.

3. ANALYSIS PROCEDURE FOR HIGH-ENERGY FLARE DATA

In the previous sections we have explored how the measurable quantities of high-energy flare data depend on the acceleration and physical parameters of the transport and interaction model. The measurable quantities that we will consider in the flare analysis presented here are: deexcitation line time-dependent fluxes, time-integrated fluences and fluence ratios; deexcitation line shapes and centroid shifts; time-dependent electron bremsstrahlung flux; neutron-capture line time-dependent flux and fluence; escaping neutron time-dependent flux at earth; and images of the active region at various wavelengths. We list these quantities in Table 4 along with their most important dependences on the acceleration and physical parameters (see Table 1). Most of these parameters have been defined earlier. The heliocentric angle of the flare, $\theta_{\rm obs}$, is provided by NOAA/SEC determinations based on optical images. For flares located near the solar limb, these determinations can be uncertain. In addition, the flare optical location and the site of the nuclear reactions may not be the same.

We see that each of the measurable quantities can depend on several parameters. Restricting an analysis to one or a small subset of the measurable quantities can result in parameter estimates with constraints that may be inconsistent with estimates derived from analysis of other measurable quantities. And, if the effect of all of the relevant parameters is properly taken into account, the uncertainties will be necessarily large; if only a subset of the parameters is considered, the uncertainties will be underestimated. A useful and reliable analysis must utilize as many measurable quantities as possible to determine as many parameters as possible. But because of the many inter-dependences on the parameters, this can be quite challenging and making progress in constraining the parameters may require additional assumptions. In the following we analyze the high-energy flare data available for the 1991 June 4 flare within the framework of the loop transport model. We will attempt to establish well-constrained values for all of the parameters and show that the loop model can account for the wide variety of observables available for this flare with reasonable values for

them. The guiding principle of the analysis will be to first analyze those measurable quantities that depend only on one or two parameters and then, using those parameter estimates, proceed to other observables that have more complicated dependences. The procedure is designed to take best advantage of the parameter dependences and may be useful in analysis of other flares with a similar range of measurable quantities.

3.1. Analysis of the *CGRO*/OSSE 1991 June 4 Flare Data

In June of 1991, active region 6659 rotated onto the solar disk and produced some of the largest flares ever recorded. It first appeared at the east limb on June 1 and produced an X12+ flare. The peak of this flare was missed by the *CGRO* instruments because the satellite was in the South Atlantic Anomaly (SAA). As there was a high probability for subsequent intense flares, a solar Target of Opportunity was declared for the Oriented Scintillation Spectrometer Experiment (OSSE) on *CGRO* which is sensitive to γ rays from 0.04 to >150 MeV and neutrons >10 MeV. On June 4, AR 6659 produced a second X12+ flare while OSSE was viewing the Sun. The flare was one of the most intense nuclear γ-ray line flares observed to date; most instruments, from the soft X-ray to the γ-ray bands, saturated at its peak. Energetic particles from the flare were observed in interplanetary space by the EPAC experiment on Ulysses (McDonald et al. 1995), GOES and IMP-8 (Tylka et al. 1996). The NOAA *Solar-Geophysical Data Comprehensive Report* gives the Hα flare location as N30E70. This location corresponds to a heliocentric angle of $\sim$74.5° at the time of the flare. The flare was also observed at 17, 35 and 80 GHz by radiometers at the Nobeyama Radio Observatory in Japan (Ramaty et al 1994).

During the OSSE observations, the Sun was kept within 0.8° of the axes of two of the detectors while the remaining two detectors "chopped"; i.e., alternately pointed at and 4.5° off the Sun at 131.1-s intervals. Full spectra were accumulated from each detector at 8-s intervals. Excellent measurements of both γ rays and neutrons were obtained during the rise, peak and decay of the event. The decay was interrupted by satellite night but observations were resumed at daylight of the next orbit and additional observations were obtained. Nuclear deexcitation line and neutron-capture line emission were detected (Murphy et al. 1997) throughout the first orbit (>1000 s) and continued into the second. Continuum γ-ray emission at >16 MeV was detected during the peak of the flare. The high-energy emission decayed much more rapidly than the line emission, falling to below detectability within 250 s after the γ-ray peak. The spectrum of the high-energy emission showed no evidence for a pion-decay feature (Del Signore 1995), implying that this emission was predominantly electron bremsstrahlung. A strong neutron signal was detected following the high-energy

γ-ray emission and continued until the Sun was occulted by the Earth. The June 4 flare neutron data were discussed in the analysis (Murphy et al. 1999) of the 1991 June 1 flare in which neutron emission was also detected by OSSE.

The June 4 flare was so intense that it produced severe saturation effects in the three detectors directly viewing the Sun. Data from the single off-pointed detector were largely unaffected because the hard X-ray photons were absorbed in the shield and collimator. During the peak, only data from this detector are used, although the statistical significance is reduced and the absorption and scattering prevents measurement of solar photons less than $\sim$1 MeV.

We begin the analysis with the parameter that is most easily established, the size of the flare loop, which can be simply determined from images of the flare. Ideally, images of γ-ray emission loop footpoints, such as obtained by *RHESSI* from the 2002 October 28 flare, would be used. Such images are not available for the June 4 flare, but some constraints can be obtained from images at other wavelengths. For example, white-light images of flares can be used to identify potential loop footpoints. Sakurai et al. (1992) provide white-light images of active region 6659 during the June 4 flare. The third panel of their Figure 2b shows the white-light patches at 3:40:34 UT, very near the peak of the June 4 flare γ-ray line emission at 3:41:07 UT. If these patches are taken to be footpoints where ions are interacting, then the possible corresponding loop lengths range from 11,500 km to 65,000 km (assuming a semicircular loop) depending on which pair is assumed to be associated with the loop producing the γ rays. In the analysis following we will consider three possible loop lengths: 11,500, 34,500 and 65,000 km.

The most direct measure of the accelerated α/proton ratio is the measured fluence ratio of the α-α line complex and a narrow line such as the 4.438 MeV line of ^{12}C or, to improve statistical significance, the sum of high-FIP lines. However, the fluence ratio also depends on the accelerated ion spectral index. The spectral index can be determined from the measured fluence ratio of the 6.129 MeV ^{16}O and 1.634 MeV ^{20}Ne lines, but this fluence ratio also depends on the accelerated α/proton ratio. Here, we will simultaneously determine the α/proton ratio and the spectral index by calculating values of the two fluence ratios for a range of assumed α/proton ratios and spectral indexes and comparing them with the measured fluence ratios. The June 4 flare measured fluence ratio of the $\alpha - \alpha$ line complex and the sum of high-FIP narrow lines obtained with sun-pointed detectors late in the flare was 0.66 $\pm$ 0.04 (Murphy et al. 1997). The measured fluence ratio of the 6.129 MeV ^{16}O and 1.634 MeV ^{20}Ne lines integrated over the entire flare 0.66 $\pm$ 0.07 (see erratum to Murphy et al. (1997)). We show in Figure 24 the 99% confidence contours from each of these comparisons, with the grey area representing the overlapping 99% confidence region.

We see that the accelerated α/proton ratio was at least 0.4 and the spectral index is 3.9 $\pm$ 0.2. Murphy et al. (1997) also found that the α/proton ratio was closer to 0.5 than 0.1. While consistent within the uncertainties with the index (4.4 $\pm$ 0.3) determined by Murphy et al. (1997), the index derived here is harder due to the updated cross sections used here. We see from Figure 20 that the ion energies relevant to a spectral index determined from the O/Ne line ratio is from $\sim$1 to several MeV nucleon^{-1}.

The parameters determined thus far do not depend on the atmospheric model $n(h)$. Because the atmospheric model cannot be characterized by a simple parametrization, we will carry out the analysis procedure first assuming the Avrett atmospheric model representing a sunspot, and then repeat the procedure assuming the *RHESSI*/Avrett model representing possible flare conditions and compare the results.

3.1.1. Analysis Assuming the Avrett Sunspot Atmospheric Model

The measurable quantity that depends on the fewest yet-undetermined parameters is the deexcitation line centroid shift. As discussed in §2.4.2, this shift depends primarily on the interacting angular distribution which in turn depends on the magnetic convergence (δ) and level of PAS (λ). The energy of the photon emitted by deexcitation from the first excited state of ^{12}C in its rest frame is 4.438 MeV. The line centroid during the flare was measured to be 4.442 $\pm$ 0.005 MeV by fitting a Gaussian profile to the spectral data. We compare this measured centroid with predicted centroids calculated for angular distributions arising from various combinations of λ and δ, accelerated α/proton = 0.5, and the range of spectral index determined above. The predicted centroids were obtained by fitting a Gaussian profile to calculated line profiles (e.g., see Figure 9). For each combination of δ and λ (and s), we calculate $\Delta\sigma$; i.e., how many 1-σ uncertainties the measured line centroid differs from the calculated centroid. In Figure 25, we show contours of $\Delta\sigma$ = 2.3, 4.6, and 9.2 corresponding to 68, 90 and 99% confidence (for 2 parameters of interest) that the calculated shift is not consistent with the measured shift. While simultaneously-low values of δ and λ can be rejected (corresponding to downward-directed angular distributions), there is still a wide range of δ-λ combinations that is allowed. Because of the location of this flare (74.5° heliocentric angle), the shift of the line centroid from a loop perpindicular to the solar surface, as assumed here, is not sensitive to the interacting particle angular distribution (see §2.4.2) and so does not provide strong constraints on δ and λ.

A different and more restrictive constraint on δ and λ can be obtained by considering the time history of the prompt deexcitation lines. Within our loop transport model, a necessary component of this analysis is the time history of the release of the accelerated ions at the top

of loop, $a_{\rm ion}(t)$, which is not known. We will assume two cases: (1) where the ion release is instantaneous and the time history of the prompt line emission is due entirely to transport, and (2) where the ion release is extended in time. For the instantaneous release case we will assume two possible instantaneous release times: (1) at the beginning of the >300 keV electron bremsstrahlung as measured by BATSE (13250 s UT), and (2) at the beginning of the prompt deexcitation line emission (13260 s UT). For the extended release case, we will assume that $a_{\rm ion}(t)$ is identical to the relativistic electron acceleration release time, $a_{\rm e}(t)$ and further assume that $a_{\rm e}(t)$ is identical to the time history of the relativistic electron bremsstrahlung flux, $\phi_{\rm brem}(t)$. Because relativistic electron transport should be very fast, the bremsstrahlung emission time history should be very nearly identical to $a_{\rm e}(t)$. For each release scenario we calculate predicted prompt deexcitation line time histories for various combinations of δ and λ and compare them with the time history of the OSSE measured summed high-FIP narrow γ-ray lines for each of the three loop lengths.

For the instantaneous release-time scenarios, we found that the best fit was achieved for a loop length of 34,500 km. Loop lengths of 11,500 and 65,000 km did not provide acceptable fits for either of the release times. For the 34,500 km loop length, only the release time at 13260 s UT provided an acceptable fit. The 13250 s UT release time was too early so that even with δ-λ combinations providing maximum delay of the emission, transport could not provide an adequate fit to the time history. We show in Figure 26 the OSSE summed prompt high-FIP deexcitation line flux time history (data points) along with time histories calculated for $\delta = 0.20$ and several values for PAS: $\lambda = 20$ (saturated), 300, 700, 5000 and none($\lambda \rightarrow \infty$). We show in Figure 27 the 68, 90 and 99% δ-λ confidence contours (thick curves) obtained from this fit. The figure shows that as the level of magnetic convergence increases (resulting in a more extended time history), the level of PAS must increase (shortening the time history). Regions of low convergence-high PAS and high convergence-low PAS are not acceptable. We also show in Figure 27 the contours from the line shift analysis (thin curves, see Figure 25), with the gray region representing the overlapping 99% confidence region. We will assume a range of δ-λ combinations drawn from this acceptable region for the remaining analyses.

We next consider the case using the bremsstrahlung time history. We show in Figure 28 the time history of the summed prompt high-FIP narrow γ-ray lines, $\phi_{\rm highFIP}(t)$ (the histogram), and the time history of the >300 keV bremsstrahlung emission, $\phi_{\rm brem}(t)$, measured by BATSE where the upper curve is without background subtraction and the lower curve was obtained with a simple, linear background subtraction. For comparison, the γ-ray and bremsstrahlung emissions have been normalized to the same flux at the peak of the emission. Near the peak, the two emissions have a similar time history. At later times, while the two time histories are similar, the line emission is stronger than the bremsstrahlung, as noted

by Murphy et al. (1997). This may suggest that, while later in the flare their acceleration processes may differ, at the peak of the flare both the ions and electrons are similarly accelerated. We therefore assume that the electron bremsstrahlung time history also represents the ion acceleration release time history during the first peak and we concentrate this part of the analysis on this peak only, from 13250 to 13335 s UT.

For this case we find that all loop lengths considered could provide adequate fits. However, the confidence regions for the 34,500 and 65,000 km loop lengths did not allow values of δ greater than about 0.10. Such small values of δ do not provide the increase of magnetic field from the corona to the photosphere expected to exist in flare loops so we reject these longer loop lengths as not physically acceptable. Only the 11,500 km loop length provides a region of acceptable δ and γ values. We show in Figure 29 the 68, 90 and 99% δ-λ confidence contours (thick curves) obtained from this fit. We also show the contours from the line shift analysis (thin curves, see Figure 25), with the gray region representing the overlapping 99% confidence region. We will assume a range of δ-γ combinations from this acceptable region for the remaining analyses.

We next analyze the neutron-capture line, considering both the shape of its time history and its absolute fluence relative to the other emissions. From Table 4 all of the parameters that this line depends upon have now been constrained by our procedure except the ambient ^{3}He/H ratio. We calculate predicted neutron capture-line time histories by convolving the time histories calculated for instantaneous release (see §2.6) with the ion acceleration release time history, $a_{\rm ion}(t)$. Again, $a_{\rm ion}(t)$ is not known but we cannot use the electron bremsstrahlung time history as we have in the previous analysis of the deexcitation line time history at the peak of emission because we require the time history throughout the entire flare, and we know that at later times the electrons and ions are not similarly accelerated (see Figure 28). Instead, we will use the measured high-FIP deexcitation line time history, $\phi_{\rm highFIP}(t)$, to represent the acceleration release time history. Deexcitation lines are prompt, and their time history is essentially identical to the nuclear interaction time history. Ion transport times (from release to interaction) are generally much shorter than neutron transport times from production to capture by H (compare Figures 2 and 17). As a result, the capture line time history should not be sensitive to the small time delay between accelerated ion release and the nuclear interaction producing the neutron. For the neutron-capture line analysis, therefore, using the prompt deexcitation line time history to represent the ion release time history is adequate. The absolute flux of the deexcitation lines fixes the normalization of the predicted neutron capture line time history.

We use the neutron production code to calculate expected neutron-capture line time histories at the heliocentric angle of the June 4 flare for a range of ambient ^{3}He/H. We use

a range of spectral indexes drawn from the acceptable range of 3.9 ± 0.2 established from the combined α-α/high FIP line ratio and O/Ne line ratio analyses above and assume the power law extends unbroken to 10 GeV. We use a range of δ-λ combinations drawn from the acceptable confidence regions established from the previous line centroid shift and line time history analyses (see Figures 27 and 29). We compare the calculated time histories with the measured (Murphy et al. 1997) time history, using χ^2 as the measure of goodness of fit. An example of such a fit is shown in Figure 30 where the solid curve is the calculated time history for $s = 4$, saturated PAS, $\delta = 0.35$ and ^{3}He/H $= 1 \times 10^{-5}$. The dotted curves represent the $\pm$1-σ uncertainties for the calculated curve. Unfortunately, the allowed ranges for δ, λ and s we have established previously do not allow a well-determined value for ^{3}He/H. We find that the fits to the neutron-capture line time history could only provide a ^{3}He/H upper limit of 4.5×10^{-5} (3-σ).

To compare our ^{3}He/H upper limit with values obtained with other techniques, we use a determination of photospheric ^{3}He/^{4}He obtained from recent solar wind measurements (Geiss and Gloeckler 1998). Taking into account the effects of separation and fractionation, they derived the present value to be ^{3}He/^{4}He $= (3.8 \pm 0.5) \times 10^{-4}$. This value is consistent with the value that can be derived from the measurement by Mahaffy et al. (1998) of D/H and ^{3}He/^{4}He in the Jovian atmosphere using the the Galileo probe. The Jovian abundances are approximately those of the proto-solar cloud. In the Sun, all of the proto-solar deuterium has been converted to ^{3}He. Taking into account the small additional production of ^{3}He over the solar history and the small decrease of ^{4}He/H due to settling of ^{4}He (Geiss and Gloeckler 1998), we find that this estimate of the present value of ^{3}He/^{4}He is consistent with the above value from the solar wind measurements. To convert to ^{3}He/H, the value of ^{3}He/^{4}He must be multiplied by the ^{4}He/H ratio in the photosphere of the ambient, flaring plasma. We use the value of 0.097 from Grevesse et al. (1996). Because we are dealing with flare plasma where variations of ^{4}He/H have been observed, we adopt an uncertainty of $\pm$0.02 for this ratio which reflects the range of values obtained by a number of investigators (e.g., see summary by Feldman et al. (2005)). This gives ^{3}He/H $= (3.7 \pm 0.9) \times 10^{-5}$ for our best estimate of the photospheric value. Our upper limit of ^{3}He/H $< 4.5 \times 10^{-5}$ derived from the γ-ray measurements is consistent with this value.

We can now use the current best-estimate ^{3}He/H value of $(3.7 \pm 0.9) \times 10^{-5}$ to provide a better constraint on the spectral index s for this flare. Using this range of ^{3}He/H values we vary the spectral index and use δ-λ combinations drawn from the acceptable ranges established above to provide the best fit to the neutron-capture line time history. We find that good fits are achieved with $3.93 < s < 4.05$ ($\pm$1 σ). This allowable range lies within the allowable range of $3.7 < s < 4.1$ obtained from the combined α-α/high FIP ratio and O/Ne ratio analyses and provides our best estimate for the index: $3.93 < s < 4.05$ or 3.99

$\pm$ 0.06 ($\pm 1\ \sigma$).

Because no evidence of a pion-decay emission feature was seen in the OSSE >16 MeV γ-ray spectrum (Del Signore 1995), the high-energy emission (detectable only during the peak of the γ-ray line emission) was attributed to relativistic electron bremsstrahlung. Using the calculations of Murphy & Ramaty (1984) and Murphy et al. (1987) and assuming that the accelerated-ion power-law spectrum continues unbroken to energies >100 MeV with the spectral index range determined above, we estimate the total γ-ray fluence at 100 MeV due to pion-decay during the first interval would be $\sim$0.03 photons MeV^{-1} cm^{-2}. The measured (Del Signore 1995) fluence at 100 MeV was 0.12 photons MeV^{-1} cm^{-2}. We therefore confirm that the bulk of the high-energy emission was electron bremsstrahlung. If the accelerated-ion spectrum were to steepen above 100 MeV, the expected pion-decay fluence would be less (see the neutron analysis below).

Since all of the parameters listed in Table 4 have now been determined, the remaining observables (the neutron arrival time history and absolute fluence) will provide a consistency check on those parameters. In addition, since the neutrons have a different parameter sensitivity than the other measurable quantities, their measurement can instruct how to modify the other parameter estimates and iterate the above procedure to provide better parameter constraints. We use the neutron production code to calculate escaping neutron kinetic-energy spectra for the heliocentric angle of the June 4 flare, $\theta_{\rm obs} = 74.5°$. For the ion acceleration release time history, $a_{\rm ion}(t)$, we again use the prompt deexcitation line time history, $\phi_{\rm highFIP}(t)$. We propagate the escaping neutrons to Earth, taking into account decay of the neutrons, and convolve the arriving neutron spectra with the OSSE neutron response (see Appendix), producing predicted neutron energy-loss count spectra. These spectra are integrated above 23 MeV (OSSE channel 2) and compared with the corresponding measured count rates. The statistical counting rate uncertainties have been increased by adding in quadrature an additional uncertainty of 30% to account for uncertainties in the OSSE neutron response function (see the Appendix).

For all of the δ-λ combinations allowed from the previous analyses (see Figures 27 and 29) and the index range of 3.99 ± 0.06 determined above, we find that the number of neutrons arriving at Earth is over-predicted, with the discrepancy being larger at early times. This can be seen in Figure 31 comparing the measured neutron count rate with a predicted rate (solid curve) calculated for saturated PAS, $\delta = 0.35$ and s at its upper (i.e., steeper spectrum) 1-σ limit of 4.05. The neutron count rate is overpredicted at times less than about 850 s after the peak of the deexcitation line emission. Figure 22 shows that for $s = 4$, neutrons arriving before 850 s are produced by accelerated ions with energies >200 MeV nucleon^{-1}. Reducing their number relative to lower-energy neutrons can be achieved if the accelerated-

particle spectrum steepens with energy, as long as this does not affect the other measurable quantities previously analyzed. This is possible since deexcitation lines and the neutrons responsible for the neutron capture line are produced by accelerated ions with lower energies than the ions producing the neutrons escaping into space and surviving to Earth (see §2.4.4). Such steepening has been observed in SEP spectra from both impulsive and gradual flares (Tylka et al. 2005, 2002; Mason et al. 2002). Here, we will simulate such steepening by introducing a sharp cutoff of the power law spectrum at an energy E_c, realizing that an actual particle spectrum most likely would not cut off suddenly but would steepen gradually with energy. We also show in Figure 31 (dotted curve) the predicted neutron arrival time history calculated for the same spectral index $s = 4.05$ but with a cutoff energy $E_c = 125$ MeV nucleon^{-1}. We have confirmed that this spectrum still predicts a neutron-capture line time history that provides an acceptable fit to the data and that the other calculated measurable quantities are not affected. As discussed in §2.4.4, the other observables are primarily produced by accelerated ions with energies less than 125 MeV nucleon^{-1}.

3.1.2. Analysis Assuming the RHESSI/Avrett Atmospheric Model

Starting with the previously-determined parameters that are independent of the atmospheric model ($s = 3.9 \pm 0.2$, and α/proton > 0.4), we repeat the previous analysis but using the *RHESSI*/Avrett atmospheric model. As for the Avrett analysis, we begin by attempting to constrain δ and λ. As discussed in §2.3.2, the interacting particle angular distribution (and thus the shift of the deexcitation line centroid) is similar for both models of the atmosphere except for very low levels of PAS where somewhat greater red shifts result from the slightly more downward-directed interacting angular distribution. As for the Avrett atmosphere, the line-shift analysis does not provide any significant constraint on δ and λ for this flare location.

We now attempt to constrain δ and λ by considering the prompt deexcitation line time history using the same ion acceleration release time histories assumed in the Avrett analysis. Because the ion interaction time histories for this atmosphere are much shorter than for the Avrett atmosphere (see §2.3.1), we found that the time histories for neither of the instantaneous release times could provide acceptable fits; no combination of δ and λ could produce a time history extended enough to to fit the line time history. If the *RHESSI*/Avrett atmosphere is applicable during this flare, the implication of this analysis is that accelerated-particle release cannot be instantaneous. Using the electron bremsstrahlung time history as the ion acceleration release time history, we again find that all of the loop lengths could provide adequate fits. But, as discussed in §2.3.1 and shown in Figure 2f, the dependence

of the time history on δ and λ is weaker for the *RHESSI*/Avrett atmosphere than for the Avrett atmosphere. This, combined with the relatively poor statistical quality of the OSSE off-pointed data, resulted in no significant constraint on δ and λ.

With no constraints on δ and λ and the ± 0.2 uncertainty on the spectral index, no significant constraint on the photospheric ^{3}He/H ratio can be established using the time history of the neutron capture line. We now fix the ^{3}He/H ratio at the independently determined value of $(3.7 \pm 0.9) \times 10^{-5}$ and reverse the analysis attempting to place constraints on δ and λ. But, except for exclusion of δ-λ combinations where both parameters are very small (corresponding to strongly downward-directed interacting ion angular distributions), only very broad allowable ranges of δ-λ combinations can be established.

For the neutron arrival time history, we find that a good fit of the predicted count rate to the data could not be obtained, regardless of the δ-λ combination assumed. Similar to the result for the Avrett atmosphere, the count rate was over-predicted at early times. We again find that introducing a cut off of the accelerated ion spectrum above $\sim$125 MeV nucleon^{-1} provides a good fit without affecting the other measurable quantities.

4. DISCUSSION

Using recently updated cross sections for deexcitation γ-ray lines (Kozlovsky et al. 2002) and neutron production (Hua et al. 2002), we have calculated a number of measurable quantities associated with narrow γ-ray deexcitation lines, the neutron capture line, and escaping neutron spectra. All of these calculations have been performed within the context of a magnetic loop model that provides a physical basis for the interacting accelerated ion time delays and anisotropic angular distributions that previously have only been assumed. The model includes energy losses due to Coulomb collisions, removal by nuclear reactions, magnetic mirroring in the convergent flux tube, and MHD pitch-angle scattering (PAS) in the corona. The measurable quantities depend on the parameters of the model (see Table 1) which are of two types: *acceleration* and *physical*. Acceleration parameters are associated with the acceleration processes: accelerated particle power law spectral index (s), acceleration release time history ($a_{\rm ion}(t)$), and accelerated particle elemental composition. Physical parameters are associated with the conditions of the magnetic loop within which the accelerated particles transport and interact with the ambient atmosphere: level of PAS (λ), magnetic field convergence (δ), loop length (L), and the atmospheric elemental composition and density and temperature height distributions ($n(h)$ and $T(h)$).

The measurable quantities we considered were: narrow deexcitation line shapes, shifts,

fluences, and time histories; neutron capture line fluence and time history; and escaping neutron fluence and time history. Each of these measurable quantities depends to varying degree on some subset of the acceleration and physical parameters (see Table 4). We explored these dependences in detail, presenting a number of figures expressing the most significant effects for each observable. To present these dependences for every possible combination of physical and acceleration parameters would be impossible. Instead, we carefully chose ranges of parameter values that most effectively convey these often complex interdependences.

We find that deexcitation line yields are not sensitive to physical parameters other than the ambient composition, being most sensitive to the acceleration parameters. The line shapes and shifts, however, are, since the physical parameters affect the angular distribution of the interacting accelerated particles. Physical parameters also affect the delay between accelerated ion release and interaction which affects the line time history. Similarly, total neutron production is also more sensitive to the acceleration parameters. However, the number and spectrum of neutron *escaping* from the Sun along a given direction and the neutron capture line fluence and time history are very sensitive to the physical parameters, again due to the effect of the interacting ion angular distribution. Increased production of neutrons in interactions of accelerated ions moving downward toward the Sun increases the neutron-capture line yield but decreases the yield of escaping neutrons.

Because each of the measurable quantities can depend on some or all of the same acceleration or physical parameters, deriving well-constrained values for those parameters can be difficult. Restricting an analysis to one or a small subset of the measurable quantities can result in parameter estimates with constraints that may be inconsistent with estimates derived from analysis of other measurable quantities and incorrectly estimated uncertainties. Acknowledging that a meaningful analysis must utilize as many measurable quantities as possible, we applied the calculations in an analysis of the γ-ray and neutron observations of the 1991 June 4 solar flare obtained with *CGRO*/OSSE, one of the best-observed high energy flares. The analysis technique applied to this flare provides an algorithm that can be applied to other flares with measurements covering a similar wide range of measurable quantities. The guiding principle of the analysis is to first analyze those measurable quantities that depend only on one or two parameters and then, using those parameter estimates, proceed to other observables that have more complicated dependences. The procedure is designed to take best advantage of the parameter dependences. We showed that the loop model can account for the wide variety of observables available for this flare with reasonable values for the parameters.

We began the analysis by obtaining an upper limit of 65,000 km for the loop size using white light images of the June 4 flare showing loop footpoints, assuming that such loops are

the same as those associated with the nuclear interactions. The accelerated α/proton ratio and ion spectral index were next determined simultaneously using the measured fluence ratios of (1) the α-α line complex and the summed high-FIP narrow deexcitation lines and (2) the 6.129 MeV ^{16}O and 1.634 MeV ^{20}Ne lines. The α/proton ratio was found to be at least 0.4 and the the spectral index was determined to be 3.9 ± 0.2. Because the remaining measurable quantities depend to some extent on the density-height distribution of the atmosphere, the analysis continued along two parallel paths, each assuming one of two possible atmospheric models: the Avrett (1981) model representing a sunspot and a hybrid model combining the distribution above 1000 km derived from *RHESSI* X-ray measurements (Aschwanden et al. 2003) with the Avrett model below, and referred to as the *RHESSI*/Avrett model.

For the Avrett model, constraints on PAS (λ) and magnetic convergence (δ) were first attempted using the measured Doppler shift of the 4.438 MeV ^{12}C narrow deexcitation line. But at the location of the June 4 flare (74.5° heliocentric angle), the dependence of the shift on the interacting ion angular distribution is weak and significant constraints could not be obtained, other than rejecting combinations of δ and λ whose values were simultaneously very low. Such combinations produce the most red-shift of the line. Better constraints on δ and λ were obtained by considering the time history of the deexcitation lines. Several potential time histories for the accelerated ion release time history were assumed and the resulting line time histories were calculated for a wide range of combinations of δ and λ. The calculated time histories were compared with the measured time history and χ^2 was used to establish the quality of fit. Combining constraints from this analysis with the weaker constraints obtained from the line shift analysis provided usable constraints on δ and λ. We found that very low values for both δ and λ (corresponding to strongly downward-directed interacting ion angular distributions) and very high values for both (corresponding to very broad angular distributions) could be rejected. The band of δ-λ combinations providing acceptable fits to both the line shift and time profile corresponded to mildly downward-directed distributions.

We next considered the neutron-capture line. The only remaining parameter affecting this line for which constraints had not been determined was photospheric ^{3}He/H. Neutron-capture line time histories calculated with varying values of ^{3}He/H and with the other parameters drawn from the acceptable ranges previously determined were compared with the measured time history. Acceptable fits to the data were achieved, but the combined effect of the allowed ranges for the various parameters resulted in only an upper limit for ^{3}He/H of 4.5×10^{-5} (3-σ), consistent with a recent estimate of the photospheric ^{3}He/H of $(3.7 \pm 0.9) \times 10^{-5}$. We then used this recent ^{3}He/H estimate to reverse the analysis and place a tighter constraint on the accelerated ion power law spectral index of 3.99 ± 0.06.

The final step of the analysis was to compare arriving neutron count rates calculated for

the allowed ranges of parameters determined from the previous analysis with neutron count rates measured with OSSE. We found that the rates were over-predicted for much of the duration of the event, with the largest excesses occurring early. Noting that early-arriving neutrons are generally the highest-energy neutrons, we calculated an arriving neutron count rate for a power law spectrum having the same spectral index but with a cutoff above an energy of 125 MeV nucleon^{-1} which reduces the relative number of high-energy neutrons. We found that an excellent fit to the measured count rate was achieved. The introduction of the cutoff energy did not significantly affect any of the other observables since they are produced predominantly by accelerated ions with energies below 125 MeV nucleon^{-1}.

Starting with the previously-determined parameters that are independent of the atmospheric model ($s = 3.9 \pm 0.2$, and α/proton > 0.4), we repeated the above analysis but using the *RHESSI*/Avrett atmospheric model. However, because of the reduced sensitivity of the interaction time history at times less than a few seconds to the interacting ion angular distribution (see §2.3.1), the prompt deexcitation line time history analysis provided no useful constraints on δ and λ. We then attempted to use the neutron capture time history measurement (fixing the photospheric ^{3}He/H ratio at an independently-determined value) to constrain δ and λ but could only exclude δ-λ combinations where both parameters are very small (corresponding to strongly downward-directed interacting ion angular distributions). For all acceptable δ-λ combinations, we again found that achieving a good fit to the neutron arrival time history required that the accelerated ion spectrum must cutoff above ∼125 MeV nucleon^{-1}.

We have shown that the measurable quantities associated with high-energy solar flares can depend in complex ways on the parameters of the transport and interaction model. Deriving self-consistent values for these parameters with reliable uncertainties can be difficult. Success requires measurements that cover a wide range of the observables and an analysis procedure that takes best advantage of their different parameter dependences. We applied such an procedure in an analysis of the high-energy data available for the well-measured 1991 June 4 flare. Even though this flare is one of the best measured high energy flares, not all of the parameters could be well constrained. Two factors contributed to this: (1) the flare occurred near the solar limb so that any line shift due to anisotropic ion angular distributions is minimal and (2) because of the intensity of this flare, only data from one off-pointed detector could be used at the peak of emission which dramatically reduced the statistical significance of the time history data. The procedure can be applied to other flares having a similar range of measurable quantities. The successful self-consistent prediction of observables has been achieved within the framework of our loop transport and interaction model with reasonable values for the associated physical and acceleration parameters.

This work was supported by NASA DPR W19,977 and the Office of Naval Research. B. Kozlovsky thanks J. Kurfess for his hospitality at the Naval Research Laboratory. B. Kozlovsky also acknowledges the Israeli Science Foundation for support.

A. OSSE RESPONSE TO NEUTRONS

For solar neutron measurements, detectors such as OSSE are non-diagonal and so do not provide a good measurement of the neutron energy. They do provide a good measurement of the arrival time history of the neutrons. In order to compare calculations of arriving neutrons with the OSSE measurements, the calculated time-dependent neutron spectra arriving at Earth are convolved with the OSSE neutron response to produce predicted neutron count spectra. These count spectra are then integrated over energy to produce a predicted neutron arrival count rate.

The OSSE instrument and its γ-ray calibration is described by Johnson et al. (1993). Here we describe the neutron calibration. OSSE consists of four independently-oriented NaI/CsI phoswich scintillation detectors, each surrounded by an anti-coincidence CsI shield and mounted in an independent elevation-angle gimbal which allows "scanning" through 192° of rotation. OSSE can detect both high-energy γ-rays and neutrons and the two emissions are distinguished by their different pulse shapes in NaI (Share et al. 1978). The identified energy-loss events are separately accumulated into 16 channels up to about 150 MeV for γ rays and 220 MeV for neutrons. The separation is not perfect with the result that a fraction of neutron events are incorrectly identified as γ rays and vice versa. Furthermore, the separation becomes ineffective for neutron energies above $\sim$100 MeV (channel 9).

Energy-loss spectra due to all detected neutrons and to all detected γ rays can be recovered from the separated spectra by using the separation constants (i.e., the energy-dependent fractions of neutron events that are identified as neutrons and as γ rays, and analogously for the γ ray events) developed by Del Signore (1995). These constants were derived for 23–100 MeV neutron energy losses (channels 3–8) by assuming that the >16 MeV emission at the peak of the 1991 June 6 flare (which did not produce neutrons) was purely γ rays, while the emission near the end of the 1991 June 4 event (after all evidence for γ-ray emission has subsided) was purely neutrons. We do not consider neutron energy losses <23 MeV (channels 1 and 2) since at these energies the neutron response is falling rapidly and the count rates are dominated by the lower-energy γ rays arriving simultaneously in the June 4 flare. Above 100 MeV (channel 9), where the total neutron and γ-ray spectra are not recoverable from the separated spectra, we find for the June 4 flare that whether these events are assumed to be all neutrons or all γ rays, the resulting total neutron count rate is

affected only early in the event (when such high-energy neutrons are arriving) and then only insignificantly. We use the separation constants determined at 100 MeV for all >100 MeV energy losses.

A prototype OSSE detector was exposed to neutrons at the Indiana Cyclotron (Jenkins et al. 1992) and an instrument model, consisting of energy-deposited spectra for several incident neutron energies, was developed (T. Jenkins, private communication). When these energy-loss spectra are integrated, the resulting total OSSE neutron response showed a strong turnover at neutron energies above 80 MeV. While a turnover is expected (due to self-veto of high-energy neutrons depositing energy in both detectors and shields), it is not expected to be so severe and the turnover onset energy should be above ∼100 MeV, as derived by Cooper, et al. (1985) for the similar *SMM*/GRS NaI/CsI detectors. In addition, the total OSSE neutron effective area at these energies appears to have been underestimated since it is less than that of the smaller *SMM*/GRS NaI/CsI detectors. To correct the response, we used the NaI neutron response measurements (20 MeV threshold) of Stanlislaus et al. (2001) to renormalize each neutron energy-loss spectrum, maintaining their relative energy dependences as derived by Jenkins. Above the neutron energy of 150 MeV, we introduced a roll-off of the Stanislaus effective areas (which continue to rise with neutron energy), using a neutron-energy dependence similar to that of the *SMM*/GRS given by Cooper, et al. (1985). The change in the neutron count rate predicted by this modified response compared to the count rate predicted by the original response established by Jenkins is small since neutrons >100 MeV do not contribute significantly to the total detected count rate and is within the estimated 30% overall uncertainty of the neutron response that we have included in the June 4 analysis.

REFERENCES

Aschwanden, M. J., Wills, M. J., Hudson, H., Kosugi, T., & Schwartz, R. A. 1996, ApJ, 468, 398

Aschwanden, M. J., Brown, J. C., & Kontar, E. P. 2003, in The Reuven Ramaty High-Energy Solar Spectroscopic Imager (RHESSI) – Mission Description and Early Results, ed. R. P. Lin, B. R. Dennis & A. O. Benz (Kluwer:Dordrecht), 383

Avrett, C. W. 1981, in The Physics of Sunspots, ed. L. E. Cram & J. H. Thomas (Sacramento Peak Observatory:AURA), p. 235

Drake, J. J., & Testa, P. 2005, Nature, 436, 525

Dyer, P., Bodansky, D., Seamster, A. G., Norman, E. B., & Maxson, D. R. 1981, Phys. Rev., C23, 1865

Dyer, P., Bodansky, D., Leach, D. D., Norman, E. B., & Seamster, A. G. 1985, Phys. Rev., C32, 1873

Chupp, E. L., Forrest, D. J., Share, G. H., Kanbach,G., Debrunner, H. & Flueckiger 1983, 18th Internat. Cosmic-Ray Conf. (Bangalore), Late Papers, 334

Cooper, J. F., Reppin, C., Forrest, D. J., Chupp, Share, G. H., & Kinzer, R., L. 1985, 19th Internat. Cosmic-Ray Conf. (La Jolla), 5, 474

Crannell, C. J., Crannell, H., & Ramaty, R. 1979, ApJ, 229, 762

DelSignore, K. W. 1995, Ph.D. thesis, Case Western Reserve University

Dunphy, P. P., Chupp, E. L., Bertsch, D. L., Schneid, E. J., Gottesman, S. R., & Kanbach, G. 1999, Sol. Phys., 187, 45

Evenson, P., Meyer, P., & Pyle, K. R. 1983, ApJ, 274, 875

Ewell, M. W. Jr., Zirin, H., Jensen, J. B., & Bastian, T. S. 1993, ApJ, 403, 426

Feldman, U., Landi, E. & Laming, J. M. 2005, ApJ, 619, 1142

Forrest, D. J. 1983, in Positron-Electron Pairs in Astrophysics, ed. M. L. Burns, A. K. Harding & R. Ramaty (New York:Am. Inst. Phys.), 101, 3

Geiss, J. 1984, Sp. Sci. Rev., 33, 201

Geiss, J., & Gloeckler, G. 1998, Sp. Sci. Rev., 84, 239

Grevesse, N., Noels, A., & Sauval, A. J. 1996, in Cosmic Abundances, ed. S. S. Holt & G. Sonneborn, Astron. Soc. Pac. Conf. Ser., 99, 117

Hurford, G. J., Schwartz, R. A., Krucker, S., Lin, R. P., Smith, D. M., & Vilmer, N. 2003, ApJ, 595, L77

Hua, X.-M., & Lingenfelter, R. E. 1987a, Solar Physics, 107, 351

Hua, X.-M., & Lingenfelter, R. E. 1987b, ApJ, 323, 779

Hua, X.-M., & Lingenfelter, R. E. 1987c, ApJ, 319, 555

Hua, X.-M., R. Ramaty & Lingenfelter, R. E. 1989, ApJ, 341, 516

Hua, X.-M., Kozlovsky, B., Lingenfelter, R. E., Ramaty, R. & Stupp, A. 2002, ApJS, 140, 563

Jenkins, T. L., Frye, G. M., Stansfield, S., Kinzer, R. L., Jensen, C., Kurfess, J. D., Johnson, W. N., Strickman, M. S., Byrd, R., and Foster, C. 1991, 22nd Int. Cosmic Ray Conf. (Dublin), 3, 760

Johnson, W. N., Kinzer, R. L., Kurfess, J. D., Strickman, S M., Purcell, W. R., Grabelsky, D. A., Ulmer, M. P., Hillas, D. A., Jung, G. V., & Cameron, R. A. 1993, ApJS, 86, 693

Kiener, J., de Sereville, N., & Tatischeff, V. 2001, Phys,. Rev. C, 64, 025803

Kozlovsky, B., Lingenfelter, R. E., & Ramaty, R. 1987, ApJ, 316, 801

Kozlovsky, B., Murphy, R. J., & Ramaty, R. 2002, ApJS, 141, 523

Kozlovsky, B., Murphy, R. J., & Share, G. H. 2004, ApJ, 604, 892

Kuzhevskij, B. M., Gan, W.-Q., & Miroshnichenko, L. I. 2005a, Chin. J. Astron. Astrophys., Vol. 5, No. 3, 295

Kuzhevskij, B. M., Miroshnichenko, L. I., & Troitskaia, E. V. 2005b, Astronomy Reports, Vol. 49, No. 7, p. 567

Lingenfelter, R. E. & Ramaty, R. 1967, in High-Energy Nuclear Reactions in Astrophysics, ed. B. S. P. Shen, (N.Y.:Benjamin, Inc.), p. 99

Lingenfelter, R. E., Flamm, E. J., Canfield, E. H., & Kellman, S. 1965a, J. Geophys. Res., 70, 4077

Lingenfelter, R. E., Flamm, E. J., Canfield, E. H., & Kellman, S. 1965b, J. Geophys. Res., 70, 4087

Mahaffy, P. R., Donahou, T. M., Atreya, S. K., Owen, T. C., & Nieman, H. B. 1998, Sp. Sci. Rev., 84, 251

Mandzhavidze, N., Ramaty, R., Bertsch, D. L., & Schneid, E. J. 1996, in High Energy Solar Physics, ed. R. Ramaty, N. Mandzhavidze, & X.-M. Hua (New York:Am. Inst. Phys.), 374, 225

Mandzhavidze, N., Ramaty, R., & Kozlovsky, B. ApJ, 518, 918

Mason, G. M., Wiedenbeck, M. E., Miller, J. A., Mazur, J. E., Christian, E. R., Cohen, C. M. S., Cummings, A. C., Dwyer, J. R., Gold, R. E., Krimigis, S. M., Leske, R. A., Mewaldt, R. A., Slocum, P. L., Stone, E. C., & von Rosenvinge, T. T. 2002, ApJ, 574, 1039

McDonald, F. B., Keppler, E., & Reuss, M. K. 1995, Sp. Sci. Rev., 72, 359

Miller, J. A., Cargill., P. J., Emslie, A. G., Holman, G. D., Dennis, B. R., LaRosa, T. N., Winglee, R. M., Benka, S. G., & Tsuneta, S. 1997, J. Geophys. Res., 102, No. A7, 14631

Murphy, R. J. & Ramaty, R. 1984, COSPAR, Vol. 7, No. 7, 127

Murphy, R. J., Dermer, C. D., & Ramaty, R. 1987, ApJS, 63, 721

Murphy, R. J., Hua, X.-M., Ramaty, R., & Kozlovsky, B. 1990, ApJ, 341, 516

Murphy, R. J., Ramaty, R., Kozlovsky, B., & Reames, D. V. 1991, ApJ, 437, 793

Murphy, R. J., Share, G. H., Grove, J. E., Johnson, W. N., Kinzer, R. L., Kurfess, J. D., Strickman, M. S., & Jung, G. V. 1997, ApJ, 490, 883

Murphy, R. J., Share, DelSignore, K. W., and Hua, X.-M., & Jung, G. V. 1999, ApJ, 510, 1011

Murphy, R. J., & Share, G. H. 2000, The Fifth Compton Symposium, Portsmouth, p. 559

Murphy, R. J., Share, G. H., Skibo, J. G., & Kozlovsky, B. 2005, ApJS, 161, 495

Ramaty, R., Kozlovsky, B. & Lingenfelter, R. E. 1979, ApJS, 40, 487

Ramaty, R., Schwartz, R. A., Enome, S., & Nakajima, H. 1994, ApJ, 436, 941

Ramaty, R., Mandzhavidze, N., Kozlovsky, B. & Murphy, R. J. 1995, ApJ, 455, L193

Ramaty, R., Mandzhavidze, N., & Kozlovsky, B. 1996, in High Energy Solar Physics, ed. R. Ramaty, N. Mandzhavidze, & X.-M. Hua (New York:Am. Inst. Phys.), 374, 172

Ramaty, R. & Mandzhavidze, N. 2000, in Highly Energetic Physical Processes and Mechanisms for Emission from Astrophysical Plasmas, eds. Martens, Tsuruta, and Weber, (San Francisco:ASP), p. 123

Rank, G., Ryan, J., Debrunner, H., McConnell, M., & Schonfelder, V. 2001, A & A, 378, 1046

Reames, D. V., Meyer, J.-P., & von Rosenvinge, T. T. 1994, ApJS, 90, 649

Reames, D. V. 1995, Adv. Sp. Res., 15, No. 7, 41

Reames, D. V. 2002, ApJ, 571, L63

Sakurai, T., Ichimoto, K., Hiei, E., Irie, M., Kumagia, K., Miyashita, M., Nishino, Y., Yamaguchi, K., Fang, G., Kambry, M. A., Zhao, Z., Shinoda, K. 1992, Publ. Astron. Soc. Japan, 44, L7

Schmelz, J. T. 1993, ApJ, 408, 373

Schmelz, J. T., Nasraoui, K., Roames, J. K., Lippner, L. A., & Garst, J. W. 2005, ApJ, 634, L197

Schrijver, C. J., Hudson, H. S., Murphy, R. J., Share, G. H., & Tarbell, T. D. 2006 (submitted)

Share, G. H., Kurfess, J. D., and Theus, R. B. 1978, Nucl. Instr. Meth., 148, 531

Share, G. H., & Murphy, R. J. 1995, ApJ, 452, 933

Share, G. H., & Murphy, R. J. 1998, ApJ, 508, 876

Share, G. H., & Murphy, R. J. 1999, Proc. of 26th Int. Cosmic Ray Conference, Salt Lake City, SH1.2.05, Vol. 6, pg. 13

Share, G. H., & Murphy, R. J. 2000, AIP Conference Proceedings #528, eds. R. A. Mewaldt, J. R. Jokipii, M. A. Lee, E. Moebius, & T. H. Zurbuchen, pg. 181

Share, G. H., Murphy, R. J., Keiner, K., & de Sereville, N. 2002, ApJ, 573, 464

Share, G. H., Murphy, R. J., Smith, D. M., Schwartz, R. A., & Lin 2004, ApJ, 615, L169

Shemi, A. 1991, MNRAS, 251, 221

Smith, D. M., Share, G. H., Murphy, R. J., Schwartz, R. A., Shih, A. H., &Lin, R. P. 2003, ApJ, 595, L81

Stanislaus, T. D. S., et al. 2001, Nuclear Instruments & Methods in Physics Research, A462, 463

Sturrock,P.A., Weber,M., Wheatland,M.S., & Wolfson,R. 2001, ApJ, 548, 492

Tatischeff, V., Kozlovsky, B., Kiener, J., & Murphy,R. J. 2006, ApJ, in press

Tylka, A. J., Dietrich, W. F., Boberg, P. R., Smith, E. C., & Adams, J. H. 1996, IEEE Trans. on Nucl. Sci., 43, No. 62758

Tylka, A. J., Boberg, P. R., Cohen, C. M. S., Dietrich, W. F., Maclennan, C. G., Mason, G. M., Ng, C. K, & Reames, D. V. 2002, ApJ, 581, L119

Tylka, A. J., Cohen, C. M. S., Dietrich, W. F., Lee, M. A., Maclennan, C. G., Mewaldt, R. A., Ng, C. K, & Reames, D. V. 2005, ApJ, 625, 474

Vernazza, J. E., Avrett, E. H., & Loeser, R. 1981, ApJS, 45, 635

Wang, H. T., & Ramaty R. 1974, Sol. Phys., 36, 129

White, S. M., Kundu, M. R., Garaimov, V. I., Yokoyama, T., & Sato, J. 2002, ApJ, 576, 505

Zweibel, E. G., & Haber, D. 1983, ApJ, 264, 648

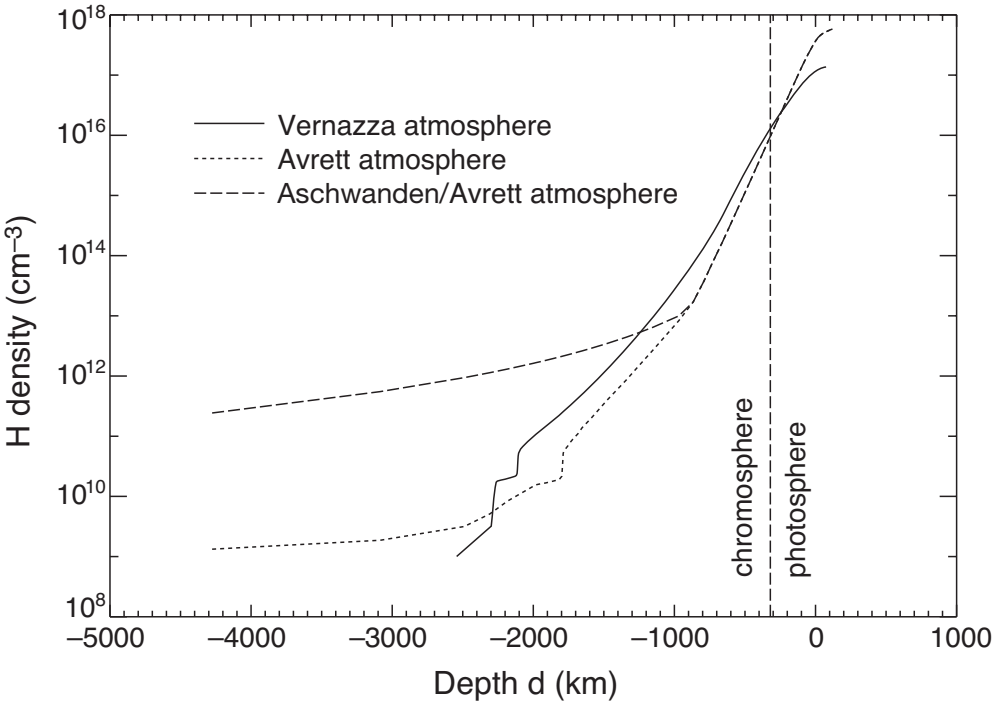

Fig. 1.— Density vs. height in the solar atmosphere for the three atmospheric models considered here: Vernazza (Vernazza et al. 1981), Avrett (Avrett 1981) and *RHESSI*/Avrett.

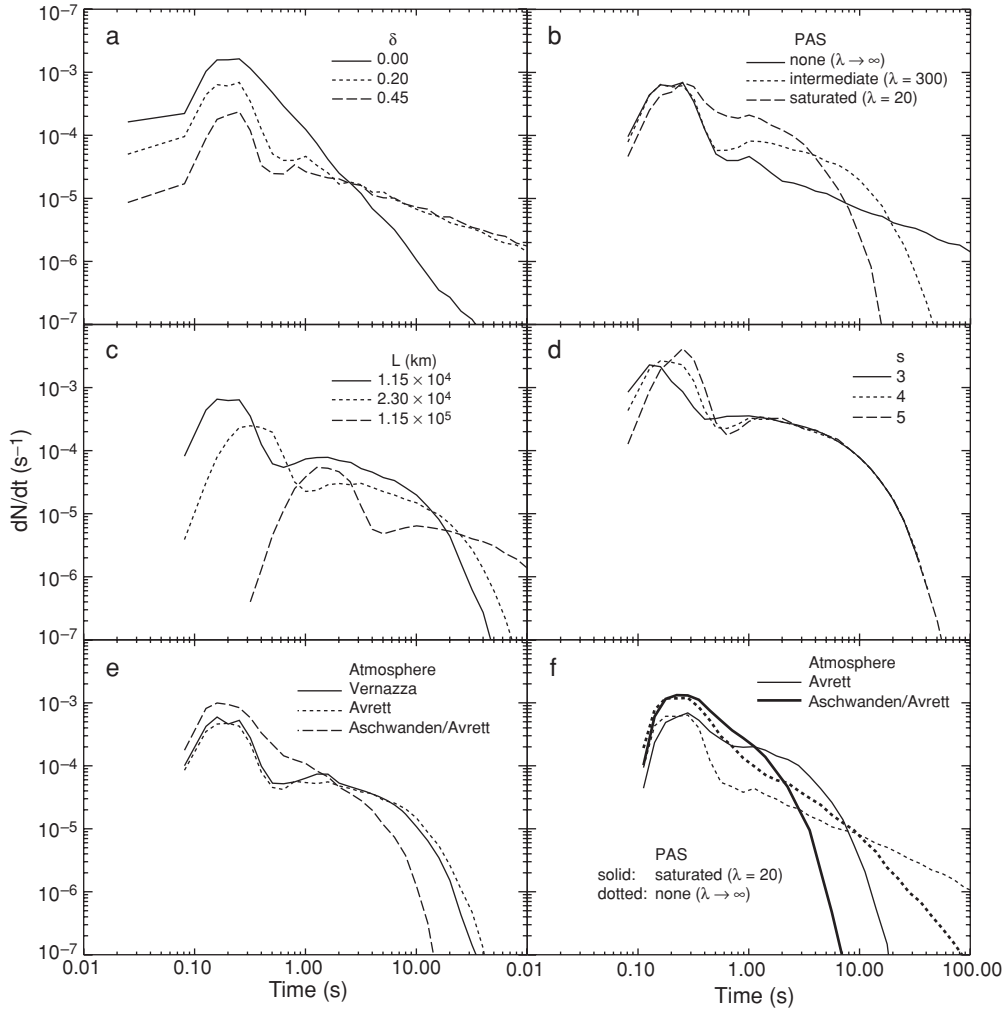

Fig. 2.— Dependence of the nuclear interaction rate time history on various parameters: a) magnetic convergence (δ), b) PAS (λ), c) loop length (L), d) spectral index (s), and e) atmospheric model. Panel f shows the range of the affect that PAS has on the Avrett and *RHESSI*/Avrett atmospheric models. For each panel, the other parameters are fixed at the values noted in the text. All yields are normalized to 1 accelerated proton of energy greater than 30 MeV.

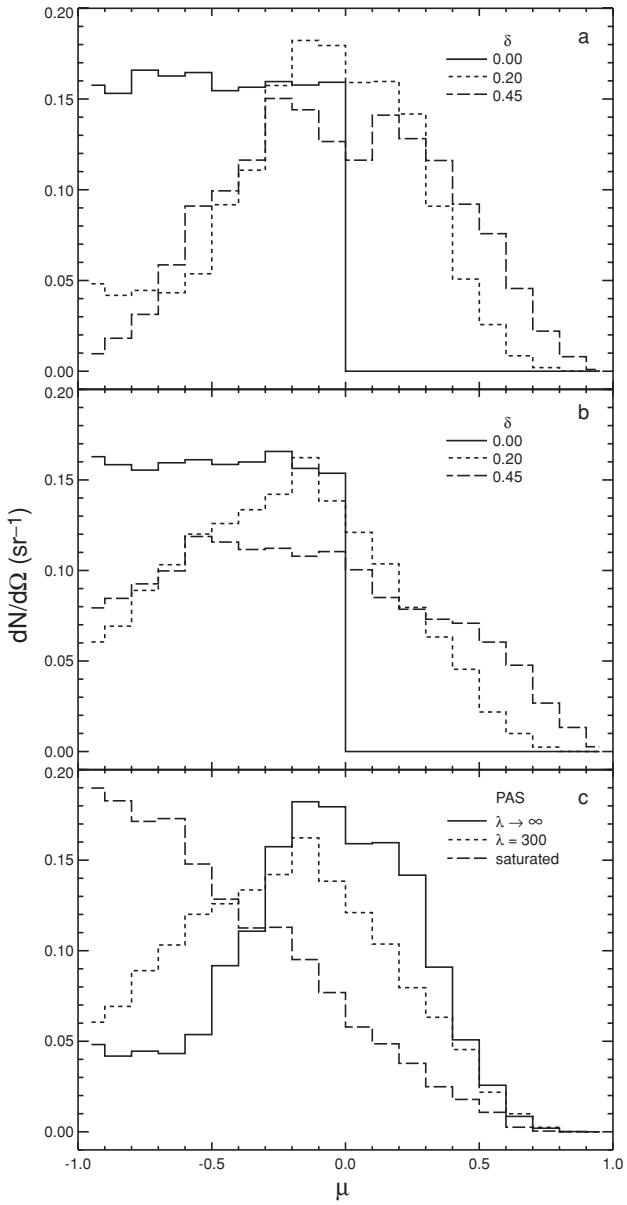

Fig. 3.— Dependence of the interacting particle angular distribution on various parameters: a) magnetic convergence (δ) with no PAS ($\lambda \rightarrow \infty$), b) magnetic convergence (δ) with λ = 300, and c) PAS (with $\delta = 0.20$). For each panel, the other parameters are fixed at the values noted in the text. $\mu = cos(\theta)$ where θ is the angle between the normal to the solar surface and the direction of the ion. $\theta = 0^\circ$ ($\mu = 1$) is directed outward from the Sun, $\theta = 180^\circ$ ($\mu = -1$) is directed inward into the Sun, and $\theta = 90^\circ$ ($\mu = 0$) is directed parallel to the surface of the Sun. The distributions are normalized to unity.

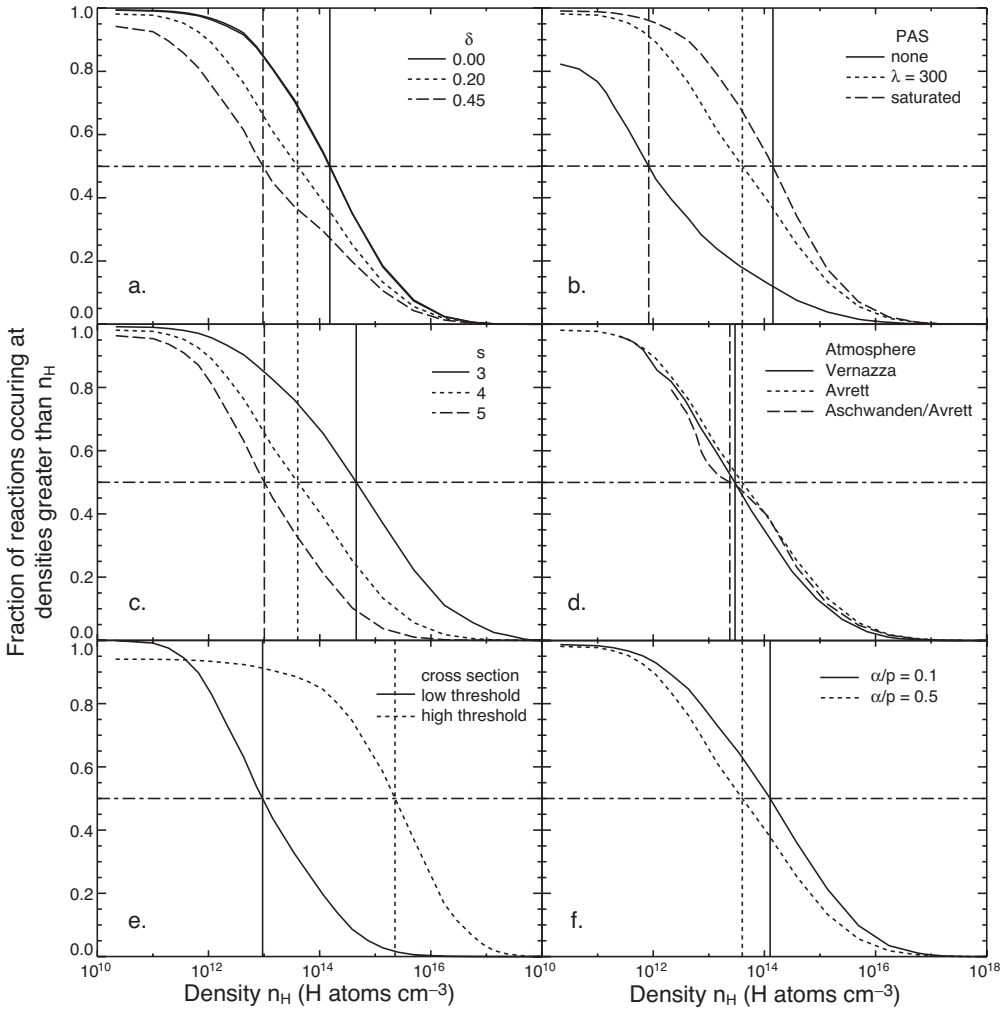

Fig. 4.— Dependence of the depth distribution of the nuclear interactions on various parameters: a) magnetic convergence (δ), b) PAS (λ), c) spectral index (s), d) atmospheric model, e) interaction cross section and f) accelerated α/proton ratio. For each panel, the abscissa is the density in the solar atmosphere which can be related to depth through the atmospheric model. Also for each panel, the other parameters are fixed at the values noted in the text.

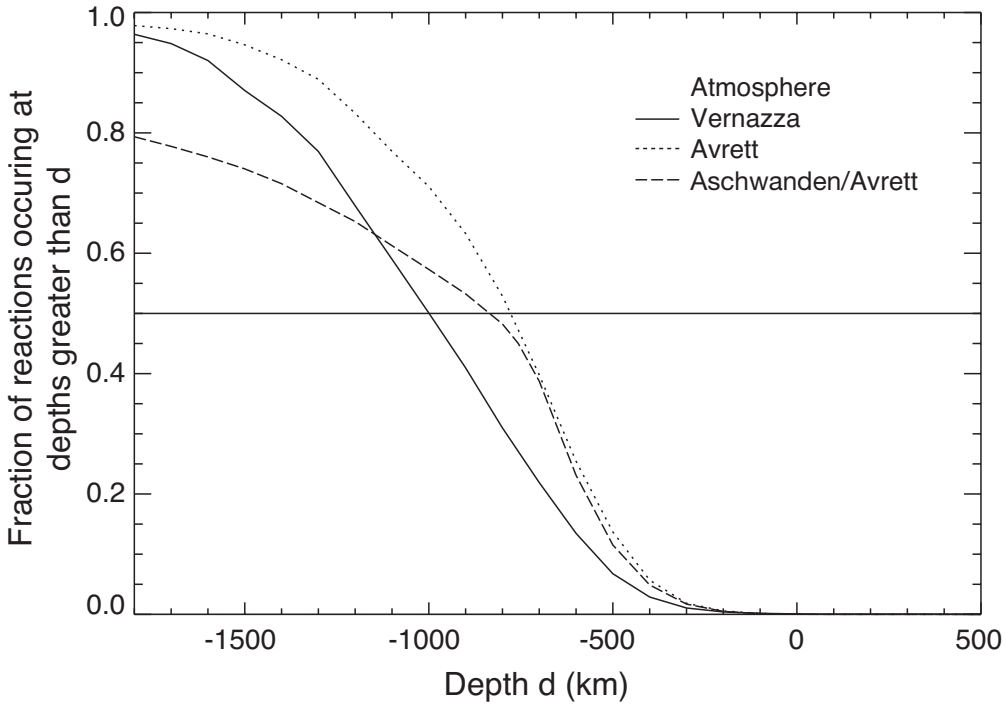

Fig. 5.— Dependence of the depth distribution of the nuclear interactions on the atmospheric model as in Figure 4d but with the abscissa being depth in the atmosphere. For each panel, the other parameters are fixed at the values noted in the text.

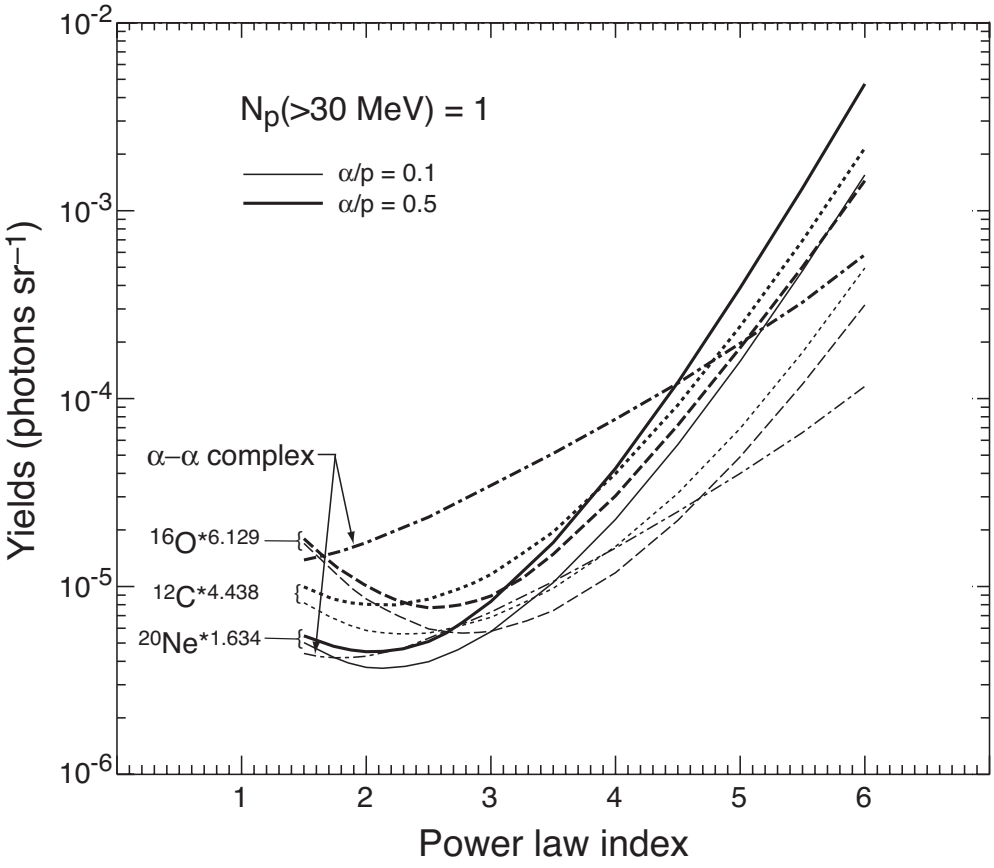

Fig. 6.— Calculated yields of the 1.634 MeV (^{20}Ne), 4.438 MeV (^{12}C), 6.129 MeV (^{16}O), and ~ 0.45 MeV $\alpha - \alpha$ complex as functions of the accelerated-ion power-law spectral index for accelerated α/proton = 0.5 (thick lines) and 0.1 (thin lines). Deexcitation line yields do not depend on loop parameters. All yields are normalized to 1 accelerated proton of energy greater than 30 MeV.

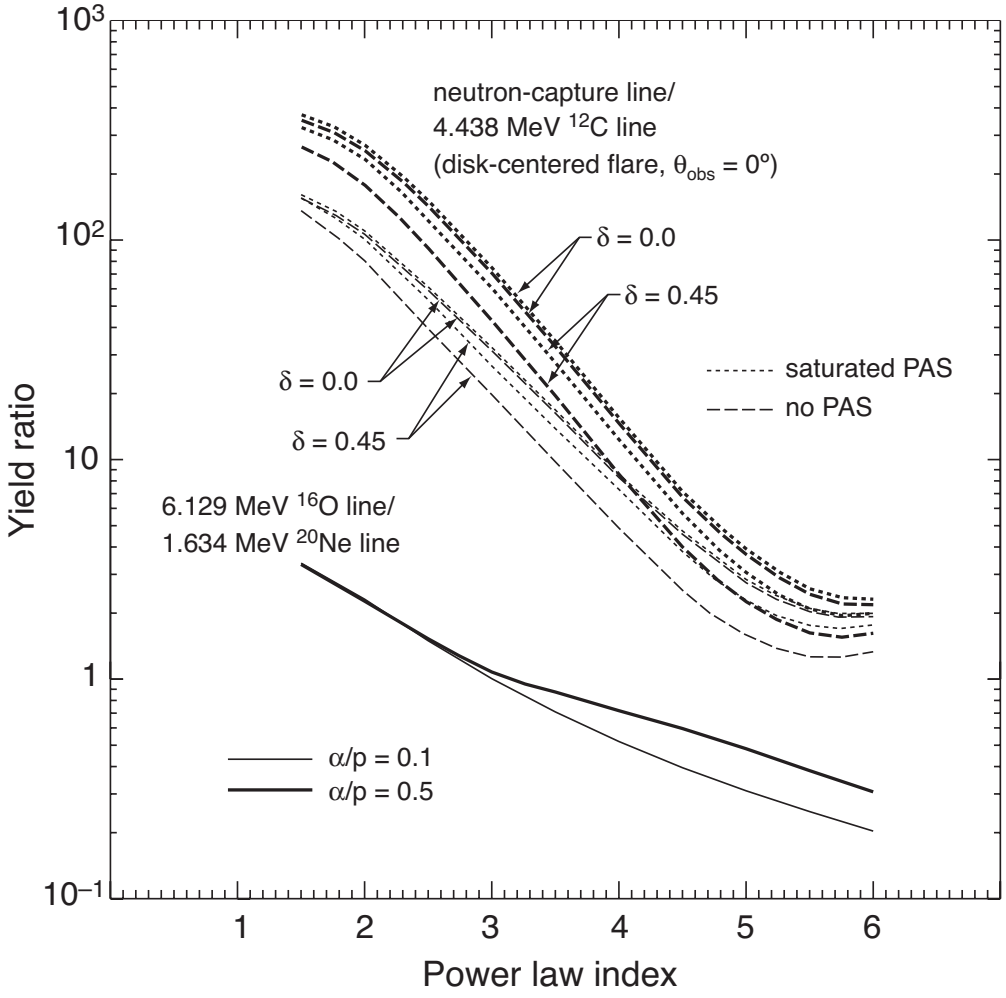

Fig. 7.— Calculated fluence ratios of the 6.129 MeV (^{16}O)/1.634 MeV (^{20}Ne) and 2.223 MeV (neutron-capture)/4.438 MeV (^{12}C) lines as functions of the power law spectral index for accelerated α/proton = 0.5 (thick lines) and 0.1 (thin lines). The latter ratio is for a disk-centered flare and is shown for both no PAS (dashed) and saturated PAS (solid). For each level of PAS, the ratio is shown for magnetic convergences of $\delta = 0.0$ and 0.45, as indicated in the figure.

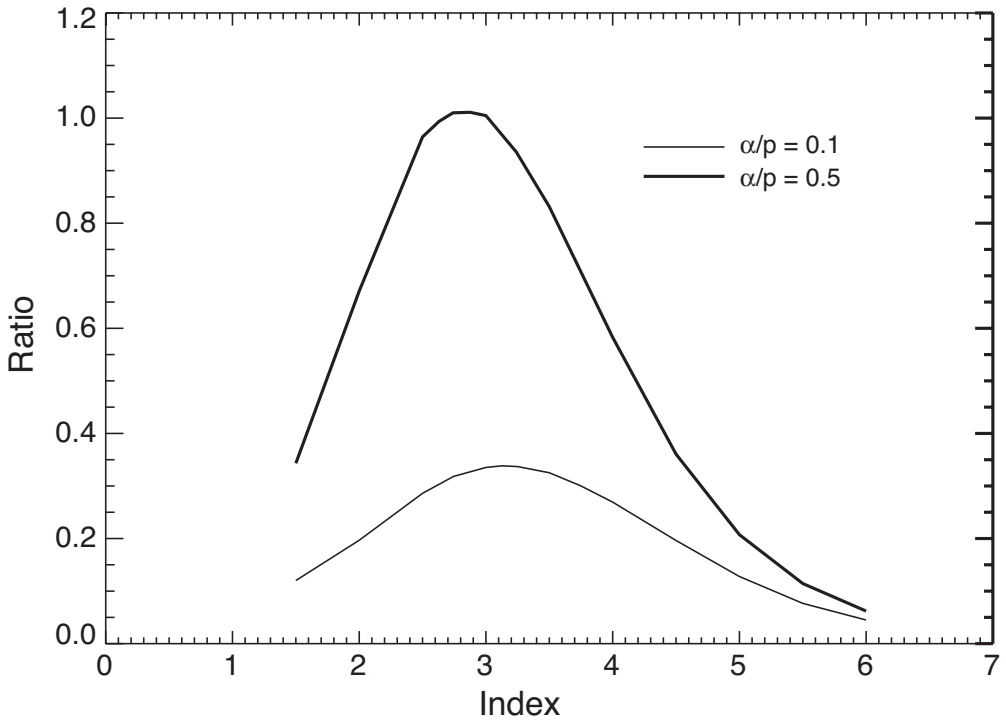

Fig. 8.— Calculated fluence ratio of the $\alpha-\alpha$ complex and the sum of the strongest high-FIP lines (1.63, 4.44, 6.13 and $\sim$7 MeV from ^{20}Ne, ^{12}C, ^{16}O, and ^{16}O, respectively) as a function of spectral index.

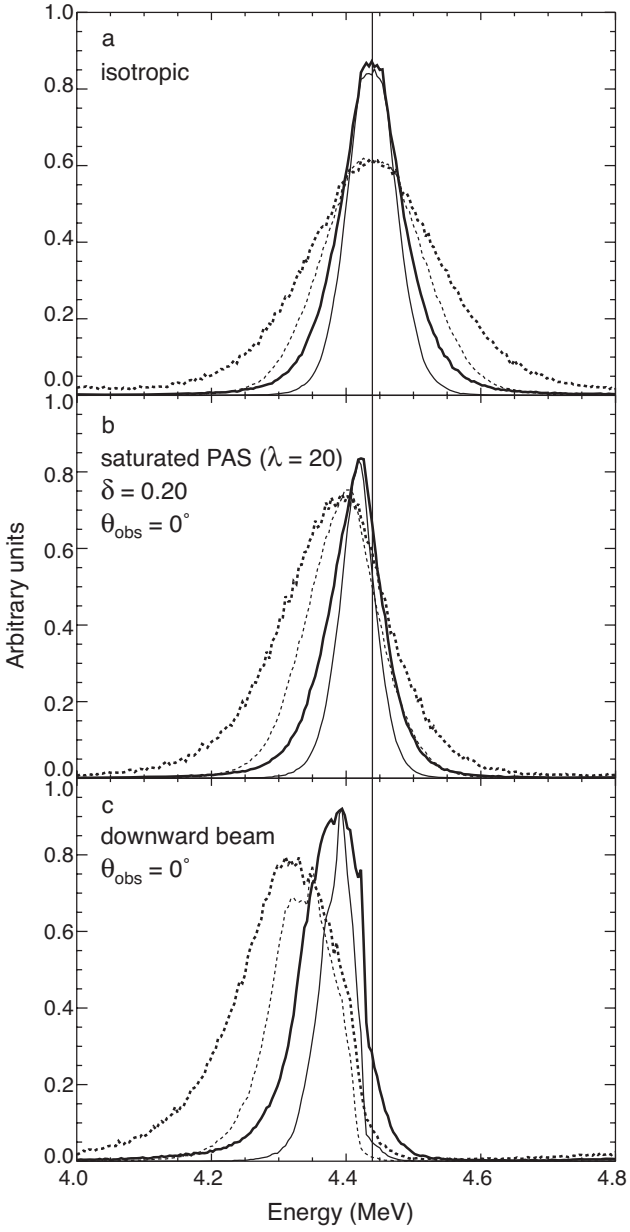

Fig. 9.— Line profiles of the 4.438 MeV ^{12}C line resulting from various interacting-particle angular distributions for a disk-centered flare: a) isotropic, b) saturated PAS and magnetic convergence $\delta = 0.20$, and c) downward beam. The solid and dotted curves are for interactions due to protons and α-particles, respectively. The thick and thin curves are for power-law spectral indexes of 2.75 and 4.75, respectively. (Note: the profiles have been renormalized to facilitate comparison.).

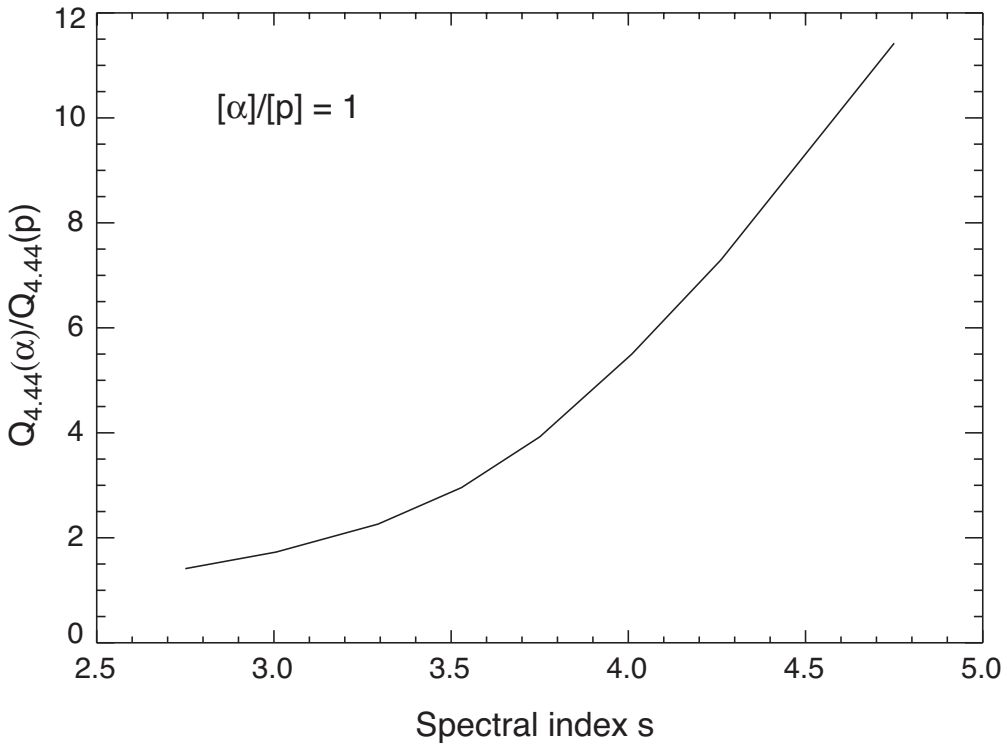

Fig. 10.— Ratio of the 4.438 MeV ^{12}C line yields from α particles and from protons as a function of spectral index for equal numbers of α particles and protons.

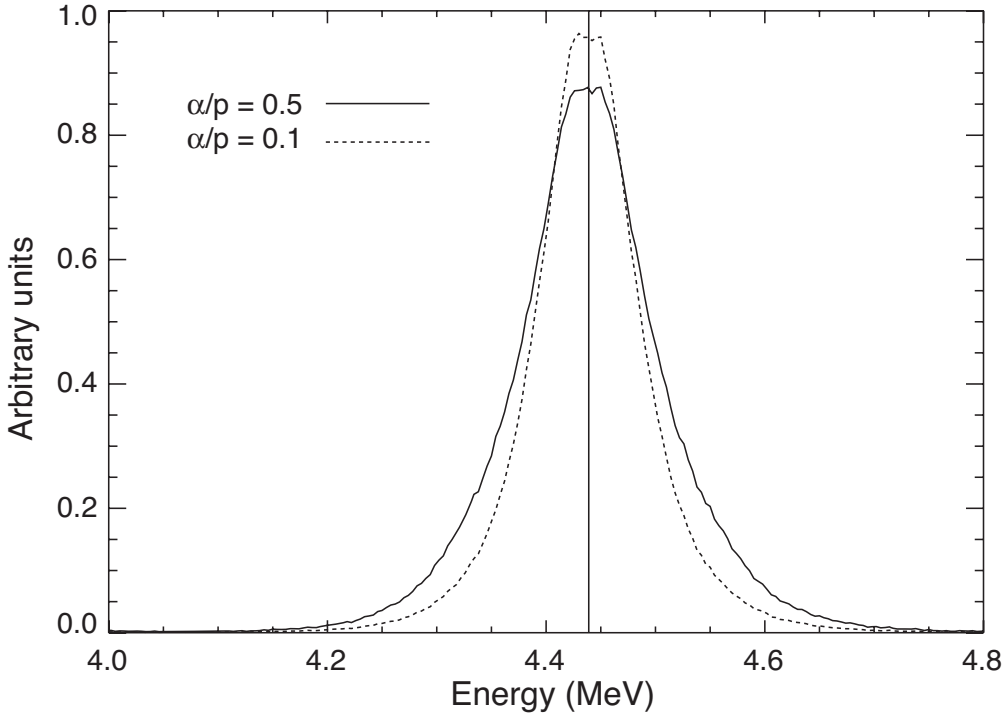

Fig. 11.— 4.438 MeV ^{12}C line shapes for $s = 3.75$ and α/proton ratios of 0.1 (dotted) and 0.5 (solid). The accelerated ion angular distribution is isotropic.

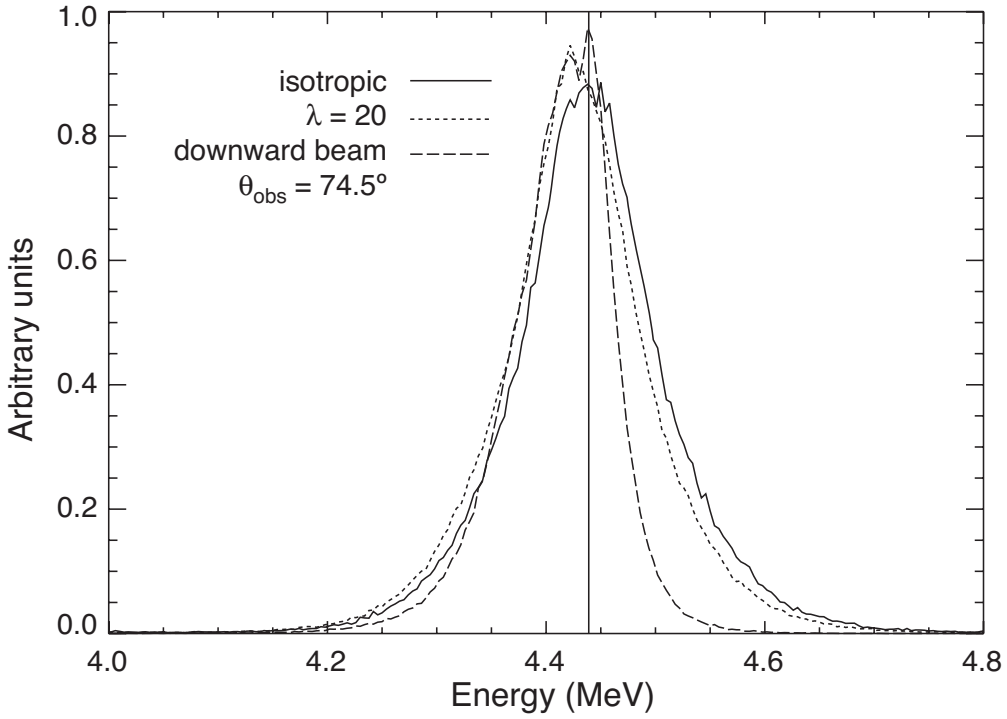

Fig. 12.— 4.438 MeV ^{12}C line profiles resulting from three angular distributions (isotropic, saturated PAS ($\lambda = 20$), and downward beam) for a flare occurring at a heliocentric angle of 74.5° (as for the 1991 June 4 flare). The α/proton ratio is 0.5 and $s = 4$.

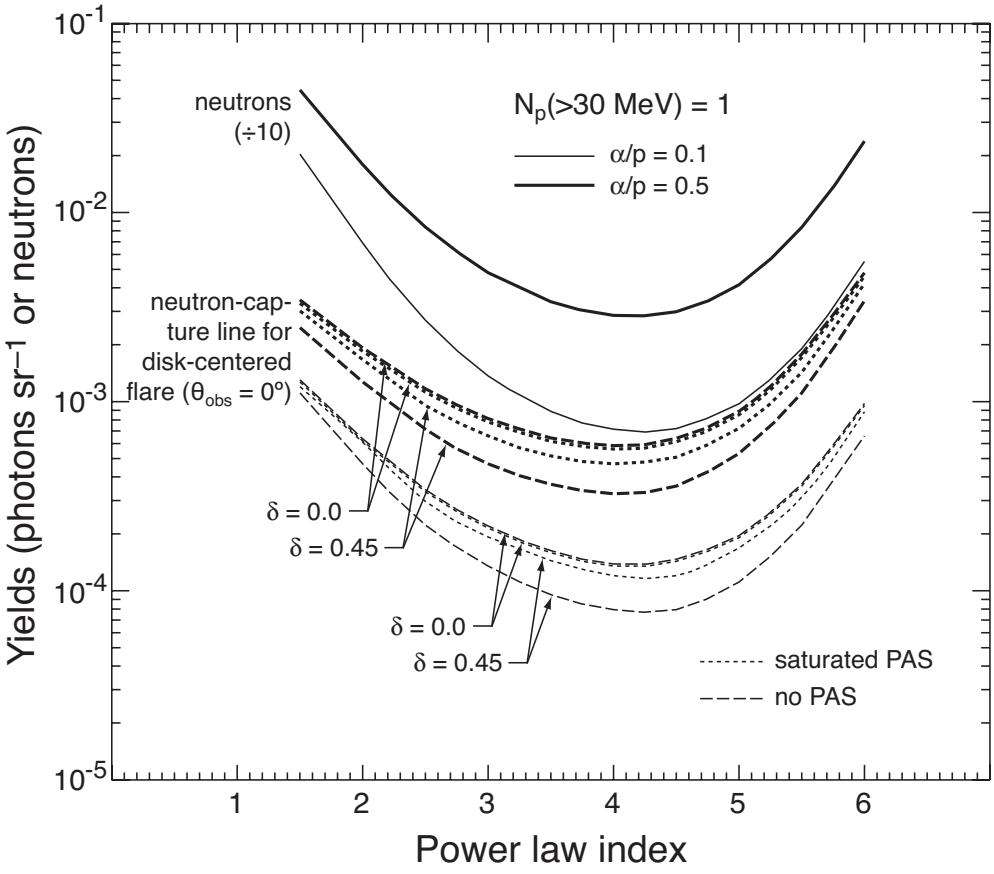

Fig. 13.— Calculated yields of total neutrons and the 2.223 MeV neutron-capture line (for a disk-centered flare) as functions of the accelerated-ion power-law spectral index for α/proton = 0.5 (thick lines) and 0.1 (thin lines). The total neutron yield has been divided by a factor of 10 for plotting purposes. The neutron-capture curves are for a disk-centered flare and are plotted for both no PAS (dashed) and saturated PAS (dotted). For each PAS, yields for magnetic convergences of $\delta = 0.0$ and 0.45 are shown, as indicated in the figure. All yields are normalized to 1 accelerated proton of energy greater than 30 MeV.

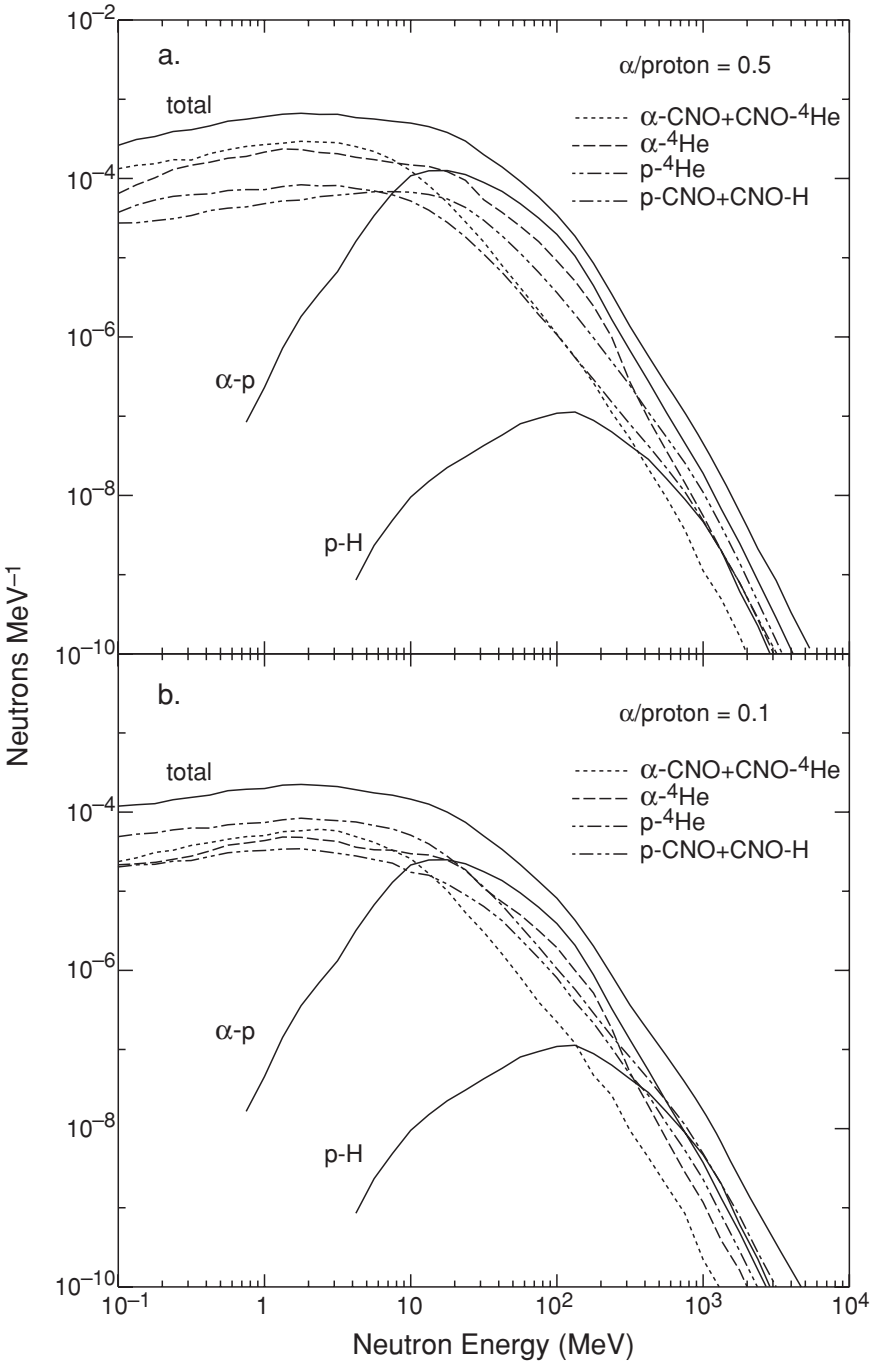

Fig. 14.— Angle-integrated neutron energy spectra calculated for an accelerated-ion power-law spectral index $s = 4$, saturated PAS, $\delta = 0.2$, the compositions given in Table 1, and accelerated α/proton = 0.5 (panel a) and 0.1 (panel b). Contributions to the total production by each of the various reactions are shown. All yields are normalized to 1 accelerated proton of energy greater than 30 MeV.

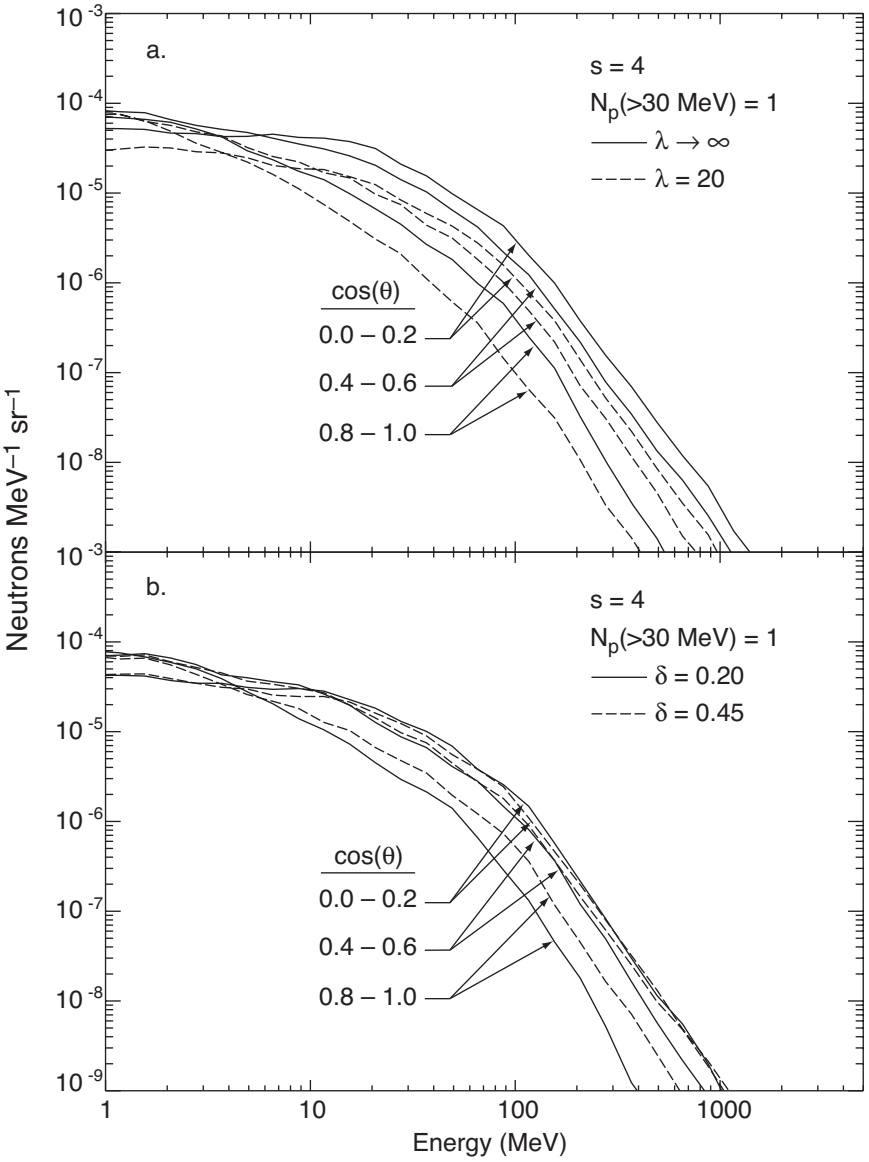

Fig. 15.— Angle-dependent escaping neutron spectra at the Sun. For loops perpendicular to the solar surface, θ is the angle relative to the surface normal, with $\theta = 0°$ being the direction away from the Sun, and corresponds to the heliocentric angle of a flare, $\theta_{\rm obs}$. For a disk-centered flare, $\cos(\theta) = 1$. Panel a): no PAS (solid curves) and saturated PAS (dashed curves) with $\delta = 0.20$. Panel b: magnetic convergence $\delta = 0.20$ (solid curves) and 0.45 (dashed curves) with $\lambda = 300$. All yields are normalized to 1 accelerated proton of energy greater than 30 MeV.

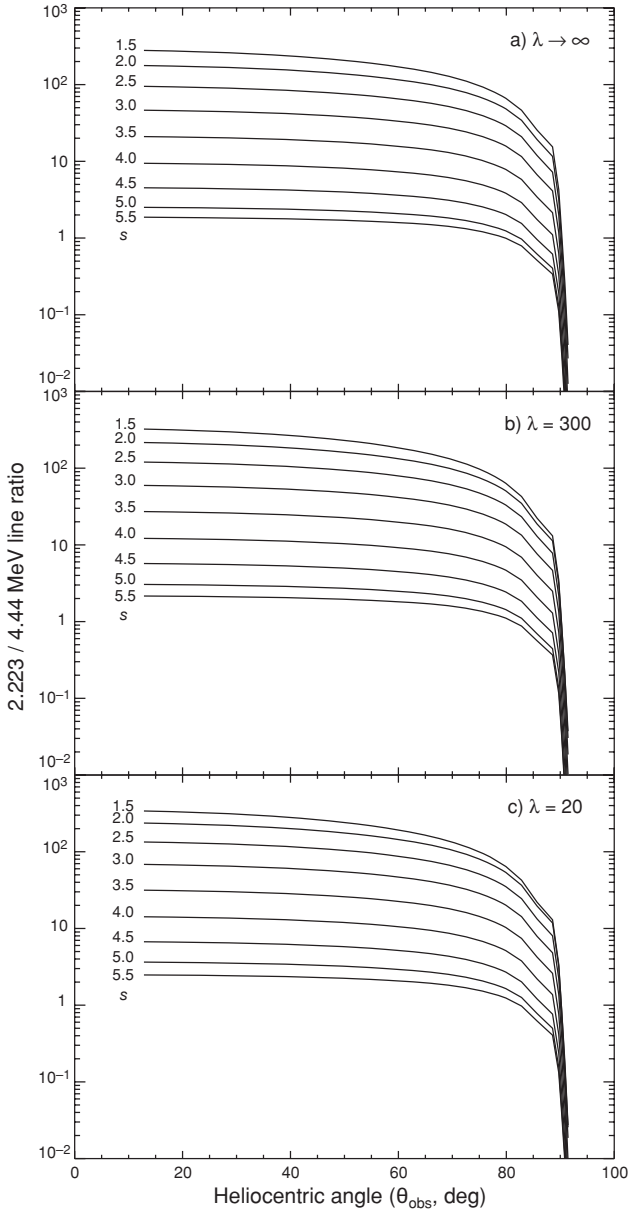

Fig. 16.— The 2.223 MeV (neutron capture)/4.438 MeV (^{12}C) line fluence ratio as a function of the flare heliocentric angle ($\theta_{\rm obs}$.), parameterized by spectral index (s): a) no PAS, b) nearly-saturated PAS, and c) saturated PAS. fig16

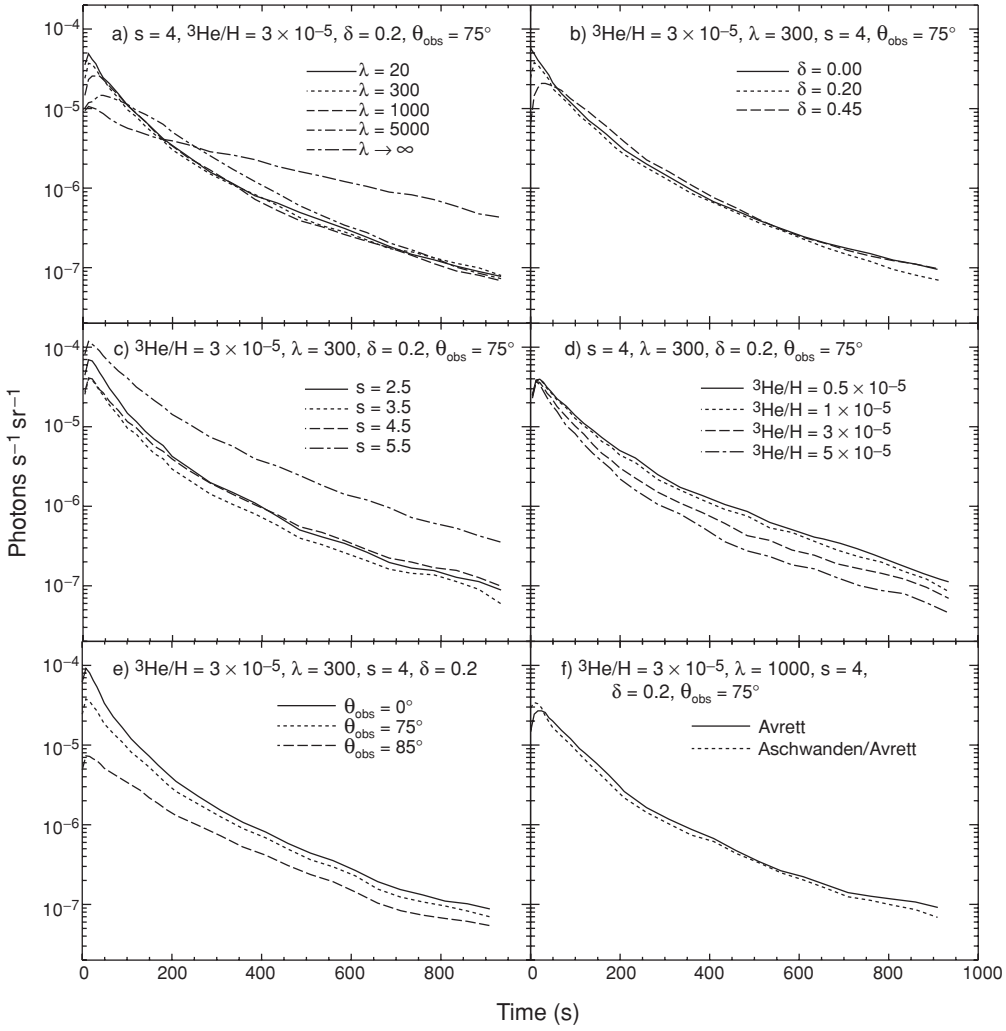

Fig. 17.— Dependence of the 2.223 MeV neutron-capture line time history on various parameters: a) PAS (λ), b) magnetic convergence (δ), c) spectral index (s), d) ambient ^{3}He/H, e) flare heliocentric angle ($\theta_{\rm obs}$), and f) atmospheric model. For each panel, the other parameters are fixed at the values noted in the text. All yields are normalized to 1 accelerated proton of energy greater than 30 MeV.

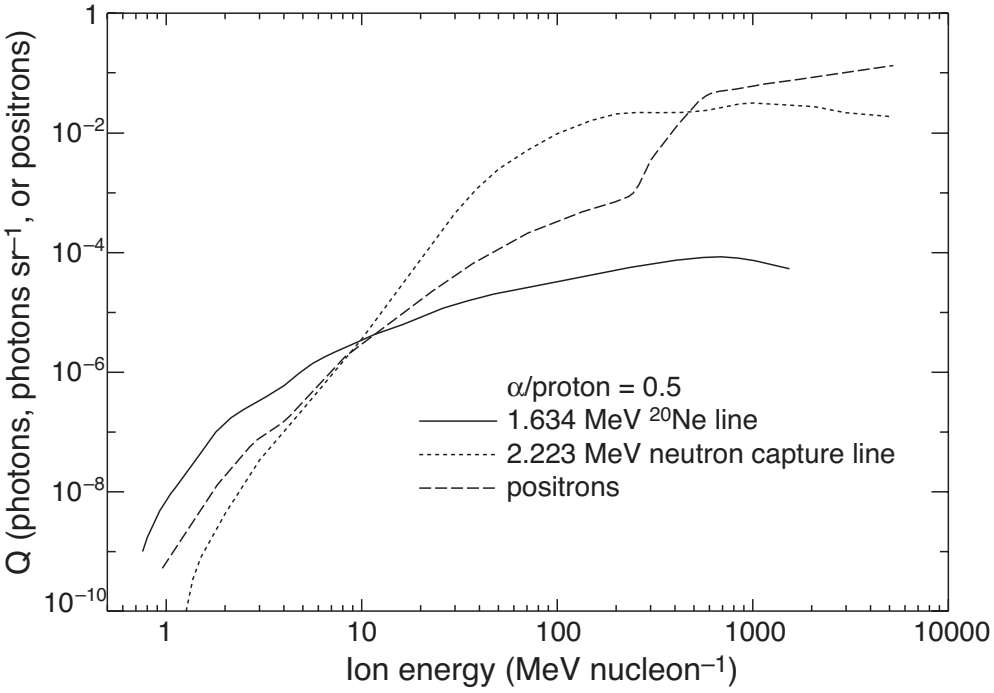

Fig. 18.— 1.634 MeV ^{20}Ne deexcitation line, 2.223 MeV neutron capture line and positron yields per accelerated proton of given energy. For the Ne line, the yield is total photons, for the neutron capture line, the yield is photons sr^{-1} at heliocentric angle $\theta_{\rm obs} = 75°$, and for positrons, the yield is total positrons.

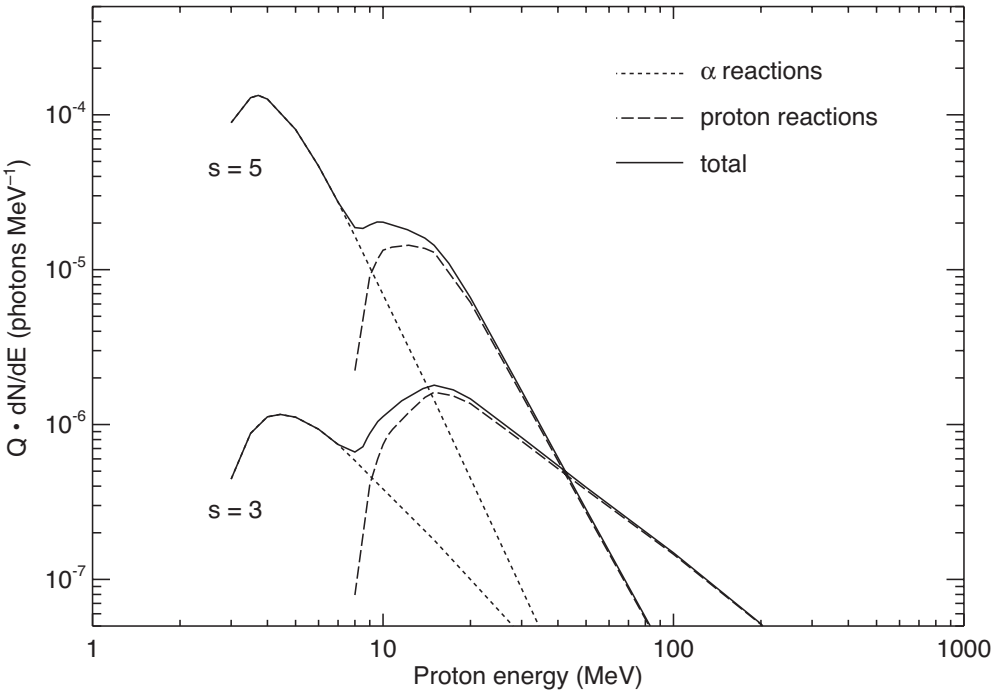

Fig. 19.— Yield of the 6.129 MeV ^{16}O line weighted by accelerated ion power law spectra with indexes $s = 3$ and 5. The contribution to the line from accelerated protons and α particles are separately shown.

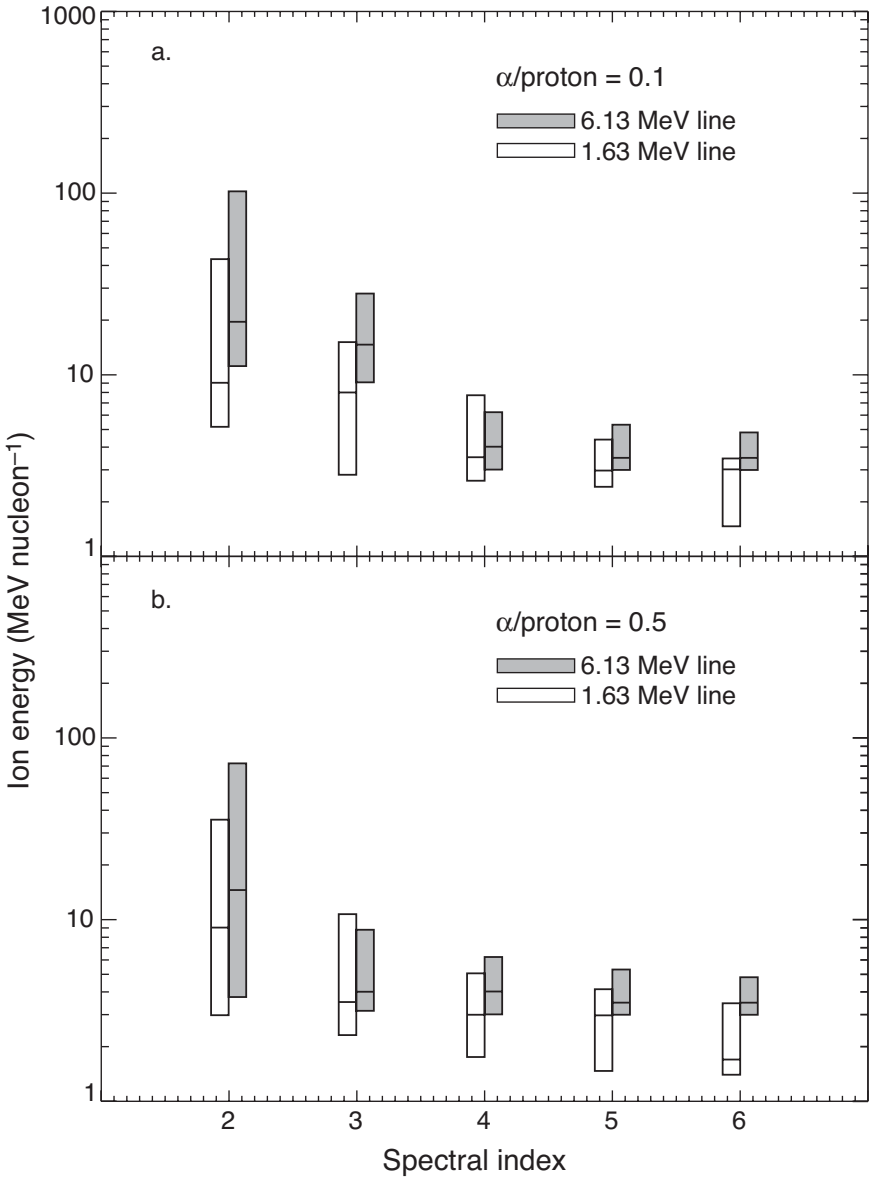

Fig. 20.— Effective accelerated ion energies for production of the 1.634 MeV ^{20}Ne line (white boxes) and 6.129 MeV ^{16}O line (grey boxes) as a function of spectral index. The effective energy ranges are the 50% yield range as defined in the text. Panel a is for accelerated α/proton = 0.1 and panel b is for 0.5.

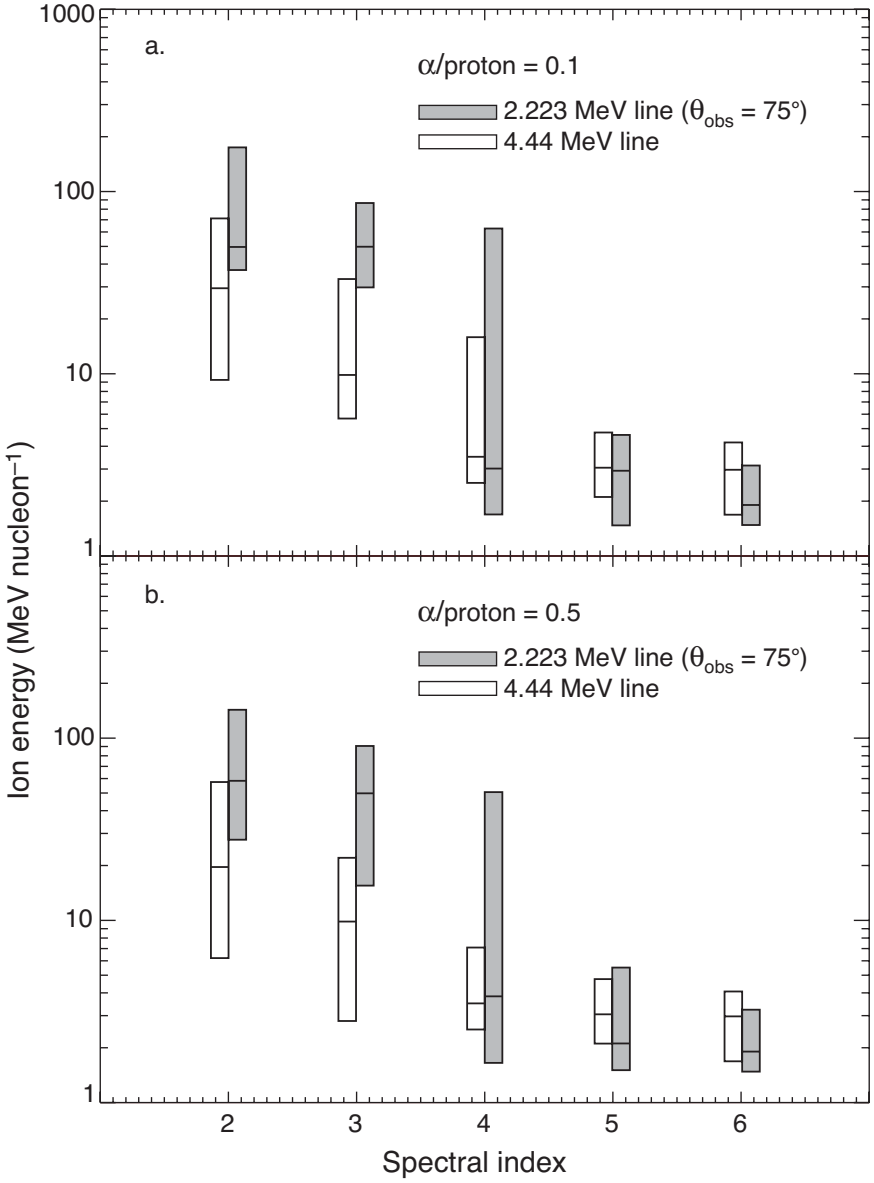

Fig. 21.— Effective accelerated ion energies for production of the 4.438 MeV ^{12}C line (white boxes) and 2.223 MeV neutron capture line (grey boxes) as a function of spectral index. The effective energy ranges are the 50% yield range as defined in the text. Panel a is for accelerated α/proton = 0.1 and panel b is for 0.5. For the neutron capture line, $\lambda = 300$, $\delta = 0.2$, $L = 11{,}500$ km, and $\theta_{\rm obs} = 75°$.

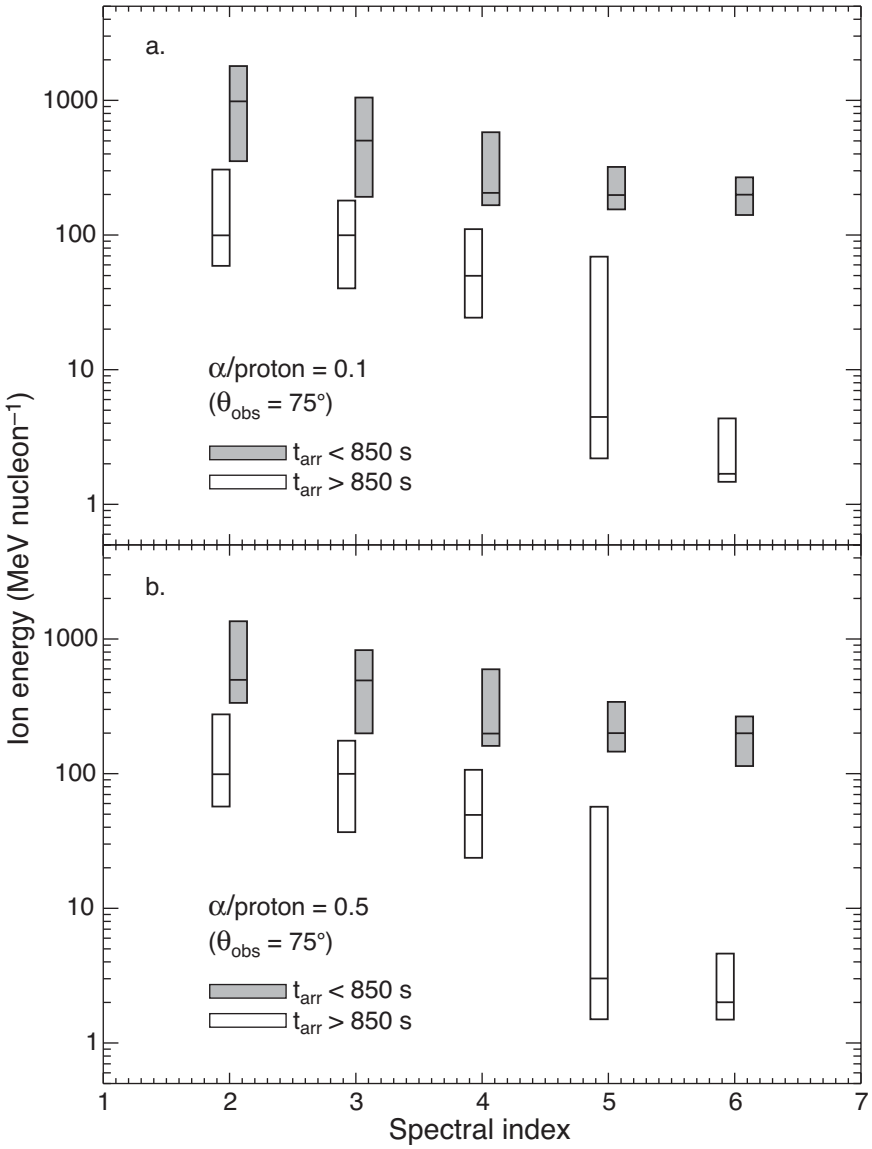

Fig. 22.— Effective accelerated ion energies for production of neutrons arriving at Earth before (grey boxes) and after (white boxes) a time $t_{\rm arr} = 850$ s after the release of the accelerated ions into the magnetic loop at the Sun as a function of spectral index. The effective energy ranges are the 50% yield range as defined in the text. Panel a is for accelerated α/proton = 0.1 and panel b is for 0.5. For these calculations, $\lambda = 300$, $\delta = 0.2$, $L = 11{,}500$ km, and $\theta_{\rm obs} = 75°$.

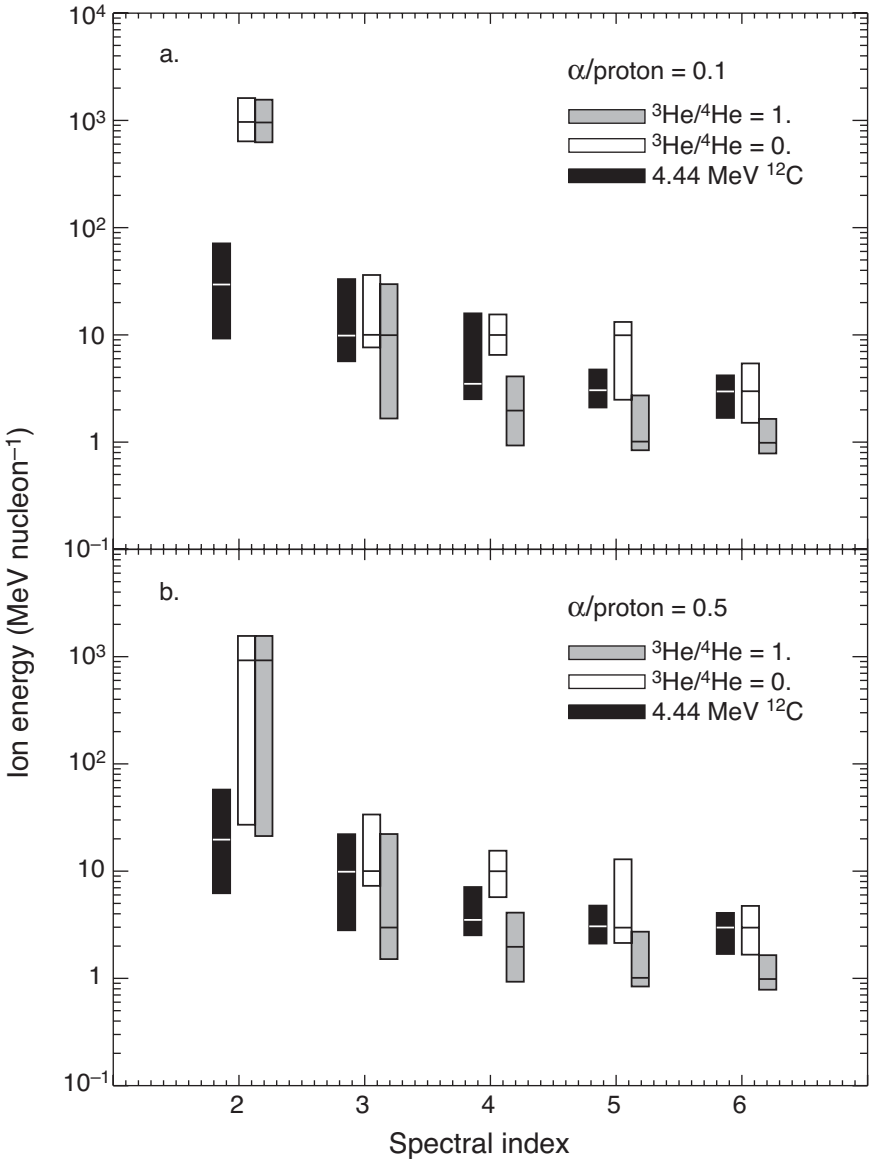

Fig. 23.— Effective accelerated ion energies for production of positrons as a function of spectral index for accelerated ^{3}He/^{4}He = 0 (white boxes) and 1 (grey boxes). The effective energy ranges are the 50% yield range as defined in the text. Panel a is for accelerated α/proton = 0.1 and panel b is for 0.5. Also shown are the effective energies for the 4.438 MeV ^{16}O line (black boxes) from Figure 21.

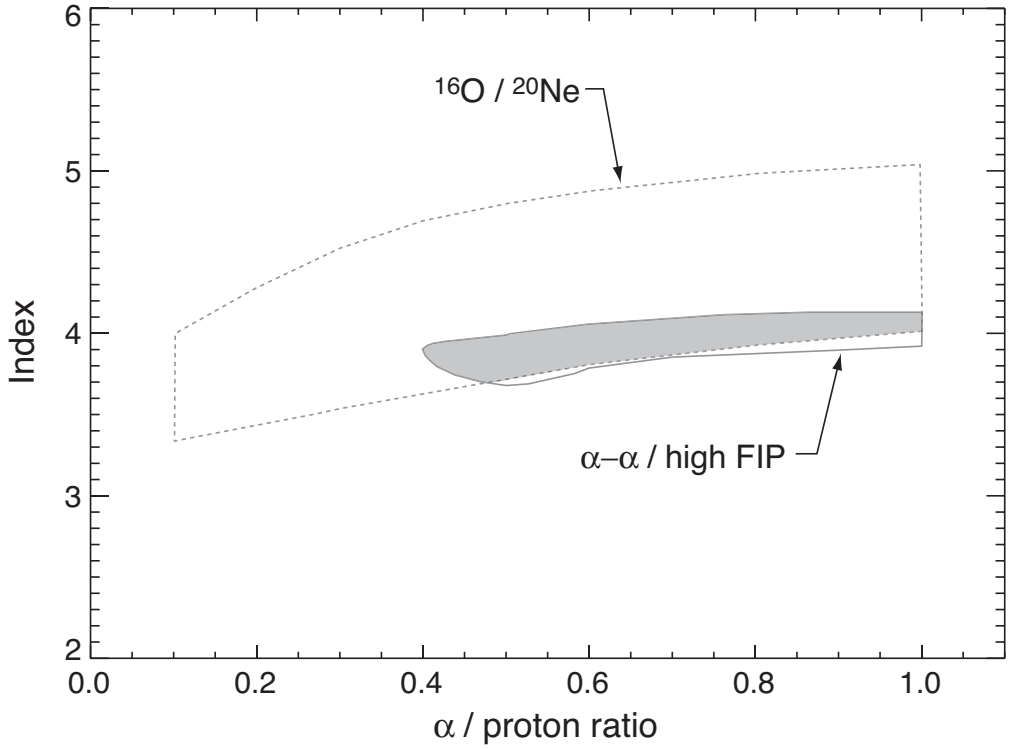

Fig. 24.— Two-parameter 99% confidence contours for combinations of accelerated α/proton ratio and spectral index from the α-α complex–high FIP line fluence ratio comparison (dotted curve) and the 6.129 MeV ^{16}O–1.634 MeV ^{20}Ne line fluence ratio comparison (solid curve) for the June 4 flare. The grey area represents the overlap of the 99% confidence regions from both analyses.

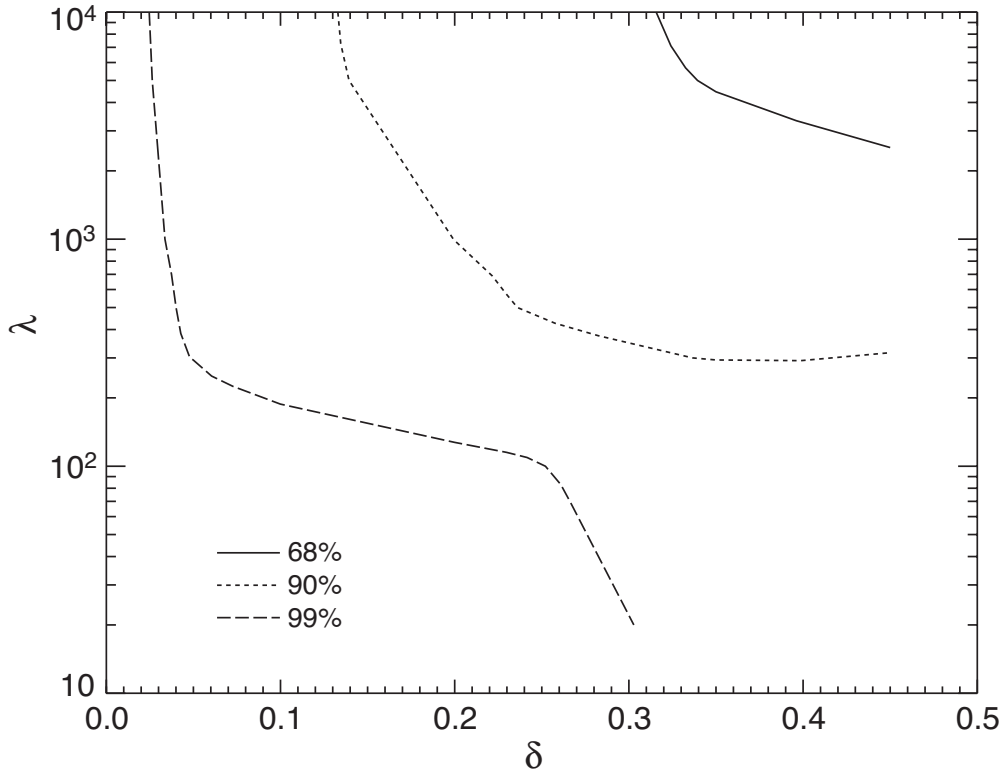

Fig. 25.— Two-parameter confidence contours for combinations of δ and λ resulting from the line shift analysis of the June 4 flare.

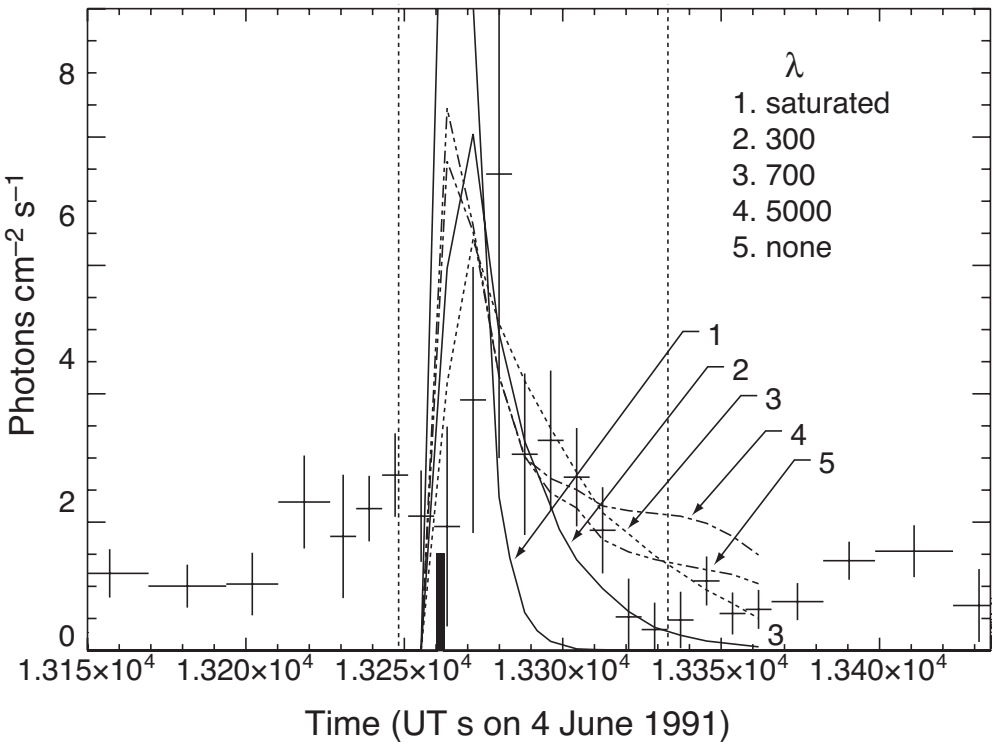

Fig. 26.— Comparison of measured high-FIP deexcitation line time history at the peak of the June 4 flare with calculated time histories for various values of PAS.

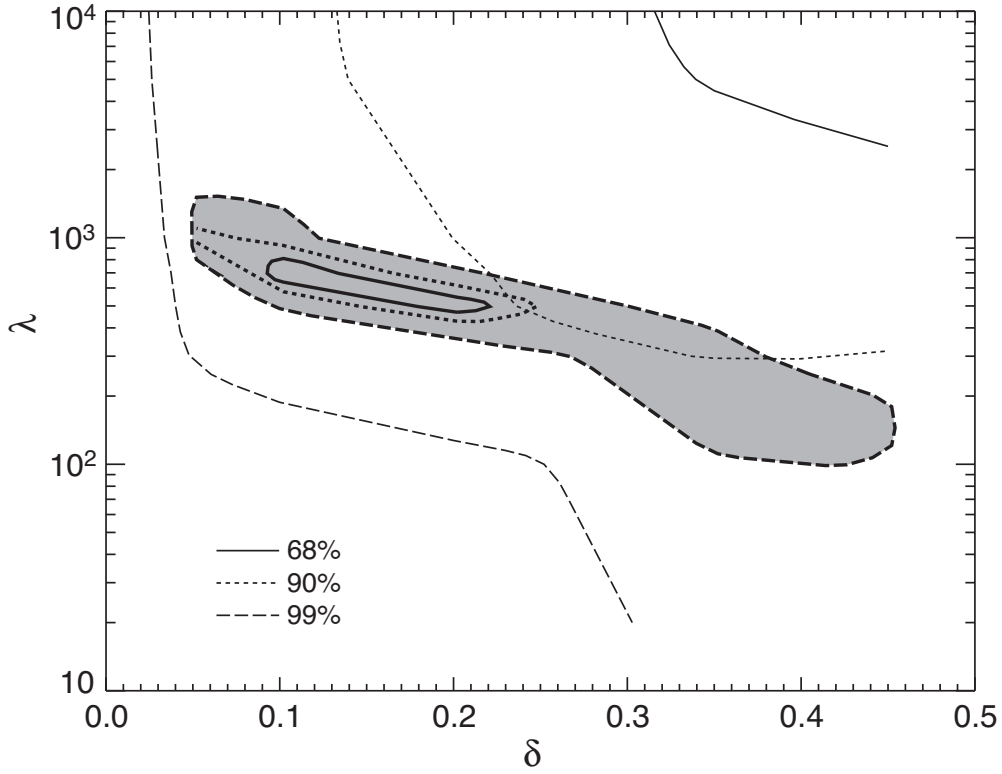

Fig. 27.— Two-parameter confidence contours (thick curves) for combinations of δ and λ resulting from the time history analysis of the June 4 flare assuming instantaneous accelerated ion release at 13260 s UT. Also shown are the contours shown in Figure 19 from the line shift analysis (thin curves). The grey area represents the overlap of the 99% confidence regions from both analyses.

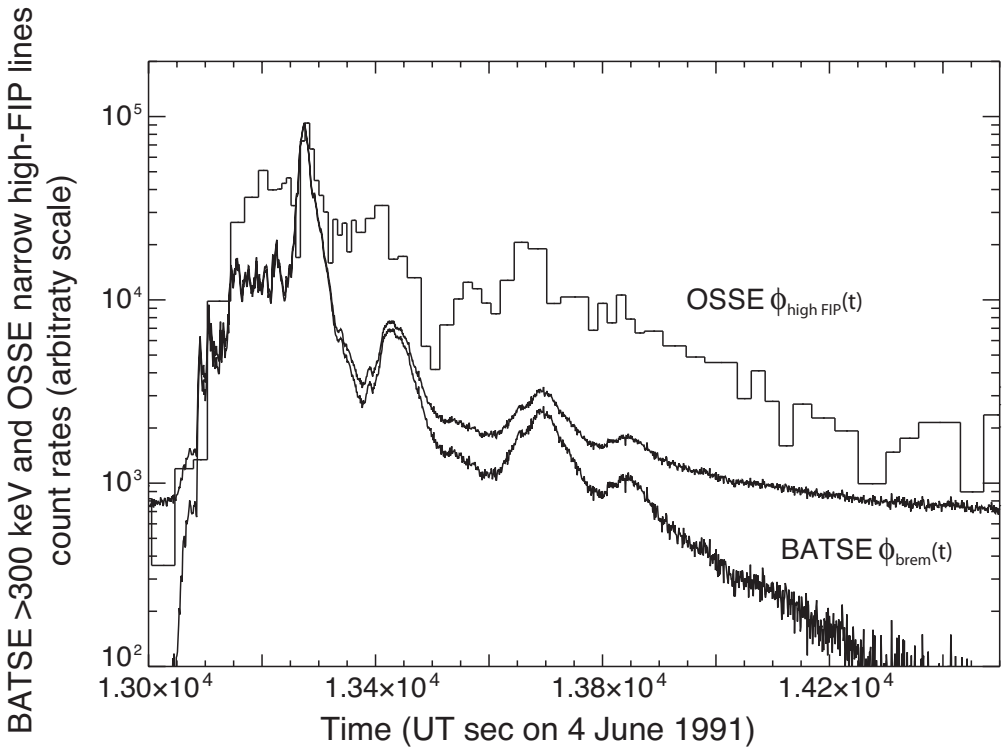

Fig. 28.— Time histories of the high-FIP narrow deexcitation line flux observed with OSSE from the June 4 flare and the >300 keV bremsstrahlung flux observed with BATSE. The upper BATSE data are without background subtraction and the lower data are with a simple linear background subtraction.

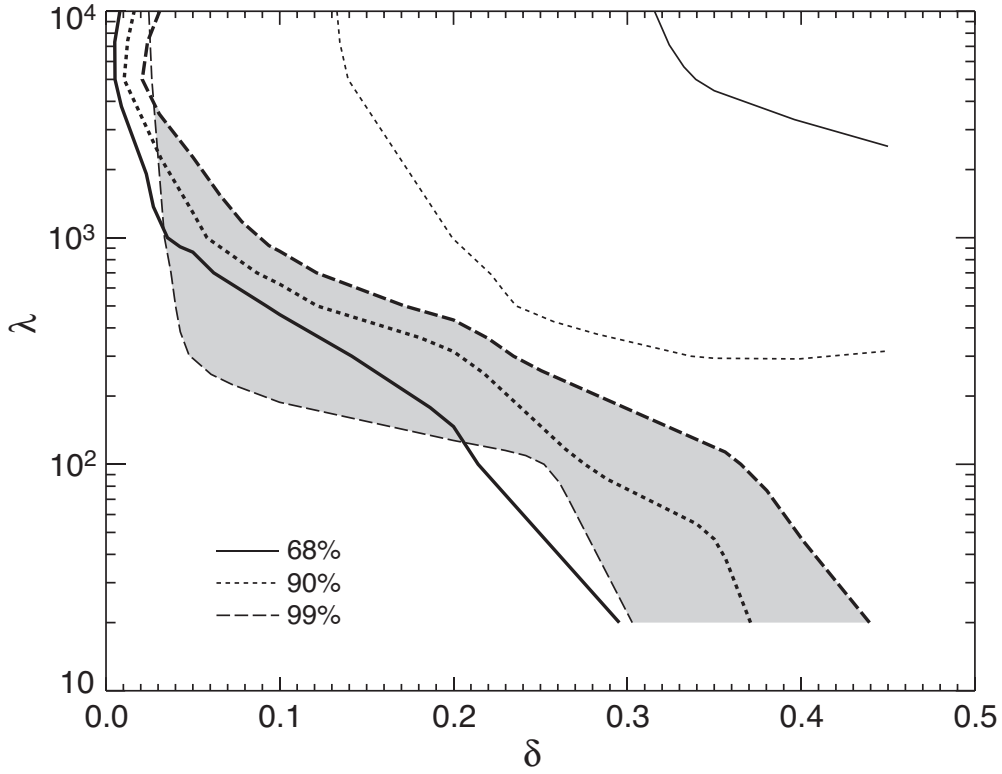

Fig. 29.— Two-parameter confidence contours (thick curves) for combinations of δ and λ resulting from the time history analysis of the June 4 flare assuming the accelerated ion release time history is given by the >300 keV BATSE time history. Also shown are the contours shown in Figure 19 from the line shift analysis (thin curves). The grey area represents the overlap of the 99% confidence regions from both analyses.

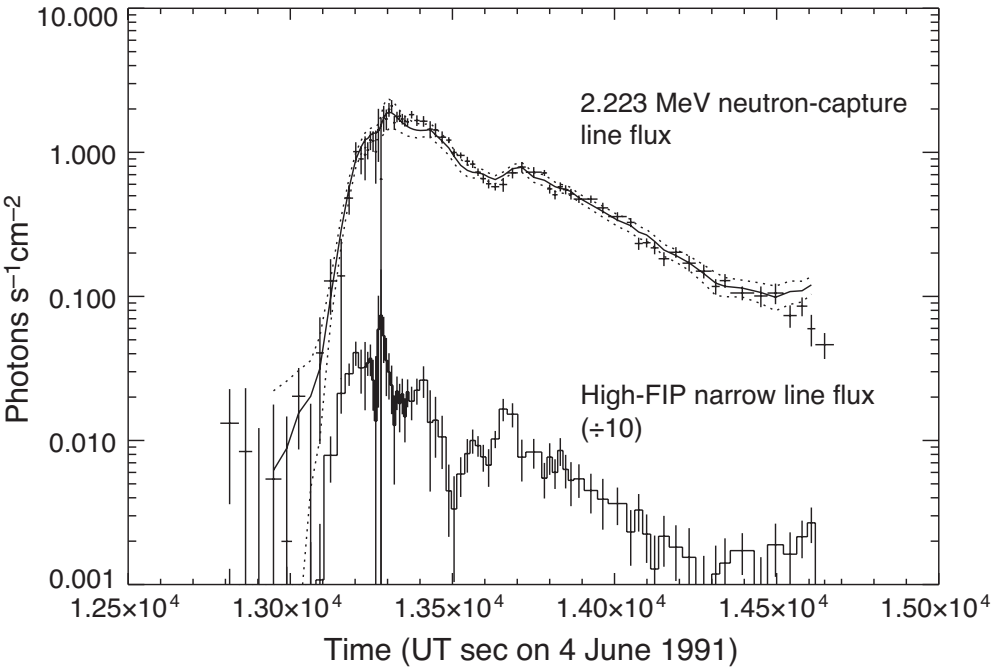

Fig. 30.— Comparison of the 2.223 MeV neutron capture line time history measured with OSSE from the June 4 flare with a time history calculated with the parameters indicated in the text. Also shown is the time history of the high-FIP narrow deexcitation line flux assumed to represent the accelerated ion release time history. The dotted curves represent the ± 1-σ uncertainties for the calculated curve.

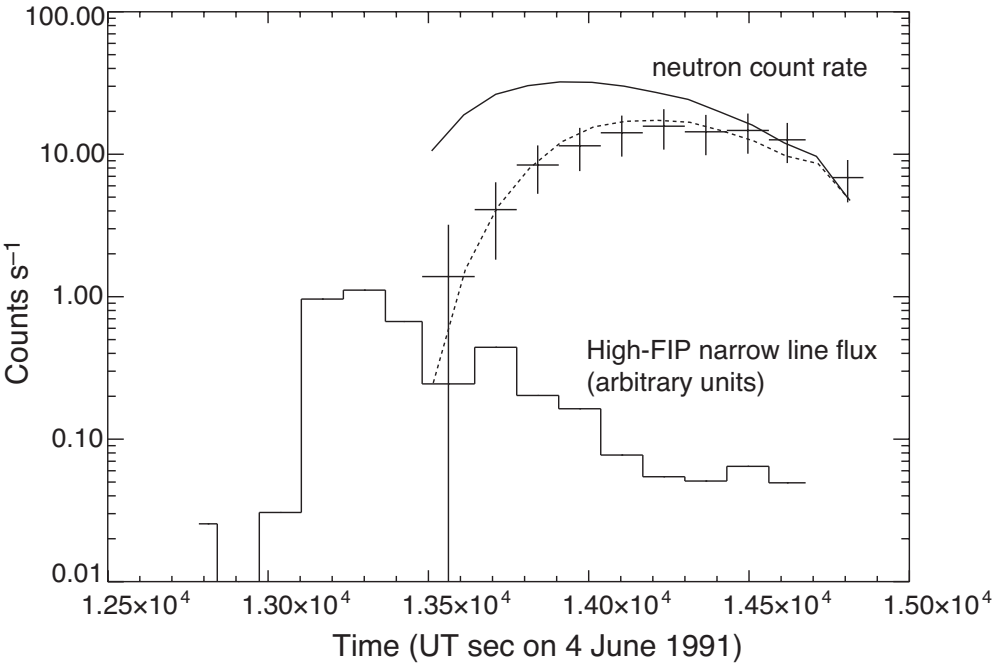

Fig. 31.— Comparison of the >23 MeV neutron count rate time history measured with OSSE from the June 4 flare with count rate time histories calculated with the parameters indicated in the text. The solid curve is for an unbroken power-law accelerated-particle spectrum and the dotted curve is for a spectrum cut off at $E_c = 125$ MeV nucleon^{-1}. Also shown is the time history of the high-FIP narrow deexcitation line flux (histogram) assumed to represent the accelerated ion release time history.

Table 1. Parameters

Type	Parameter
acceleration	power law index, s
	acceleration release time history, $a_{\rm ion}(t)$
	accelerated-particle composition
physical	level of PAS, λ
	magnetic convergence, δ
	loop half-length, L_c
	ambient composition
	atmospheric density & temperature model, $n(h)$ & $T(h)$
	flare heliocentric angle, $\theta_{\rm obs}$

Table 2. Ambient and Accelerated-Ion Compositions

Element	Ambient	Accelerated
H	1.0	1.0
^{3}He	3.0×10^{-5}	0.5
^{4}He	0.1	0.5
C	2.96×10^{-4}	4.65×10^{-3}
N	7.90×10^{-5}	1.24×10^{-3}
O	6.37×10^{-4}	1.00×10^{-2}
Ne	1.59×10^{-4}	4.55×10^{-3}
Mg	1.25×10^{-4}	5.89×10^{-3}
Al	1.00×10^{-5}	1.57×10^{-4}
Si	9.68×10^{-5}	4.55×10^{-3}
S	2.03×10^{-5}	9.56×10^{-4}
Ca	6.75×10^{-6}	1.06×10^{-4}
Fe	8.54×10^{-5}	1.34×10^{-2}

Table 3. Approximate Threshold Energies of Neutron Production Reactions

Reaction	Threshold Energy (MeV nucleon^{-1})
p – CNO...	5–10
α – CNO...	$\sim$1
p – H	$\sim$300
p – He	$\sim$30
α – He	$\sim$10

Table 4. Measurable quantities and their Dependences on the Acceleration and Physical Parameters

Observable	Acceleration Parameter	Physical Parameter
narrow deexcitation line fluences & ratios	α/p, s	ambient abundances
narrow deexcitation line shift and shape	α/p, s	δ, λ, $\theta_{\rm obs}$, $n(h)$
narrow deexcitation line time history	$a_{\rm ion}(t)$	δ, λ, L, $n(h)$
electron bremsstrahlung time history	$a_{\rm e}(t)$	L
neutron-capture line fluence	α/p, s	δ, λ, $\theta_{\rm obs}$, $n(h)$, ambient ^{3}He/H
neutron-capture line time history	$a_{\rm ion}(t)$, α/p, s	δ, λ, $\theta_{\rm obs}$, L, $n(h)$, ambient ^{3}He/H
neutron fluence at Earth	α/p, s	δ, λ, $\theta_{\rm obs}$, $n(h)$
neutron arrival time history at Earth	$a_{\rm ion}(t)$, α/p, s	δ, λ, $\theta_{\rm obs}$, L, $n(h)$
images	—	L, $\theta_{\rm obs}$